Nonlinear Instability Behavior of a High Speed Multistage Compressor

by

Hong Shu

S.B. in Thermal Engineering, Tsinghua University, Beijing, June 1989

Submitted to the Department of Aeronautics and Astronautics
in partial fulfillment of the requirements for the degree of

Master of Science in Aeronautics and Astronautics

at the

MASSACHUSETTS INSTITUTE OF TECHNOLOGY

February 1996

© Massachusetts Institute of Technology 1996. All rights reserved.

Author ....
Department of Aeronautics and Astronautics
November 24, 1995

Certified by ....
Professor Edward M. Greitzer
H. N. Slater Professor of Aeronautics and Astronautics
Thesis Supervisor

Accepted by ....
Professor Harold Y. Wachman
Chairman, Department Graduate Committee

Nonlinear Instability Behavior of a High Speed Multistage Compressor

By

Hong Shu

Abstract

This Thesis describes the development and application of a nonlinear analysis for examining the instability inception process in multi-stage high speed compressors. The goal is to develop a numerical procedure which can capture the unsteady behavior of these type of turbomachines and to use the model to assess the influence of non-linearities on stall onset. The model is built on two-dimensional unsteady compressible description of the flow in the blade free regions with a distributed bodyforce field to represent the flow inside the blade row. The numerical scheme is Jameson's finite volume method and time-matching technique. The thesis shows comparison of the computational program against several different cases including a four-stage high speed compressor run at Wright Laboratory. The calculations show that as observed in practice, the system can be driven unstable at a normally linearly stable condition by external forcing. An investigation has also been conducted on the effect of different forcing structures on stall inception.

Thesis Supervisor: Professor E.M.Greitzer

Title: H.N. Slater Professor of Aeronautics and Astronautics

1

Acknowledgements

First, I'd like to thank Prof. Greitzer for his continuous encouragement and criticism. I am grateful for his valuable time and guidance in this study. I also want to thank Dr. Tan, for his very friendly and useful discussions and suggestions all along this research; Dr. Hendricks, for his very important initial guidance and continuous help. It is him who introduced me into the stability field; Prof. Paduano, for his friendly remarks and continuous interest.

Special thanks go to Yifang Gong, for the numerous small but important discussions. I would also like to take this opportunity to thank all my friends at GTL. Catherine, for her very precious friendship; Jan, for his incredible caring and unique cheerful character; Martin, for his strong support and very impressive personality which I enjoy very much. My office mates: Chris, Ken and Ish, they made my staying at GTL a lot easier. I am also grateful for Don, Luc and Harold.

Last, but not least, I want to express my gratitude to my husband, Yongcheng Liang, for his very strong moral and actual support.

Table of Contents

List of Figures

Nomenclature

a: speed of sound

A: area

b_x: non-dimensional axial chord

c: local speed of sound

dm_j: mass flow rate change across the cell (j,k)

dmb: mass flow rate change across a blade

E: total internal energy

F: four component vector in Euler equations

F_x: axial bodyforce

F_y: circumferential bodyforce

G: four component vector in Euler equations

H: total enthalpy

M: Mach number

$\dot{m}$: mass flow rate

n: harmonic number

P: static pressure

r: compressor mean radius

R: streamtube thickness

S: source terms of Euler equations

S_x: switch in x direction in numerical smoothing

S_y: switch in y direction in numerical smoothing

t: time

T: temperature

u: axial velocity

U_r: rotor rotating speed

v: circumferential velocity

V: volume

x: axial coordinate

y: circumferential coordinate

ρ: density

γ: specific heat ratio

γ_2: non-dimensional constant in numerical smoothing

γ_4: non-dimensional constant in numerical smoothing

Δt: time step

ϕ: flow coefficient. $\phi = u / U_r$

ψ: total-to-static pressure rise

β: flow angle

η: adiabatic efficiency

τ: time lag constant

λ: rotor inertia parameter

μ: compressor inertia parameter

α: growth rate

ω: rotating frequency

Subscripts:

1: leading edge of the blade

2: trailing edge of the blade

j: number of grid in axial direction

k: number of grid in circumferential direction

E: east side of a computational cell

N: north side of a computational cell

W: west side of a computational cell

S: south side of a computational cell

t: stagnation quantity

*: critical quantity

mx: total number of grids in axial direction

P: quantity in the plenum

c: quantity in the compressor

T: quantity in the throttle

a: quantity in ambient

': relative quantity

s: quantity in the stator

r: quantity in the rotor

is: isentropic

ss: steady state

Superscripts:

(0): previous time step

(1): stage 1 of four-stage Runge-Kutta method

(2): stage 2 of four-stage Runge-Kutta method

(3): stage 3 of four-stage Runge-Kutta method

(4): stage 4 of four-stage Runge-Kutta method

n: time step n

Chapter 1. Introduction

1.1 Background

Rotating stall and surge are widely recognized as the instabilities which limit the operating range of compression systems. Surge is a low frequency, essentially axisymmetric oscillation which involves the whole compression system. Rotating stall is a wave propagating in the circumferential direction at a fraction of rotor frequency, which is localized to the compressor blade row region.

Because rotating stall and surge can have significant effect on gas turbine engine operability, there has been a large amount of research on the basic fluid dynamics of these phenomena as well as on ways to avoid or control them. Many of the previous work have concentrated on low-speed (blade Mach number less than 0.3) compression systems[1,2,3,4]. However, modern compressors have blade Mach numbers around 1.0, and a natural question is whether there are differences concerning these instabilities between low-speed and high-speed compressors.

There has been some recent work on rotating stall and surge in high speed compressors[5,6,7,8,9]. Prior to the work of Tryfonidis et. al[12], the conclusion was that there were no basic differences between the unsteady behavior at low and high speed compressors. Tryfonidis et al pointed out that compressibility which had an axial structure introduced another class of modes. The experimental data presented showed that it is one of the compressible modes which becomes unstable first. Further, the rotating speed is near shaft speed in a

high-speed compressor running at 100% corrected speed. In low speed compressors, the wave which first goes unstable is an mode which rotates at 0.5 shaft frequency or less and which we will refer to as the "incompressible mode". This low speed behavior is captured by the incompressible Moore-Greitzer model [2], while the high speed behavior is shown in the stability analysis of Hendricks et al.

A typical experimental result is given in figure 1.1, which shows a Spectral Density (PSD) plot of the experimental data of a high speed 4-stage compressor (the EFC compressor tested at the Air Force Compressor Research Facility) at 100% corrected speed. A wave traveling at shaft frequency grows in amplitude as the throttle is closed. This shaft frequency wave, which can be driven by the non-uniform rotor geometry, does not show the same growth in low speed compressors. We associate this wave with the natural mode predicted as the least damped by the compressible linearized stability model. The compressible mode with a frequency near shaft frequency is excited by the external forcing. The measured reflect both this forcing and the resultant dynamic response of the compressor.

The two-dimensional compressible linearized stability model mentioned above ([13],1991) was first developed by Bonnaure and updated by Hendricks ([10],1993), and applied to active control by Feulner ([18],1994). This approach treats the compressor as a series of actuator ducts (1 per blade row) separated by inter-blade row volumes, with suitable matching conditions at the leading and trailing edges of each blade row. The results of the calculation include the determination of the neutral stability operating point, and the circumferential and axial shape of the perturbations, the wave rotational frequency and growth rate. It is the compressible mode which dominates at high corrected speed.

Applications of this model to high speed compression systems reveal that there are infinite number of modes for each spatial harmonic, in contrast to the incompressible case where there is only one mode for each spatial harmonic. The lowest frequency mode has a circumferential wavelength equal to the compressor perimeter and the local mass flow is nearly uniform along the axial axis, similar to the mode in the incompressible machine. We refer to this as the "incompressible mode". In terms of circumferential and axial wave number we designate it [1,0] for n=1, [2,0] for n=2, etc. The next lowest mode is therefore [1,1] for n=1 with an axial wavelength scaling on the compressor length.

The linearized approach only applies to small perturbations. The stall inception process, during which the waves grow to large amplitude, is not described by this model and the assumption that each spatial harmonic and each mode evolve independently is no longer true as the wave amplitude grows. In addition, determining the influence of external forcing is beyond the scope of the linear theory. For example, experimental data on high speed compression systems show that instability occurs at a mass flow where the damping ratio positive. It is hypothesized that the cause of this is that finite disturbances are encountered which are large enough to induce a nonlinear response of the system.

Mansoux et al(1993) developed an incompressible nonlinear stability analysis of rotating stall using a Liapunov function approach[16]. This showed that a linearly stable equilibrium point with a small domain of attraction can be destabilized by a large enough perturbation. Specifically, in a compression system when the so-called domain of attraction of an operating point becomes very small, disturbances which might be considered "linear" in magnitude can

actually be unstable due to nonlinear effects. Mansoux's analysis however does not describe high speed machines.

1.2 Objectives.

The objective of this thesis is to develop a computational nonlinear stability analysis of the compressible flow in multi-stage high speed compressors. The model should be able to capture the main features of the transient behavior of rotating stall and surge, and the effect of external forcing on compressor instability.

1.3 Approach.

The compression system includes an upstream duct, a multi-stage compressor, a downstream duct, a plenum and a throttle. The basic unit in the compressor is the blade row, which is separated from other blade rows by an inter-row gap.

The flow in the upstream and downstream ducts as well as gaps are modeled using a two-dimensional unsteady compressible description. The flow inside the blade passage is represented by an unsteady compressible flow with a distributed bodyforce field which is determined by the blade row characteristics (pressure rise and exit flow angle). In the plenum and throttle, the flow is modeled using a one-dimensional unsteady compressible description [1].

The numerical scheme to solve the fluid dynamic model is Jameson's finite-volume method and time-matching technique.

The stability of axisymmetric disturbances can be investigated by decreasing the throttle area. Flow transients resulting from a small change of the throttle area are damped until a critical operating point is reached, at which a growing transient occurs, finally developing into a limit cycle called "surge". Stability of the rotating wave can be simulated by imposing a circumferential disturbance on an axisymmetric steady-state flow field and tracking the system response to this disturbance. The disturbance will grow or decay depending on the operating point. The growth rate and rotating frequency of this circumferential disturbance can be obtained from its time history.

1.4 Thesis overview

Chapter 2 of this thesis addresses the numerical model including the aerodynamic description of each part of the compression system and the formulation of source terms which appear on the right-hand side of unsteady Euler equations and which represent the flow inside blade rows.

Chapter 3 describes the test cases used to assess the model. Comparison has been carried out with a two-dimensional non-linear incompressible computation done by Gong[24] by simulating a hypothetical single-stage compressor with blade Mach number of 0.2. Calculations are performed for a NASA three-stage compressor and a four-stage compressor at Wright Laboratory. Comparisons of mean flow calculations with results from another CFD calculation done at Pratt & Whitney are also made. The stability calculations are also compared with a linearized compressible analysis, as well as experimental data.

In chapter 4, an investigation of the effect of forcing on stall inception will be performed. Specifically, we wish to see how the stall inception point changes with different level of (a) forcing by an extend disturbance rotating at shaft speed and (b) forcing due to a stationary disturbance.

Chapter 2. Description of the Fluid Dynamic Model

2.1 Geometry of the compression system

The compression system considered here consists of five parts: an upstream duct, a multi-stage compressor, a downstream duct, a plenum and a throttle valve. The layout of the system is shown in figure 2.1, which is a cross-section along the circumferential direction.

upstream   compressor downstream plenum
duct   duct
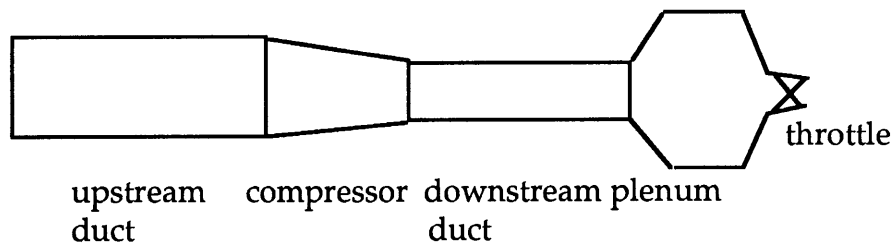
Figure 2.1 Compression system configuration

The upstream and downstream ducts are straight cylindrical channels with constant area. The basic units inside the compressor are a blade row which can be inlet guide vanes, a rotor, or a stator, and a inter-row gap which separates blade rows.

2.2 Assumptions

The compressor is taken to have high hub-to-tip ratio so that radial variations of the flow quantities can be neglected. Area changes are taken into account. The flow is considered adiabatic. The bodyforces inside the compressor are determined by the compressor characteristics (which are known from experimental data or from results of a mean flow prediction model). These bodyforces are the way in which viscous effects are taken into account.

2.3 Modeling ducts and inter-row gaps

2.3.1 Equations

The fluid mechanics in the upstream and downstream ducts as well as in inter-row gaps are described as the motion of an unsteady inviscid compressible gas in two dimensions. Adding varying streamtube thickness in the third direction to account for area change, the quasi three-dimensional Euler equations in conservative form and in Cartesian coordinates are as follows:

$$\frac{\partial U}{\partial t} + \frac{\partial F}{\partial x} + \frac{\partial G}{\partial y} = S \tag{2.1}$$

where U, F and G are four component vectors given by:

$$U = \begin{pmatrix} \rho R \\ \rho u R \\ \rho v R \\ \rho E R \end{pmatrix} \quad F = \begin{pmatrix} \rho u R \\ (\rho u^2 + P)R \\ \rho u v R \\ \rho u H R \end{pmatrix} \quad G = \begin{pmatrix} \rho v R \\ \rho u v R \\ (\rho v^2 + P)R \\ \rho v H R \end{pmatrix} \quad S = \begin{pmatrix} 0 \\ P\dfrac{\partial R}{\partial x} \\ 0 \\ 0 \end{pmatrix}$$

In these equations R is the streamtube thickness. The pressure P, and total enthalpy H are related to the density ρ, velocity components u and v, and total energy per unit mass E by the following two equations which assume a perfect gas with a constant specific heat ratio γ:

$$P = (\gamma - 1)\rho[E - \frac{1}{2}(u^2 + v^2)] \tag{2.2}$$

$$H = E + \frac{P}{\rho} \tag{2.3}$$

Additional equations which will be required are the definitions of the speed of sound, Mach number, stagnation pressure and stagnation density.

$$c = \sqrt{\frac{\gamma P}{\rho}} \tag{2.4}$$

$$M = \frac{\sqrt{u^2 + v^2}}{c} \tag{2.5}$$

$$P_t = P(1 + \frac{\gamma - 1}{2}M^2)^{\frac{\gamma}{\gamma - 1}} \tag{2.6}$$

$$\rho_t = \rho(1 + \frac{\gamma - 1}{2}M^2)^{\frac{1}{\gamma - 1}} \tag{2.7}$$

The flow variables are non-dimensionalized using the upstream stagnation density, the stagnation speed of sound and the mean radius. This leaves the equations unchanged and gives the following inlet stagnation quantities:

$$H_t = \frac{1}{\gamma - 1}, \qquad \rho_t = 1, \qquad P_t = \frac{1}{\gamma}$$

2.3.2 Numerical scheme

To solve equation (2.1), the node-centered Jameson finite volume scheme is used.

1. Finite volume discretization:

Take the integral of equation (2.1):

$$\frac{d}{dt}\int_{\Omega} U d\Omega + \int_{\partial\Omega}(Fn_x + Gn_y)dl = \int_{\Omega} S d\Omega \qquad (2.8)$$

$$\vec{n} = (\frac{dy}{dl}, -\frac{dx}{dl})$$
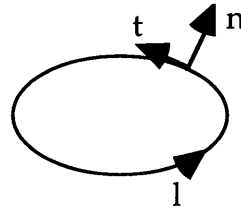
Figure 2.2

$$\frac{d}{dt}\int_{\Omega} U d\Omega + \oint(Fdy - Gdx) = \int_{\Omega} S d\Omega \qquad (2.9)$$

In figure 2.3, node (j,k) is surrounded by a cell ABCD with four sides marked E,S,W,N.
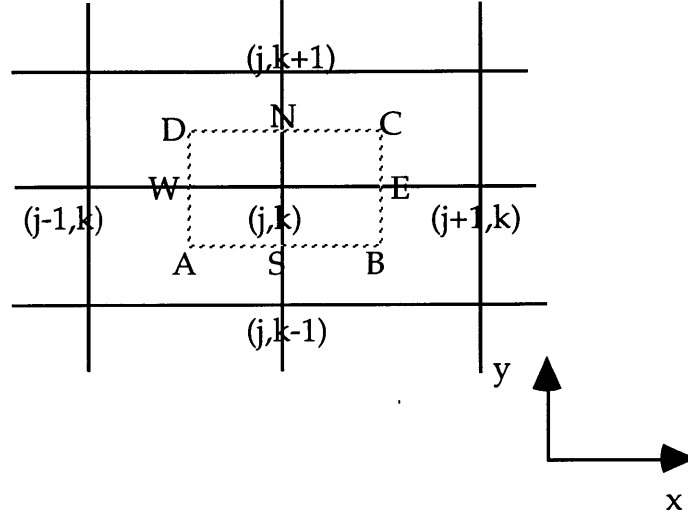
Figure 2.3 Grid and cell for cell-centered scheme

The grid of points A, B, C, D is:

A: (j-1/2, k-1/2)

B: (j+1/2, k-1/2)

C: (j+1/2, k+1/2)

D: (j-1/2, k+1/2)

Using equation (2.9) on cell (j,k):

$$\frac{d}{dt} \int_{\Omega_{j,k}} U d\Omega + (F\Delta y - G\Delta x)_E + (F\Delta y - G\Delta x)_N +$$

$$(F\Delta y - G\Delta x)_W + (F\Delta y - G\Delta x)_S = \int_{\Omega_{j,k}} S d\Omega \qquad (2.10)$$

Where:

$$U_{j,k} = \frac{\int_{\Omega_{j,k}} U d\Omega}{\int_{\Omega_{j,k}} d\Omega} \qquad \text{average value of U over cell (j,k)}$$

$$\int_{\Omega_{j,k}} d\Omega = A_{j,k} \qquad \text{area}$$

$$S_{j,k} = \frac{\displaystyle\int_{\Omega_{j,k}} S d\Omega}{\displaystyle\int_{\Omega_{j,k}} d\Omega} = \frac{\displaystyle\int_{\Omega_{j,k}} S d\Omega}{A_{j,k}}$$

Thus:

$$A_{j,k} \frac{dU_{j,k}}{dt} + [F_E(y_C - y_B) - G_E(x_C - x_B)] +$$
$$[F_N(y_D - y_C) - G_N(x_D - x_C)] + [F_W(y_A - y_D) - G_W(x_A - x_D)] + \quad (2.11)$$
$$[F_S(y_B - y_A) - G_S(x_B - x_A)] = A_{j,k} S_{j,k}$$

F_E can be approximated as:

$$F_E = F_{j+\frac{1}{2},k} = \frac{1}{2}(F_{j,k} + F_{j+1,k})$$

so is G_E, F_N, etc.

Writing (2.3) in short:

$$\frac{dU_{j,k}}{dt} = -\frac{1}{A_{j,k}} \sum \text{Fluxes} + S_{j,k} \equiv R_{j,k} \qquad (2.12)$$

2. Time discretization:

A four-stage Runge-Kutta method is used here:

$U^{(0)} = U^n \qquad$ known value at time step n

$U^{(1)} = U^{(0)} + \frac{1}{4}\Delta t R^{(0)}$

$U^{(2)} = U^{(0)} + \frac{1}{3}\Delta t R^{(1)}$

$U^{(3)} = U^{(0)} + \frac{1}{2}\Delta t R^{(2)}$

$U^{(4)} = U^{(0)} + \Delta t R^{(3)}$

$U^{n+1} = U^{(4)} \qquad$ new value at time step n+1

24

3. Numerical smoothing:

Most discrete approximations to the Euler equations require the addition of numerical smoothing (or artificial viscosity) to overcome two problems:

1). Dissipation of steady high wave number oscillations which have wavelengths comparable to grid spacing, and which are solutions of the finite difference equations, but not of the partial differential equations. These waves can amplify and lead to instability.

2). Capturing of shock waves is needed to suppress or limit overshoots.

The semi-discrete cell-based Euler equation with numerical smoothing is:

$$A_{j,k} \frac{dU_{j,k}}{dt} + (\sum \text{Fluxes} - A_{j,k}S_{j,k}) = D_{j,k} \tag{2.13}$$

where

$$D_{j,k} = \gamma_2 [\delta_x (S_x \frac{A}{\Delta t} \delta_x U) + \delta_y (S_y \frac{A}{\Delta t} \delta_y U)]_{j,k} -$$

$$\gamma_4 [\delta_x (\frac{A}{\Delta t} \delta_x^3 U) + \delta_y (\frac{A}{\Delta t} \delta_y^3 U)]_{j,k}$$

γ_2, γ_4 are non-dimensional constants; $\gamma_2 \approx 0.05 \sim 0.5$, $\gamma_4 \approx 0.01$,

S_x, S_y are switches to be defined later.

Combining $D_{j,k}$ with fluxes, (2.13) becomes:

$$A_{j,k} \frac{dU_{j,k}}{dt} + (\sum \text{mod ifiedfluxes} - A_{j,k}S_{j,k}) = 0 \tag{2.14}$$

For example:

$$(\text{mod ifiedfluxes})_E = F_E \Delta y_E - G_E \Delta x_E - \gamma_2 (\frac{S_x A}{\Delta t})_E (U_{j+1,k} - U_{j,k}) +$$

$$\gamma_4 (\frac{A}{\Delta t})_E (U_{j+2,k} - 3U_{j+1,k} + 3U_{j,k} - U_{j-1,k})$$

$$(\text{mod ifiedfluxes})_W = F_W \Delta y_W - G_W \Delta x_W + \gamma_2 (\frac{S_x A}{\Delta t})_W (U_{j,k} - U_{j-1,k}) -$$

$$\gamma_4 (\frac{A}{\Delta t})_W (U_{j+1,k} - 3U_{j,k} + 3U_{j-1,k} - U_{j-2,k})$$

25

There are several ways to calculate S_x and S_y. Here the following formula is used:

$$S_x \big|_{j,k} = \frac{\left| P_{j+1,k} - 2P_{j,k} + P_{j-1,k} \right|}{P_{j,k}}$$

$$S_y \big|_{j,k} = \frac{\left| P_{j,k+1} - 2P_{j,k} + P_{j,k-1} \right|}{P_{j,k}}$$

(2.15)

2.3.3 Time step

For the Cartesian mesh used in this calculation, the maximum time step among all cells for Jameson's method is:

$$\Delta t_{max} = \frac{\Delta x \Delta y}{|u|\Delta y + |v|\Delta x + c\sqrt{\Delta x^2 + \Delta y^2}}$$

(2.16)

In practice, Δt is limited to $0.9 \sim 0.95 \Delta t_{max}$.

2.3.4 Boundary conditions

1. Subsonic inlet boundary

The inlet stagnation pressure Pt, the stagnation temperature Tt and the flow angle θ are specified. As stated in 2.3.1, the flow variables are non-dimensionalized using the upstream stagnation density and stagnation speed of sound, so the inlet stagnation quantities are:

$$H_t = \frac{1}{\gamma - 1}, \qquad \rho_t = 1, \qquad P_t = \frac{1}{\gamma} \qquad T_t = \frac{1}{\gamma R}$$

The static pressure, temperature and density can be expressed as functions of axial velocity as follows (see NACA Report 1135)

$$P = P_t[1 - \frac{\gamma - 1}{\gamma + 1}(1 + \tan^2 \theta)\frac{u^2}{a_*^2}]^{\frac{\gamma}{\gamma-1}} = P(u)$$

(2.17)

26

$$T = T_t[1 - \frac{\gamma - 1}{\gamma + 1}(1 + \tan^2 \theta)\frac{u^2}{a_*^2}] = T(u) \qquad (2.18)$$

$$\rho = \rho_t[1 - \frac{\gamma - 1}{\gamma + 1}(1 + \tan^2 \theta)\frac{u^2}{a_*^2}]^{\frac{1}{\gamma - 1}} = \rho(u) \qquad (2.19)$$

To close the system of equations, we select the characteristic relations coupling the boundary with the interior flow volume.

$$\frac{\partial P}{\partial t} - \rho c \frac{\partial u}{\partial t} = -(u - c)(\frac{\partial P}{\partial x} - \rho c \frac{\partial u}{\partial x}) \qquad (2.20)$$

The implicit finite difference relation is:

$$\delta P - \rho c \delta u = -\frac{\lambda_4}{1 + \lambda_4}[P_1 - P_0 - \rho c(u_1 - u_0)] \equiv R \qquad (2.21)$$
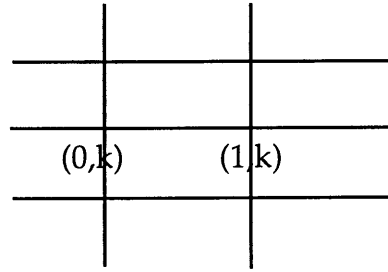
Figure 2.4 Grid at inlet boundary

where

$$\lambda_4 = (u - c)\frac{\Delta t}{\Delta x}$$

$$\delta P = \frac{\partial P}{\partial u}\delta u$$

Thus

$$\delta u = \frac{R}{\frac{\partial P}{\partial u} - \rho c}$$

where

$$\frac{\partial P}{\partial u} = P_t \frac{\gamma}{\gamma - 1}[1 - \frac{\gamma - 1}{\gamma + 1}(1 + \tan^2 \theta)\frac{u^2}{a_*^2}]^{\frac{\gamma}{\gamma - 1} - 1}[-\frac{\gamma - 1}{\gamma + 1}(1 + \tan^2 \theta)\frac{2u}{a_*^2}]$$

$$= -\frac{2u}{a_*^2}\frac{1 + \tan^2 \theta}{\gamma + 1}[1 - \frac{\gamma - 1}{\gamma + 1}(1 + \tan^2 \theta)\frac{u^2}{a_*^2}]^{\frac{1}{\gamma - 1}} \qquad (2.22)$$

27

Hence:

$$u_0^{n+1} = u_0^n + \delta u$$

$$v_0^{n+1} = u_0^{n+1} \tan \theta$$

$$P_0^{n+1} = P(u_0^{n+1})$$

$$T_0^{n+1} = T(u_0^{n+1})$$

$$\rho_0^{n+1} = P_0^{n+1} / (RT_0^{n+1})$$

Here $\quad \dfrac{a_*^2}{a_0^2} = \dfrac{2}{\gamma + 1}, \quad$ and $\quad a_0 = \sqrt{\gamma R T_t} = 1,$

so $\quad a_*^2 = \dfrac{2}{\gamma + 1}$

2. Subsonic exit boundary

The exit boundary considered here is the exit of the downstream duct. So P_{exit} equals the plenum pressure P_p, and $P_{mx+1} = P_{exit}$.

Assume P_{exit} is specified. The four characteristic relations connecting points (mx, k) and (mx+1, k) at the exit are:

$$\frac{\partial \rho}{\partial t} - \frac{1}{c^2} \frac{\partial P}{\partial t} = -u \left(\frac{\partial \rho}{\partial x} - \frac{1}{c^2} \frac{\partial P}{\partial x} \right) \tag{2.23}$$

$$\frac{\partial P}{\partial t} + \rho c \frac{\partial u}{\partial t} = -(u + c) \left(\frac{\partial P}{\partial x} + \rho c \frac{\partial u}{\partial x} \right) \tag{2.24}$$

$$\frac{\partial v}{\partial t} = -u \frac{\partial v}{\partial x} \tag{2.25}$$

$$\frac{\partial P}{\partial t} - \rho c \frac{\partial u}{\partial t} = -(u - c) \left(\frac{\partial P}{\partial x} - \rho c \frac{\partial u}{\partial x} \right) \tag{2.26}$$

Implicit finite difference approximations for the above relations are given as follows:

$$\delta \rho - \frac{1}{c^2} \delta P = -\frac{\lambda_1}{1 + \lambda_1} \left[\rho_{mx+1} - \rho_{mx} - \frac{1}{c^2} (P_{mx+1} - P_{mx}) \right] \equiv R_1 \tag{2.27}$$

$$\delta P + \rho c \delta u = -\frac{\lambda_2}{1 + \lambda_2} \left[P_{mx+1} - P_{mx} + \rho c (u_{mx+1} - u_{mx}) \right] \equiv R_2 \tag{2.28}$$

$$\delta v = -\frac{\lambda_1}{1 + \lambda_1} (v_{mx+1} - v_{mx}) \equiv R_3 \tag{2.29}$$

$$\delta P - \rho c \delta u = -\frac{\lambda_4}{1+\lambda_4}[P_{mx+1} - P_{mx} - \rho c(u_{mx+1} - u_{mx})] \equiv R_4 \quad (2.30)$$

The quantities $\lambda 1$, $\lambda 2$, and $\lambda 4$ are:

$$\lambda_1 = \frac{u\Delta t}{\Delta x}, \quad \lambda_2 = \frac{(u+c)\Delta t}{\Delta x}, \quad \lambda_4 = \frac{(u-c)\Delta t}{\Delta t}$$

Solving for δP:

$$\delta P = \begin{cases} \dfrac{R_2 + R_4}{2} & (M = \dfrac{u_{mx}}{c_{mx}} > 1) \\ 0 & (M < 1) \end{cases}$$

Thus:

$$\delta \rho = R_1 + \frac{1}{c^2}\delta P$$

$$\delta u = \frac{R_2 - \delta P}{\rho c}$$

$$\delta v = R_3$$

Therefore:

$$P_{mx+1}^{n+1} = P_{mx+1}^n + \delta P$$

$$\rho_{mx+1}^{n+1} = \rho_{mx+1}^n + \delta \rho$$

$$u_{mx+1}^{n+1} = u_{mx+1}^n + \delta u$$

$$v_{mx+1}^{n+1} = v_{mx+1}^n + \delta v$$

The exit boundary considered here is the exit of the downstream duct. So P_{exit} equals the plenum pressure P_p, and $P_{mx+1} = P_{exit}$.

2.4 Modelling the plenum and the throttle

The continuity equation for the plenum [2] is:

$$\dot{m}_C - \dot{m}_T = \frac{\rho V_P}{\gamma P}\frac{dP_P}{dt} \quad (2.31)$$

29
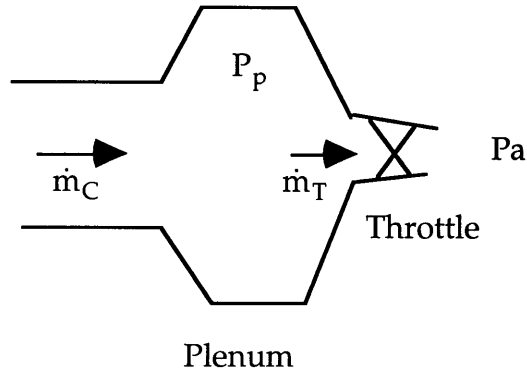
Figure 2.5 Plenum and throttle

In (2.31) $\dot{m}_C$ is the mass flow through the compressor.

$\dot{m}_T$ is the mass flow through the throttle.

V_P is the volume of the plenum.

ρ, P are the density and static pressure at the exit of the downstream duct.

Since the plenum serves as an upstream reservoir for the throttle, $\dot{m}_T$ can be expressed as:

$$\dot{m}_T = \sqrt{\gamma} A_T \sqrt{P_P \rho} \, \frac{M_T}{(1 + \frac{\gamma-1}{2} M_T^2)^{\frac{\gamma+1}{2(\gamma-1)}}} \qquad (2.32)$$

A_T , the area of the throttle which determines the compressor operating condition, is specified.

M_T is the Mach number of the throttle. M_T is related to the plenum pressure by:

$$\frac{P_P}{P_a} = (1 + \frac{\gamma-1}{2} M_T^2)^{\frac{\gamma}{\gamma-1}} \leq (1 + \frac{\gamma-1}{2})^{\frac{\gamma}{\gamma-1}} \approx 1.893 \qquad (2.33)$$

(M_T =1 is the choking condition)

30

Thus

$$M_T = \begin{cases} \sqrt{\dfrac{2}{\gamma-1}[(\dfrac{P_P}{P_a})^{\frac{\gamma-1}{\gamma}}-1]} & \dfrac{P_P}{P_a} \leq 1.893 \\ 1 & \dfrac{P_P}{P_a} > 1.893 \end{cases}$$

Now M_T can be expressed as a function of P_P.

Then,

$$\frac{dP_P}{dt} = \frac{\gamma P}{\rho V_P}(\dot{m}_C - \dot{m}_T) \equiv R_T \qquad (2.34)$$

Apply four-stage Runge-Kutta method for time discretization as follows:

$$P_P^{(0)} = P_P^n$$

$$P_P^{(1)} = P_P^{(0)} + \frac{1}{4}\Delta t R_T^{(0)}$$

$$P_P^{(2)} = P_P^{(0)} + \frac{1}{3}\Delta t R_T^{(1)}$$

$$P_P^{(3)} = P_P^{(0)} + \frac{1}{2}\Delta t R_T^{(2)}$$

$$P_P^{(4)} = P_P^{(0)} + \Delta t R_T^{(3)}$$

$$P_P^{n+1} = P_P^{(4)}$$

2.5 Modelling the flow in blade rows

The flow in a blade row is represented by a locally uniform flow with distributed bodyforces. Locally no gradients of the fluid properties in the tangential direction are taken into account, but a hypothetical bodyforce changes the tangential momentum of the fluid.

In some engines, air is taken out from some blade rows in the compressor for various reasons such as cooling the turbine blades, which is called "bleeds". Since this model will be used to simulate modern high speed compressors, it should be able to address flow through a compressor with mass flow changes.

31

Change of mass flow through a blade row is represented by a source term in the continuity equation.

2.5.1 The equations

Derivations of the one-dimensional unsteady compressible flow equations in the cascades with bleeds and area changes are given in Appendix 1. The equations are:

continuity:

$$\frac{\partial(\rho R)}{\partial t} + \frac{\partial(\rho u R)}{\partial x} = dm_j \qquad (2.35)$$

axial momentum:

$$\frac{\partial(\rho u R)}{\partial t} + \frac{\partial[(\rho u^2 + P)R]}{\partial x} = P\frac{\partial R}{\partial x} + F_x + dm_j u \qquad (2.36)$$

circumferential momentum:

$$\frac{\partial(\rho v R)}{\partial t} + \frac{\partial(\rho u v R)}{\partial x} = F_y + dm_j v \qquad (2.37)$$

energy:

$$\frac{\partial(\rho E R)}{\partial t} + \frac{\partial(\rho u H R)}{\partial x} = dm_j H \qquad (2.38)$$

The quantity dm_j is the mass source per unit length along the axial direction. F_x and F_y are axial and circumferential bodyforces.

The above equations also apply to the flow in the rotor relative frame (t', x', y'), but the flow variables are all relative quantities (with prime). The equations are:

$$\frac{\partial(\rho' R)}{\partial t'} + \frac{\partial(\rho' u' R)}{\partial x'} = dm_j \qquad (2.39)$$

$$\frac{\partial(\rho' u' R)}{\partial t'} + \frac{\partial[(\rho' u'^2 + P')R]}{\partial x'} = P'\frac{\partial R}{\partial x} + F_x' + dm_j u' \qquad (2.40)$$

$$\frac{\partial(\rho' v' R)}{\partial t'} + \frac{\partial(\rho' u' v' R)}{\partial x'} = F_y' + dm_j v' \qquad (2.41)$$

$$\frac{\partial(\rho'E'R)}{\partial t'} + \frac{\partial(\rho'u'H'R)}{\partial x'} = dm_jH' \tag{2.42}$$

We need to transform these equations into the absolute frame with the relative flow variables, then replace the relative quantities with absolute quantities in order to obtain the flow equations in the rotor blade row. The relations between the relative coordinate (t', x', y') and the absolute coordinate (t, x, y) are:

$$\begin{cases} t = t' \\ x = x' \\ y = y' + \omega t' \end{cases} \tag{2.43}$$

where ω is the rotor rotating freqency, and $\omega = U_r/r$. U_r is the rotor speed and r is the compressor mean radius at mid-span. Here r=1 because it is non-dimensionalized by itself.

The relations of derivatives in the relative and absolute coordinates are:

$$\begin{cases} \dfrac{\partial}{\partial x'} = \dfrac{\partial}{\partial x} \\ \dfrac{\partial}{\partial t'} = \dfrac{\partial}{\partial t}\dfrac{\partial t}{\partial t'} + \dfrac{\partial}{\partial y}\dfrac{\partial y}{\partial t'} = \dfrac{\partial}{\partial t} + U_r\dfrac{\partial}{\partial y} \end{cases} \tag{2.44}$$

The equations in the rotor relative frame can be transformed into the absolute frame as shown below:

$$\frac{\partial(\rho'R)}{\partial t} + \frac{\partial(\rho'u'R)}{\partial x} + U_r\frac{\partial(\rho'R)}{\partial y} = dm_j \tag{2.45}$$

$$\frac{\partial(\rho'u'R)}{\partial t} + \frac{\partial[(\rho'u'^2 + P')R]}{\partial x} + U_r\frac{\partial(\rho'u'R)}{\partial y} = P'\frac{\partial R}{\partial x} + F_x' + dm_ju' \tag{2.46}$$

$$\frac{\partial(\rho'v'R)}{\partial t} + \frac{\partial(\rho'u'v'R)}{\partial x} + U_r\frac{\partial(\rho'v'R)}{\partial y} = F_y' + dm_jv' \tag{2.47}$$

$$\frac{\partial(\rho'E'R)}{\partial t} + \frac{\partial(\rho'u'H'R)}{\partial x} + U_r\frac{\partial(\rho'E'R)}{\partial y} = dm_jH' \tag{2.48}$$

The relations between relative and absolute quantities are as follows:

$$\begin{cases} \rho' = \rho \\ P' = P \\ u' = u \\ v' = v - U_r \end{cases} \qquad (2.49)$$

The continuity equation (2.45) and the axial momentum equation (2.46) will remain the same with absolute quantities.

Using the above relations in the circumferential momentum equation (2.47), we obtain:

$$\frac{\partial(\rho v R)}{\partial t} + \frac{\partial(\rho u v R)}{\partial x} + U_r \frac{\partial(\rho v R)}{\partial y} - U_r [\frac{\partial(\rho R)}{\partial t} + \frac{\partial(\rho u R)}{\partial x} + U_r \frac{\partial(\rho R)}{\partial y}]$$

$$= F_y + dm_j (v - U_r) \qquad (2.50)$$

Using:

$$\frac{\partial(\rho R)}{\partial t} + \frac{\partial(\rho u R)}{\partial x} + U_r \frac{\partial(\rho R)}{\partial y} = dm_j \qquad (2.51)$$

(2.50) becomes:

$$\frac{\partial(\rho v R)}{\partial t} + \frac{\partial(\rho u v R)}{\partial x} + U_r \frac{\partial(\rho v R)}{\partial y} = F_y + dm_j v \qquad (2.52)$$

In equation (2.48),

$$\begin{cases} E' = \frac{1}{\gamma - 1} \frac{P'}{\rho'} + \frac{1}{2}(u'^2 + v'^2) = E - v U_r + \frac{1}{2} U_r^2 \\ H' = H - v U_r + \frac{1}{2} U_r^2 \end{cases} \qquad (2.53)$$

Equation (2.48) becomes:

$$\frac{\partial(\rho E R)}{\partial t} + \frac{\partial(\rho u H R)}{\partial x} + U_r \frac{\partial(\rho E R)}{\partial y} -$$

$$U_r [\frac{\partial(\rho v R)}{\partial t} + \frac{\partial(\rho u v R)}{\partial x} + U_r \frac{\partial(\rho v R)}{\partial y}] +$$

$$\frac{1}{2} U_r^2 [\frac{\partial(\rho R)}{\partial t} + \frac{\partial(\rho u R)}{\partial x} + U_r \frac{\partial(\rho R)}{\partial y}]$$

$$= dm_j H - U_r dm_j v + \frac{1}{2} U_r^2 dm_j$$

$$(2.54)$$

Substitute equations (2.51) and (2.52) into (2.54) to get:

$$\frac{\partial(\rho ER)}{\partial t} + \frac{\partial(\rho uHR)}{\partial x} + U_r \frac{\partial(\rho ER)}{\partial y} = U_r F_y + dm_j H \qquad (2.55)$$

The equations in the stator and rotor blade rows can be written in the same form as equation (2.1):

$$\frac{\partial U}{\partial t} + \frac{\partial F}{\partial x} + \frac{\partial G}{\partial y} = S \qquad (2.56)$$

In a stator:

$$U = \begin{pmatrix} \rho R \\ \rho u R \\ \rho v R \\ \rho ER \end{pmatrix} \quad F = \begin{pmatrix} \rho u R \\ (\rho u^2 + P)R \\ \rho uvR \\ \rho uHR \end{pmatrix} \quad G = 0 \quad S = \begin{pmatrix} dm_j \\ F_{xs} + P\dfrac{\partial R}{\partial x} + dm_j u \\ F_{ys} + dm_j v \\ dm_j H \end{pmatrix}$$

In a rotor:

$$U = \begin{pmatrix} \rho R \\ \rho u R \\ \rho v R \\ \rho ER \end{pmatrix} \quad F = \begin{pmatrix} \rho u R \\ (\rho u^2 + P)R \\ \rho uvR \\ \rho uHR \end{pmatrix} \quad G = \begin{pmatrix} \rho U_r R \\ \rho u U_r R \\ \rho v U_r R \\ \rho EU_r R \end{pmatrix} \quad S = \begin{pmatrix} dm_j \\ F_{xr} + P\dfrac{\partial R}{\partial x} + dm_j u \\ F_{yr} + dm_j v \\ U_r F_{yr} + dm_j H \end{pmatrix}$$

The numerical scheme applied to equation (2.1) as described in sections (2.3.2) and (2.3.3) is used here.

2.5.2 Modelling the source terms

The so-called source terms are the terms on the right hand side of equation (2.56). Since (2.56) is solved for the four basic flow variables u, v, P, ρ, the bodyforces F_x, F_y in the source terms should be represented by these basic

35

variables and some specified quantities. We must also determine dm_j given mass source in each blade row.

We need to decide what quantities should be specified to determine F_x and F_y in a rotor and a stator. Two quantities are needed since there are two unknowns in either a rotor or a stator. A total-to-total pressure rise characteristic is chosen as one specified quantity for both a rotor and a stator. Then, the flow angle is chosen as another specified quantity in a stator; and in a rotor, the adiabatic efficiency is used to determine how much percent of shaft work are used to increase the total pressure across the rotor.

A stator and a rotor are thus treated differently.

1). In a stator, there are three unknowns:

$$dm_j, \ F_{xs}, \ F_{ys}$$

We specify:

dmb: mass flow source of the blade row, a function of the local flow coefficient ϕ, $dmb = f_1(\phi)$

ΔP_t: total pressure rise across the blade row. Also a function of the local flow coefficient ϕ, $\Delta P_t = f_2(\phi)$.

β: flow angle, fixed value.

According to the definition of dm_j in section 2.5.1, which is the mass flow change per unit axial length:

$$\int_{x_1}^{x_2} dm_j dx = dmb \tag{2.57}$$

The quantity dm_j is the axial distribution of dmb. Since $dm_j=0$ in the inter-row gaps, we use a sinusoidal function with value and derivatives of 0 at both the leading and the trailing edges to have a smooth distribution of this source term in the compressor.

$$dm_j = a_{dm} \left\{ \sin[\frac{2\pi}{x_2 - x_1}(x - x_1) - \frac{\pi}{2}] + 1 \right\} \tag{2.58}$$

Substituting dm_j into equation (2.57), and solving for a_{dm}:

$$a_{dm} = \frac{dmb}{x_2 - x_1} \tag{2.59}$$

The circumferential bodyforce changes the tangential momentum of the fluid. It can be formulated in the following way:

$$F_{ys} = \frac{\varepsilon \dot{m}(u_j \tan \beta_{jw} - u_j \tan \beta_j)}{(x_{j+1} - x_j)} \tag{2.60}$$

where β_{jw} is the specified fixed flow angle of cell (j,k).

β_j is the current flow angle of cell (j,k), $\beta_j = atan(v_j / u_j)$.

ε is a coefficient used to adjust the amount of bodyforce so to get the desired flow angle.
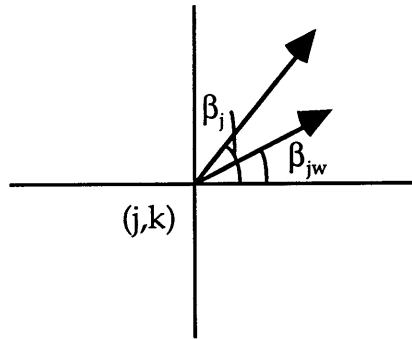
Figure 2.6 Flow angles on a cell

When $\beta_j > \beta_{jw}$ as shown in figure 2.5, F_{ys} is negative, which means that a downward bodyforce needs to be put on the fluid to make flow angle close to the given value.

To calculate the axial bodyforce F_x, we are given $\Delta P_{ts} = f(\phi_j)$ defined by

$$\frac{P_{t2}}{P_{t1}} = 1 + \frac{\Delta P_{ts}}{P_{t1}} \tag{2.61}$$

Given this total pressure rise, if it were an isentropic process, we would have:

$$\left.\frac{T_{t2}}{T_{t1}}\right|_{is} = \left(\frac{P_{t2}}{P_{t1}}\right)^{\frac{\gamma-1}{\gamma}} \tag{2.62}$$

$$\left.\Delta T_{ts}\right|_{is} = (T_{t2} - T_{t1})_{is} = T_{t1}\left(\left.\frac{T_{t2}}{T_{t1}}\right|_{is} - 1\right) \tag{2.63}$$

We need to distribute this isentropic total temperature change into each cell. Using the same function as (2.58), we have the isentropic total temperature change of a cell (j,k) as follows:

$$\left.dT_{tj}\right|_{is} = a_{Tt}\left\{\sin[\frac{2\pi}{x_2 - x_1}(x_j - x_1) - \frac{\pi}{2}] + 1\right\} \tag{2.64}$$

Where

$$a_{Tt} = \frac{\left.\Delta T_{ts}\right|_{is}}{x_2 - x_1}$$

The isentropic enthalpy change of a cell (j,k) is given by:

$$\left.\Delta H_{tj}\right|_{is} = \dot{m} C_p \left. dT_{tj}\right|_{is} \tag{2.65}$$

Because the flow is assumed adiabatic, the work done during the isentropic process is: $\left.\dot{W}_j\right|_{is} = \left.\Delta H_{tj}\right|_{is}$. For blade passages with high solidity, we can assume :

$$\left.\dot{W}_j\right|_{is} = F_{xs}u_j + F_{ys}v_j \tag{2.66}$$

Thus

$$F_{xs}u_j + F_{ys}v_j = \left.\Delta H_{tj}\right|_{is} \tag{2.67}$$

$$F_{xs} = \frac{\left.\Delta H_{tj}\right|_{is} - F_{ys}v_j}{u_j} \tag{2.68}$$

We should keep in mind that the real process is not isentropic, because there are dissipation terms on the right-hand side of energy equation aside from the work done by bodyforces. The work done in the stator is zero, as reflected in the energy equation (see Appendix 1).

38

2). In a rotor, there are three unknowns:

$$dm_j, \quad F_{xr}, \quad F_{yr}$$

We specify:

dmb: same definition as in the stator.

ΔP_t: same definition as in the stator.

η: adiabatic efficiency, $\eta = \dfrac{\left(\dfrac{P_{t2}}{P_{t1}}\right)^{\frac{\gamma-1}{\gamma}} - 1}{\dfrac{T_{t2}}{T_{t1}} - 1}$.

The calculation of dm_j is the same as in 1).

Given $\Delta P_{tr} = f(\phi_j)$, and going through the same procedure as in 1), we

obtain:

$$\Delta T_{tr}\big|_{is} = T_{t1}\left(\frac{T_{t2}}{T_{t1}}\bigg|_{is} - 1\right) \tag{2.69}$$

In the real process:

$$\Delta T_{tr} = \frac{\Delta T_{tr}\big|_{is}}{\eta} \tag{2.70}$$

We distribute ΔT_{tr} into each cell using the same function as in 1) to obtain:

$$dT_{tj} = a_{Tt}\left\{\sin[\frac{2\pi}{x_2 - x_1}(x_j - x_1) - \frac{\pi}{2}] + 1\right\} \tag{2.71}$$

where

$$a_{Tt} = \frac{\Delta T_{tr}}{x_2 - x_1}$$

We also have

$$\Delta H_{tj} = \dot{m}C_p dT_{tj} \tag{2.72}$$

The work done by the rotor is $\dot{W}_j = \Delta H_{tj}$, where $\dot{W}_j$ is the shaft work, i.e. $U_r F_{yr}$

in the source term of the energy equation of the rotor. Thus

$$U_r F_{yr} = \Delta H_{tj} \tag{2.73}$$

$$F_{yr} = \frac{\Delta H_{tj}}{U_r} \qquad (2.74)$$

Once we know F_{yr}, we can get F_{xr} the same way as in 1), i.e.:

$$F_{xr}u_j + F_{yr}v_j = \Delta H_{tj}\big|_{is} = \eta \Delta H_{tj} \qquad (2.75)$$

$$F_{xr} = \frac{\eta \Delta H_{tj} - F_{yr}v_j}{u_j} \qquad (2.76)$$

2.6 Unsteady blade row behavior

So far, the bodyforces determined by the blade row performance are assumed quasi-steady. To account for the unsteady effect of the fluid in the blade passage on the performance of the blade row, a first order lag is introduced [13] as a correction to the performance of a compressor. This model takes the form:

$$\tau \frac{dX}{dt} = X_{steady-state} - X \qquad (2.77)$$

Where: $X_{steady-state}$ is the steady state value of flow field variable.

X is the instantaneous value of a flow field variable.

τ is a time constant related to the convection time of the bulk flow through the blade channels, $\tau = \dfrac{\overline{b}_x}{\phi}$. Here $\overline{b}_x$ is the non-dimensional axial chord.

The unsteadiness of the total pressure loss L is used in the model.

For a stator:

$$\frac{dL_s}{dt} = \frac{L_{s,ss} - L_s}{\tau_s} \qquad (2.78)$$

For a rotor:

$$\frac{dL_r}{dt} + U_r \frac{dL_r}{dy} = \frac{L_{r,ss} - L_r}{\tau_r} \qquad (2.79)$$

Thus

$$\frac{dL_r}{dt} = -U_r \frac{dL_r}{dy} + \frac{L_{r,ss} - L_r}{\tau_r} \qquad (2.80)$$

L_s and L_r are then calculated by using four-stage Runge-Kutta method.

To find the unsteady total pressure rise ΔP_t, we need to know the ideal total pressure rise $\Delta P_t|_{ideal}$, because $\Delta P_t = \Delta P_t|_{ideal} - L$. $\Delta P_t|_{ideal} = 0$ in stators. In the rotors, an empirical formula is used, which is $\Delta P_t|_{ideal} = C + 0.5\phi \tan \beta_{exit}'$, obtained from the author's experience (see also [21]).

2.7 Flow chart of the computational program.

```
┌─────────────────────────────────────┐
│  geometry of the compression system │
└─────────────────────────────────────┘
                  │
                  ▼
        ┌─────────────────────┐
        │ generate cartesian grid │
        └─────────────────────┘
                  │
                  ▼
        ┌─────────────────────────┐
        │ read in specified quantities │
        │ and generate local compressor │
        │ characteristics │
        └─────────────────────────┘
                  │
                  ▼
        ┌─────────────────────────┐
        │ assume an initail flow field │
        └─────────────────────────┘
                  │
                  ▼
        ┌─────────────────────┐
        │ calculate time step │
        └─────────────────────┘
                  │
                  ▼
        ┌─────────────────────────┐
        │ calculate modified flux │
        └─────────────────────────┘
                  │
                  ▼
        ┌─────────────────────────┐
        │ calculate source terms │
        └─────────────────────────┘
                  │
                  ▼
        ┌─────────────────────────────┐
        │ calculate pressure in the plenum │
        └─────────────────────────────┘
                  │
                  ▼
        ┌─────────────────────────────┐
        │ calculate U from equation (2.12) │
        └─────────────────────────────┘
                  │
                  ▼
        ┌─────────────────────────────┐
        │ calculate u,v,P, ρ  in interior cells │
        │ from U │
        └─────────────────────────────┘
                  │
                  ▼
        ┌─────────────────────────────┐
        │ calculate up- & down-stream │
        │ boundary values using boundary │
        │ condition │
        └─────────────────────────────┘
                  │
                  ▼
        ┌─────────────────────────────┐
        │ calculate U, F, G in the whole flow │
        │ field │
        └─────────────────────────────┘
                  │  four-stage Runge-Kutta
                  ▼
        ┌─────────────────────────────┐
        │ store variables at this time step │
        └─────────────────────────────┘
                  │  go to next time step
                  ▼
        ┌─────────────────────────────┐
        │ stop when steady-state calculation │
        │ converges at one throttle setting │
        └─────────────────────────────┘
```

Chapter 3 Test cases to assess the model

3.1 Introduction

In this chapter comparisons are shown with the model of reference [4], with a two-dimensional non-linear incompressible model (developed by Gong), and with a linearized compressible model [13], and also some high-speed compressor data.

The model of [4] is a incompressible analytical stability analysis. This analysis and the non-linear incompressible model developed by Gong can be used to test the validity of the compressible model for low speed cases. Test case 1 is for this purpose. A single-stage low-speed compressor with hypothetical geometry and characteristics is simulated by the current model and a back-to-back comparison done with the non-linear incompressible computation. Both are then checked with the analytical result of model of [4].

The present model has also been assessed against data for multi-stage high speed compressors. The instability of a high speed multi-stage compressor at design or near-design speed is of most concern, so a four-stage compressor which has been run at the Wright laboratory operating at 100% corrected speed is examined. Results are compared against those of the linearized compressible analysis as well as experimental data. The same compressor operating at 70% corrected speed is also examined. As a further check, a three-stage high speed machine designed at NASA has been modeled at conditions corresponding to 80% corrected speed and the results compared with the linearized analysis.

3.2 Test case 1: Hypothetical single-stage low speed compressor

Comparison has been carried out between the current compressible calculation and the incompressible computation done by Gong for a hypothetical single-stage compressor. The capabilities of the two models are:

current model	Gong's model
compressible	incompressible
IGV,rotor, stator & inter-row gaps	lumped compressor
bodyforces in x and y directions	bodyforce in x direction only
allow circumferential velocity	no circumferential velocity
inside blade rows	

Two calculations were done using same overall compressor characteristic, same operating condition, same inertia, same initial perturbation structure, and same grid points in the circumferential direction.

The overall total-to-static compressor characteristic ψ is:

$$\psi(\phi) = -5.76\phi^3 + 4.32\phi^2 + 0.3 \qquad (3.1)$$

The operating point is at $\phi = 0.49, \dfrac{d\psi}{d\phi} = 0.08$, shown in figure 3.1. The rotor inertia parameter is set to 1.08 , and the compressor inertia parameter is set as 2.0.

A time history of the inlet axial velocity at four circumferential positions around the compressor is given in figure 3.2a and figure 3.2b for the present numerical simulation (run at a blade Mach number of 0.2) and the incompressible calculation of Gong. As can be seen, there is good agreement between the two.

A time history of the first (most important) spatial fourier component of the axial velocity non-uniformity is given in figure 3.3 for both methods. Good agreement exists in the pre-stall region for which the amplitude is less than 0.08.

There is less agreement between the two in the region with amplitude larger than 0.08, but the results are quantitatively similar. It is thought that the main reason for the discrepancy is associated with the different manner in which the two methods specify the bodyforces.

By calculating the slope of the amplitude in figure 3.3 (the region with the amplitude less than 0.08), we obtain a growth rate of 0.02 for both methods. Similarly, we can calculate the rotating frequency of the first spatial harmonic of flow coefficient by taking the slope of the phase of this component shown in figure 3.3. This is about 0.27 for both calculations.

We can also use the model of [4] to calculate the growth rate and rotating frequency of the first harmonic in this case. The formulae are

growth rate $$\alpha = \frac{\dfrac{d\psi}{d\phi}}{\dfrac{2}{|n|} + \mu}$$

rotating frequency $$\frac{\omega}{n} = \frac{\lambda}{\dfrac{2}{|n|} + \mu}$$

Since here $\dfrac{d\psi}{d\phi} = 0.08$, $\lambda = 1.08$, $\mu = 2.0$, n=1, we get:

$$\begin{cases} \alpha = 0.02 \\ \omega = 0.27 \end{cases}$$

The growth rate and wave frequency are the most important quantitative features of the stall inception and there is good agreement among the three models for these quantities.

From the linear point of view, if the initial circumferential perturbation is small enough, we should see a linear region where different modes evolve independently and different harmonics travel at different speeds as predicted by the linear model. As a further check therefore, a simulation with the first five

harmonics at a level of 0.01% of mean flow as an initial perturbation was carried out. The time history of the first three Fourier components of flow coefficient is shown in figure 3.4, in which (a) shows the phases of the three harmonics, and (b) shows the slopes of the phases which tell the rotating speeds of these harmonics. Here we see a clear linear region before 12 rotor revolutions (perturbation less than 0.2% of mean flow), in which the rotating speeds of the first, second and third harmonics are about 0.276, 0.359, 0.400, respectively. The model of [4] predicts:

$$\frac{\omega}{1} = \frac{\lambda}{\frac{2}{|1|} + \mu} = 0.270(1st)$$

$$\frac{\omega}{2} = \frac{\lambda}{\frac{2}{|2|} + \mu} = 0.360(2nd)$$

$$\frac{\omega}{3} = \frac{\lambda}{\frac{2}{|3|} + \mu} = 0.405(3rd)$$

The biggest difference between the analytical model and the numerical calculation is 2%.

There is a transient period between 12 and 50 rotor revolutions, where the harmonics start to interact, showing a change in phase speeds, especially for the third harmonic. After 50 rotor revolutions (perturbation bigger than 8% of mean flow), these three harmonics are coupled with the phase speeds "locked", as seen in figure 3.4 (b).

3.3 Test case 2: a four-stage high speed compressor operated at 100% corrected speed.

This four-stage high speed compressor has been tested at the Wright laboratory. The mean flow has been simulated using a mean-line generation

code of Pratt & Whitney (we will refer to this as "PWmean"). Based on this mean flow, a stability analysis is performed by using the linearized compressible model of Hendricks [13]. Both the mean-line calculation and stability calculation are conducted using the current model, then compared against the mean flow calculated by PWmean and linearized stability analysis, as well as experimental data.

The geometry of the compressor is given in Appendix 2. Taking the geometry and blade row characteristics (total pressure rise, efficiency (rotor), flow angle (stator)) given by PWmean as inputs, a steady-state mean flow calculation can be performed for each throttle setting greater than a critical value below which an axial oscillation involving the whole compression system (surge) would happen. Starting from a throttle setting which sets the operating point far away from the instability (surge) point, the mean flow calculations can be carried to the instability point by gradually decreasing the throttle area.

Comparison of the calculated and input overall total pressure rise characteristics is shown in figure 3.5. Comparisons of total pressure, static pressure, total temperature and flow coefficient axial distributions from current calculation and PWmean at two different operating points are shown in figure 3.6 and 3.7. PWmean gives values only at the leading and trailing edges of each blade row. In figure 3.5, the maximum discrepancy between the two methods is about 2.5% of the total pressure rise. Figure 3.6 and 3.7 show that the two methods give almost the same values at leading and trailing edges of each blade row for the four variables. The shape of the flow coefficient distribution inside the blade row calculated by the current model results from the sinusoidal bodyforce distribution inside the blade row.

47

The discrepancy in figure 3.5 occurs due to the following. As stated in chapter 2, the source terms are formulated in such a way that the total pressure rise across each blade row should be specified as a function of local flow coefficient at each axial grid point. Theoretically no matter what kind of flow coefficient distribution inside a blade row, every point should give the same blade loading (total pressure rise) for an operating condition. From PWmean, we can get the total pressure rise characteristic as a function of the leading edge flow coefficient for each blade row. Based on this, the local pressure rise characteristics are generated according to the flow coefficient distribution inside a blade row to ensure that the blade loading given at each grid point is close to that of leading edge. It is very difficult, however, to make them exactly the same.

For example, at one operating condition where the inlet Mach number is 0.374 as shown in figure 3.7, we can examine the first rotor. If we take five points along the axial direction and mark them on a flow coefficient plot (figure 3.8), then plot the five corresponding local characteristics (figure 3.9) and look up the pressure rises given by these five points in figure 3.8, we see that they are not exactly the same. The average value is also below the specified value at inlet of this rotor (marked on line 1 in figure 3.9). This is the main reason for the discrepancy between the calculated and specified pressure rises.

The steady-state mean flow can be calculated at throttle areas larger than the critical value. At this throttle setting (marked * in figure 3.5), the flow field is stable. Further decreasing the throttle area causes instability because a small axial oscillation evolves into a large amplitude axial oscillation. We call this operating point the "surge point". The surge behavior of this case is shown in

figure 3.10, which gives the time history of the flow coefficient at the inlet of the compressor.

To see the rotating-stall type of instability, we need to put a circumferential perturbation into the steady-state flow field. The way to do this is to superimpose small amplitude circumferential perturbations, which can include an arbitrary harmonics distribution, on the quasi-steady axisymmetric pressure rise characteristics. The response of the system to this initial perturbation is then tracked. At the operating point where we saw the surge-type of instability, a small initial circumferential perturbation was put into the mean flow field, and a time history of the inlet flow coefficient (with the mean value subtracted) at four circumferential positions is shown in figure 3.11. The disturbances decay, but they are clearly traveling waves with rotating speed near 100% of rotor speed.

It is difficult to tell whether the surge or rotating stall happens first using the current nonlinear calculations because the throttle closing rate may not be small enough in unsteady calculations. However we can use the linearized stability model to address this part. Using the mean line information from PWmean and the same geometry, the eigenvalues for n=0 (surge type) and n=1 (rotating stall type) are plotted in figure 3.12. The plot gives contours of real and imaginary parts of the dispersion equation, representing the eigenvalues of the linear system. As the least damped eigenvalue reaches the imaginary axis, the system becomes neutrally stable. In figure 3.12, we see that surge occurs at an operating condition where inlet Mach number is 0.3610, and rotating stall happens at an operating condition with inlet Mach number of 0.3556. Surge thus occurs before rotating stall.

In figure 3.12, for n=1 (the lower plot), there are two eigenvalues with different rotating frequencies. One is about 1 rotor frequency, another is about 0.45 rotor frequency. These have almost the same growth rate, in other words, the so-called (1,1) mode and (1,0) mode have zero damping almost simultaneously. Note that in the compressible flow field, each harmonic of the flow variable consists of an infinite number of modes and they are all independent. In figure 3.12, each graph only includes the least damped modes, i.e. modes with growth rate close to zero.

It is of interest to study these two modes and a three-dimensional "waterfall" spectral plot provides a convenient way to do this [12]. Here, the power spectrum of a spatial harmonic is calculated over a window of fixed period. The window is then marched forward in time and the process repeated. The result is the variation of the rotating spatial wave spectral distribution over time.

The results shown in figure 3.12 have been reduced using this technique for the first harmonic, and the three-dimensional "waterfall" plot is shown in figure 3.13. We see that there are two waves traveling at different speeds, one at about 1.0 rotor speed and the other at much lower speed of about 0.15. They contain about the same amount of energy. To confirm that the 100% rotor frequency mode is the (1,1) mode in the linear analysis, the axial structure of the shaft frequency component of the axial velocity disturbances is compared with that of (1,1) mode predicted by the linearized analysis. Figure 3.14 presents the amplitude and phase of this mode at the leading and trailing edges of the nine blade rows for both methods.

The two calculations match well in terms of both amplitude and phase. The small discrepancy may be due to the different level of details that these two

methods model the flow within the blade row. In particular, the linear compressible model treats the blade row as an actuator disk, whereas the current method models the flow inside the blade row, as required by the numerical scheme used. The inlet and the exit of the compressor are essentially "out of phase", which is an important effect of the compressibility. The incompressible mode has no variation of phase along the axial direction (as seen later in case 3).

At an operating point which is 1.5% in inlet Mach number away from the linear instability point, a circumferential disturbance traveling at the shaft speed (the so-called once per revolution forcing) was input to examine the effect of the forcing. The magnitude of this shaft speed forcing corresponds to 1% of the mean total pressure rise across each blade row. For large enough amplitude of this once per rev. forcing (1.4% of the mean flow in this case), the compression system goes into rotating stall.

Figure 3.15 is the time history of the first three spatial fourier components of the axial velocity. The upper plot is the phase and the lower plot is the logarithm of the amplitude. The stall inception period is very short (only 3 rotor revolutions), which is not long enough to show a clear picture of the stall inception, but the fully developed rotating stall cell travels at about 40% of rotor frequency.

To see a clear picture of the stall inception, a calculation with once per rev. disturbance was done as the throttle was slowly closed from a stable condition. A time history of the first three harmonics of the axial velocity is shown in figure 3.16, and a three-dimensional "waterfall" plot is shown in figure 3.17. In figure 3.16, the prestall wave of the first harmonic travels at 100% of rotor frequency, then changes to 40% when it evolves into rotating stall. After about 5 rotor

revolutions, the circumferential disturbances are surpressed and the flow goes into a surge cycle.

Figure 3.17 shows the first harmonic wave energy grows before the fully developed rotating stall, while figure 3.18 is the same plot using experimental data for this compressor at 100% corrected speed [12]; the two are similar. Because the spectral plot does not allow an abrupt change of the amplitudes of signals, it can not show the transient behavior from the stall inception to the fully developed stall. The rotating speed of the fully developed stall was measured as about 50% of rotor frequency in the experiment, which is close to the calculated value. The data also show that the flow went into surge after a very short period of rotating stall.

The conclusions from the above comparisons are:

1) Compressibility is important in this case. The compressible mode rotates at the rotor frequency and has an axial structure in which the inlet and exit are "out of phase".

2) The system exhibits stall at a linearly stable operating point with once per revolution forcing of sufficient amplitude.

3.4. Test case 3: Four-stage high-speed compressor operating at 70% corrected speed.

The geometry of this compressor at this speed is given in Appendix 2. The mean line calculation is performed as in case 2. Comparison of the calculated and input overall total pressure rise characteristic is shown in figure 3.19. Comparisons of total pressure, static pressure, total temperature and flow coefficient axial distributions from the current calculation and PWmean at one operating condition are given in figure 3.20. Comparisons of the adiabatic

efficiencies for the four stages is shown in figure 3.21 (solid line for input and dashed line for calculated results). As in case 2, there is good agreement between the two methods for steady-state quantities.

For the stability calculation, the same procedure as case 2 was carried out with similar results were obtained. Surge was also observed with a finite closing rate of the throttle area. With an initial small amplitude circumferential perturbation in the mean flow field, a time history of the inlet axial velocity at four circumferential positions is shown in figure 3.22. The disturbances decay with the wave traveling at about 15% of rotor speed. Figure 3.23 is the root locus for the linearized analysis for n=0 (surge type) and n=1 (stall type). Surge is predicted to occur before rotating stall.

A power spectral density analysis of the results shown in figure 3.22 shows only one wave traveling at about 15% rotor frequency. Figure 3.23 shows that only one mode ((1,0) mode) has very low damping. However the frequency of this mode is about 45% of rotor frequency, which is different from that of the nonlinear calculation. Comparison of the axial structure of the (1,0) mode and 0.15 frequency mode (figure 3.24) shows that they are very similar.

The reason for the difference of the rotating speed may be that the methods which the two models calculate the unsteady behavior of the compression system are different. Here we are trying to put it in a very simple way. The linear incompressible theory tells that $\frac{\Delta \delta P_t}{\delta \phi}$ of each blade row determines the eigenvalues. In the linearized model, this term is just a function of the leading edge mean flow coefficient, but in the current model, it is a function of both the local flow coefficient and its perturbation. As explained in section 3.3, the mean flow coefficient in a blade row changes substantially, so it is

53

difficult to keep each grid point operate at the same operating condition. As shown in figure 3.24, the perturbation of the flow coefficient also changes very much across a blade row (In the IGV, it changes more than 30% from leading to trailing edge), so the term $\dfrac{\Delta\delta P_t}{\delta\phi}$ given by each grid point can be very different from that of the leading edge. The prediction of the eigenfrequency from these two models could thus be different. (If we recall the calculation of case 2 (100% corrected speed), we also saw a mode at 15% rotor frequency (figure 3.14)).

A question to be answered is then whether this 15% rotor frequency mode exist in the real compressor. The data from the paper of Tryfonidis et al[12] helps answer this question. Figure 3.25 is the three-dimensional "waterfall" plots of the first harmonic of flow coefficient of this 4-stage compressor at 70%, 80%, 90% and 100% corrected speeds. Two other waves are discernible besides the one rotor frequency wave in all the four speeds. One of these two waves has the frequency close to 15% of rotor frequency, so there is a wave traveling at low speed in the compressor.

To see the effect of external forcing, a calculation with once per rev. disturbance is done as the throttle is slowly closed from a stable condition. A time history of the first three harmonics of the inlet axial velocity is shown in figure 3.26. The prestall wave of the first harmonic travels at 100% rotor frequency, then changes to 35% when it goes into the rotating stall. Figure 3.27 is the three-dimensional "waterfall" plot for n=1. Just before stall, the low frequency mode grows quickly, while the rotor frequency mode does not change much. It thus appears that the low frequency (incompressible) mode goes into stall first in this case. This is different from the last case where the rotor frequency mode grew substantially prior to stall.

From the above results, several points can be made here:

(1) Compressibility is not important in this case.

(2) Rotating stall occurs at a linearly stable operating point with external forcing of sufficient amplitude.

3.5 Test case 4: NASA three-stage compressor operating at 80% corrected speed

The mean line geometry for the NASA 3-stage high speed compressor is in Appendix 2. The mean line calculation is performed in the same way as in the above cases. Comparisons of the mean flow as the above cases were conducted, with similar results. Figure 3.28 and 3.29 are the comparisons of the input and calculated overall total pressure rise characteristics and the axial distributions of the four flow variables from current calculation and PWmean, respectively.

Only one stability calculation was performed in this case. A circumferential perturbation is superimposed on a steady-state flow field initially and the response of the system to this initial perturbation is then tracked. A time history of the first three harmonics of the inlet axial velocity is shown in figure 3.30. The perturbation is slowly decaying, and the phase speed (rotating speed) of the first harmonic is about 45% of rotor speed in the negative direction. The eigenvalue plot for the linearized stability calculation for n=1 and inlet Mach number Min=0.3728 is shown in figure 3.31. The mode with the highest growth rate has the rotating speed of 43% and also travels in the negative direction.

3.6 Discussion

The above tests give confidence in the current method. For the most part, the results agree with the linearized analysis in the linear region. Some results,

however exhibit strong nonlinear behavior prior to stall when the disturbance level gets large. Figure 3.16 shows the second and third harmonic start growing before the first harmonic does, although the first harmonic dominates in the whole transient process. This may be the reason the transient is so abrupt. Figure 3.32 are the first and second Fourier coefficients of experimental data of the 4-stage compressor at 100% corrected speed[12], which show the similar trend as in figure 3.16. The second harmonic starts growing earlier than the first does, supporting the current calculation.

An interesting phenomenon seen in both the current result and experimental data is that there is a high frequency small amplitude wave superimposed on all harmonics. And as one approaches stall, this wave grows in amplitude. Two questions are thus:

1. What is this wave?

2. What is the effect of this wave on stall inception?

To address these, the axial structure of the wave in the zeroth and first harmonics of the flow coefficient was examined. By performing a Fourier decomposition of the zeroth harmonic in time at one axial location, we can get the amplitude and phase of this (1.6 rotor frequency) component at this axial location. The axial distribution of the amplitudes of this mode is thus obtained by repeating the same procedure along the axial direction of the system. Figure 3.33 is a plot of the amplitudes and phases of this mode of the zeroth harmonic. The figure shows that there are about five standing waves in the whole system. The wave in the region of the compressor (the compressor is between 10 and 11 along axial direction) is the strongest, indicating that the compressor is likely the source of this wave. The length of the compressor is roughly the half length of

the standing wave, indicating that the frequency of this wave is set by the compressor geometry.

Calculating the natural frequency of the acoustic wave in an organ pipe based on the geometry of the system [23], we find that the number of these wave with 1.6 rotor frequency should be five in the system. The standing wave number seen in figure 3.33 thus matches with the natural acoustics of the system. The standing wave observed is thus an acoustic wave, and the 1.6 rotor frequency mode is an acoustic mode.

Figure 3.34 is the amplitude distribution of the acoustic mode in the first harmonic. It is very similar to that of the zeroth harmonic. Combining the fact that all higher harmonics have the same frequency as the zeroth harmonic, it is possible that the harmonics interact with each other through nonlinear effects.

The amplitude of this mode gets large as the operating point approaches stall, so it may make a contribution to the onset of rotating stall. Acoustic instability has been studied by Gysling et al[23], who found that the mechanism responsible for the acoustic instability, i.e. the compressor feeding energy into the disturbance, is similar to the mechanism responsible for rotating stall and surge. Here, it is also seen that acoustic waves can be coupled with rotating stall.

Chapter 4. The Investigation of the Forcing Effect on Compressor Instability

4.1 Introduction

The aerodynamic forced response of a compressor can be an important factor in establishing stability. A compression system can be driven unstable when in a normally stable operating regime by external forcing of sufficient amplitude. In this it is not the damping ratio alone, but the increased perturbation level associated with low damping ratios combined with degradation of the nonlinear resistance to such perturbations, which determines the rotating stall inception point [16]. In this chapter we investigate how the stall inception point changes with level and type of external forcing.

4.2 The effect of forcing (once per revolution disturbance) level on stall inception

Forcing here refers to a non-uniformity created by such features as non-uniformity of tip-clearance. There can have a level up to several percent of the mean flow quantities. Forcing with shaft frequency has been seen in almost all compressors, and calculations were carried on to see the effect of such forcing on stall. The forcing is implemented in the same way as in section 3.3, i.e. a circumferential disturbance is superimposed on the mean steady-state total pressure rise characteristic of each blade row. One percent in forcing means a non-uniformity of one percent of the mean total pressure rise across a blade row. A series of such calculations at different operating points then gives us a picture

of the change in stall inception point with forcing level. The result is shown in Figure 4.1 as the solid line. The figure shows that the change in stall inception point increases with the amplitude of forcing. For example, 4.5% in forcing causes about 4.6% change of stall inception in flow coefficient away from the linearized instability point.

4.3 The effect of forcing structure on stall inception

Another type of forcing is stationary distortion. A series of calculations has also been carried out with stationary distortions and results are also shown in figure 4.1. Stationary forcing triggered rotating stall at smaller amplitude than the once per revolution forcing. This seems surprising because the latter is expected to be close to one of the resonances of the system. The steady-state characteristics of the compressor with both a once per revolution and a stationary forcing are plotted in figure 4.2. The characteristic with stationary forcing is seen to be more severely degraded from the uniform flow situation, consistent with the larger effect of stationary forcing.

A central question is thus why the system has a stronger response to stationary than to once per revolution forcing. One part of the answer is associated with the resonances of the system. To find these, calculations were carried out using a first harmonic sinusoidal forcing containing a spectrum of frequencies in both positive and negative directions of rotor rotation. The PSD of the time history of the inlet flow coefficient shows that there are two peaks in both positive and negative directions of the frequency axis, as shown in figure 4.3. Neither the stationary forcing nor once per revolution forcing appears at a resonance of the system.

We can also compare the response of the system to 0.9 shaft frequency forcing with that to stationary and once per revolution forcing, when all forcings are only the first spatial harmonic sinusoidal perturbations (The amplitude used was 0.2% of mean value, about 0.7% of inlet dynamic head). The response to 0.9 rotor frequency forcing was stronger than for once per revolution forcing, but smaller than from stationary forcing.

Figure 4.4 is the time history of the amplitudes of the first three spatial Fourier harmonics of inlet flow coefficient for cases with stationary forcing and 0.9 rotor frequency forcing. The forcing is first harmonic only. The second and third harmonics in the case with stationary forcing are larger than with 0.9 rotor frequency forcing while the first harmonic stays about the same level, showing that the nonlinearity level in the former case is much larger than the latter case.

Another difference between the two cases is that there is a low frequency (~0.7% rotor frequency) oscillation seen in all three harmonics with stationary forcing. This frequency is about the surge frequency of the system predicted by linear analysis (see Fig. 3.12). As stated in chapter 3, surge is more unstable than rotating stall in this compressor. We thus propose that the degradation of the resistance to this level of stationary forcing arises because of nonlinear interaction with the surge mode of the system.

To further explore the idea that this effect is a nonlinear phenomenon, we need to decrease the amplitude of both the stationary forcing and 0.9 rotor frequency forcing to a level small enough to be in the linear region. We thus use 0.02% of inlet dynamic head and run the calculations again. This time the response of the system to stationary forcing is less than that to 0.9 rotor frequency forcing as seen in figure 4.5, which shows the time history of inlet flow coefficient around the whole annulus for both cases. The response for 0.9 shaft

frequency forcing has bigger magnitude. This means that the response of the system to 0.9 shaft frequency forcing is stronger than that for stationary forcing within the linear region, and therefore agrees with linear analysis.

Chapter 5. Summary and conclusions

A two-dimensional nonlinear compressible model has been developed to examine stability in high speed multistage compressors. Computational implementation of this model allows the investigation of both rotating stall and surge. The model has been applied to two high speed multistage compressors and compared with existing experimental data. The model has also been used to investigate the effect of external forcing on stall inception.

Some specific conclusions are as follows:

1. For the compressor examined here the compressible mode was important at 100% corrected speed. This mode rotates at near shaft speed and has an axial structure in which the inlet and exit of the compressor are "out of phase".

2. Simulation of this 4-stage compressor at 70% corrected speed shows that compressibility is much less important.

3. The system exhibits rotating stall at operating points that are linearly stable if extend forcing is of sufficient amplitude. For example, rotating stall occurs at an operating point 1.5% away (in mass flow) from the linear instability point when the amplitude of once per revolution forcing is about 1.2% of the mean total pressure rise across each blade row.

4. The response of this system to stationary forcing becomes stronger than that of once per revolution forcing if the amplitude of the forcing becomes large enough.

Recommendations for future work

Further comparisons and testing with experimental measurements on real engines are essential to assess the range of validity of the current model.

Two specific questions can also be identified:

1. When does the compressible mode (rather than the incompressible mode) become unstable first and why?

2. Does thinking about stall onset from a dynamic point of view lead one to a different set of design guidelines than the current "steady-state" approach?

These questions have an impact not only on understanding the basic unsteady fluid dynamics that characterizes the stall inception, but also on stall management and on development of schemes for active control. The simulation being developed should provide an excellent tool to answer these questions.

References

(1). Greitzer, E. M., " Surge and Rotating Stall in Axial Compressors, Part I: Theoritical Compression System Model", and "Part II: Experimental Results and Comparison with Theory". ASME *Journal of Engineering for Power*. April, 1976

(2). Moore, F. K. and Greitzer, E. M., "A Theory of Post-Stall Transients in Axial Compressors. Part I: Development of the Equations", ASME *Journal of Engineering for Gas Turbine and Power*, Vol. 108, pp.68-76, January, 1986.

(3). Greitzer, E. M. and Moore, F. K., "A Theory of Post-Stall Transients in Axial Compressors. Part II: Applications", ASME *Journal of Engineering for Gas Turbine and Power*, Vol. 108, pp.231-239, January, 1986.

(4). Hynes, T. P. and Greitzer, E. M., "A Method for Assessing Effects of Circumferential Flow Distortion on Compressor Stability", *Journal of Turbomachinery*, Vol. 109, pp.371-379, July 1987.

(5). Garnier, V. H., Epstein, A. H., Greitzer, E. M., "Rotating Waves as a Stall Inception in Axial Compressors", *Journal of Turbomachinery*, Paper No. 90-GT-156, April 1991.

(6). Day, I. J., Freeman, C., "The Unstable Behavior of Low and High Speed Compressors", ASME, *Journal of Turbomachinery*, Vol.116, No.2, pp.194-201, April, 1994.

(7). Wilson, A. G., Freeman, C., "Stall Inception and Development in an Axial Aeroengine", ASME, *Journal of Turbomachinery*, Vol.116, No.2, pp.216-225, April, 1994.

(8). Hoying, D. A., "Stall Inception in a Multistage High Speed Axial Compressor", Paper of 29th Joint Propulsion Conference and Exhibit, Monterey, CA, 1993.

(9). Boyer, K. M., King, P. I., and Copenhaver, W. W., "Stall Inception in Single Stage, High-Speed Compressors with Straight and Swept Leading Edges", Paper of 29th Joint Propulsion Conference and Exhibit, Monterey, CA, 1993.

(10). Hendricks, G. J., Bonnaure, L. P., etc. "Analysis of Rotating Stall Onset in High Speed Axial Flow Compressors", Paper of 29th Joint Propulsion Conference and Exhibit, Monterey, CA, 1993.

(11). Escuret, J. F., Garnier, V., "Numerical Simulation of Surge and Rotating Stall in Multistage Axial-Flow Compressors", Paper of 29th Joint Propulsion Conference and Exhibit, Monterey, CA, 1993.

(12). Tryfonids, M., Etchevers, O., Paduano, J. D., etc. "Pre-Stall Behavior of Several High-Speed Compressors", Paper of International Gas Turbine Congress and Exposition, The Hague, Netherland, 1994.

(13). Bonnaure, L. P., "Modelling High Speed Multistage Compressor Stability", MS Thesis, MIT Department of Aeronautics and Astronautics, September, 1991.

(14). Paduano, J. D., Gysling, D. L., "Modelling Axial Compressor Nonlinear Rotating Stall Phenomena for Control", MIT GTL paper.

(15). Chue, R. S., Greitzer, E. M., Tan, C. S., "An Analysis of General Post-Stall Transients in Axial Compression Systems", MIT GTL paper, May, 1987

(16). Mansoux, C., "Distributed Nonlinear Stability Analysis of Rotating Stall", MS Thesis, MIT Department of Aeronautics and Astronautics, May, 1994.

(17). Hale, J. K., LaSalle, J. P., "Differential Equations: Linearity vs. Nonlinearity", SLAM Review, Vol 5, No.3, July, 1963.

(18). Feulner, M. R., "Modelling and Control of Rotating Stall in High Speed Multistage Axial Compressors", Ph. D Thesis, Department of Aeronautics and Astronautics, May, 1994.

(19). Horlock, J .H., Marsh, H., "Flow Models for Turbomachines", *Journal Mechanical Engineering Science*, Vol 13, No.5, 1971.

(20). Giles, M., "A Numerical Method for the Calculation of Unsteady Flow in Turbomachinery", GTL Report #205, 1991.

(21). Horlock, J. H., "Axial Flow Compressors", Robert E. Krieger Publishing Company, Malabar, Florida.

(22). Notes of course 16.160 (Computational Fluid Dynamics).

(23). Gysling, D. L., "Dynamic Control of Rotating Stall in Axial Flow Compressors Using Aeromechanical Feedback", GTL Report #219, 1993.

(24). Research by Gong, Y.F., 1993.

Appendix 1
Derivation of the one-dimensional Euler equation in stators with streamtube thickness R(x).

1. Continuity equation:

The control volume is shown in figure A1.1
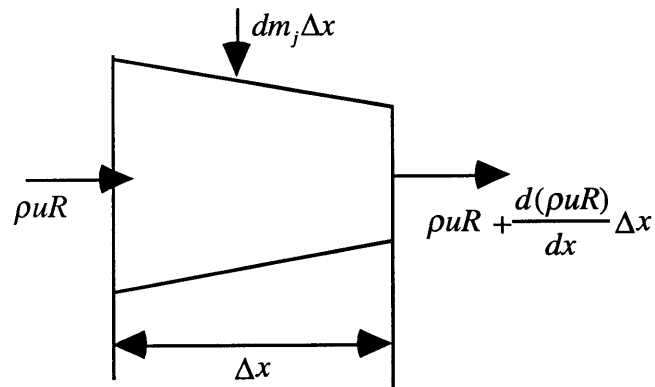
Figure A1.1 Control volume for mass flow conservation

mass of the fluid inside the control volume: $\rho R \Delta x$

rate of mass change with time: $\dfrac{\partial}{\partial t}(\rho R \Delta x)$

mass flow rate in: $\rho u R + dm_j \Delta x$

mass flow rate out: $\rho u R + \dfrac{d(\rho u R)}{dx} \Delta x$

rate of mass change=mass flow rate in - mass flow rate out

Thus

$$\frac{\partial}{\partial t}(\rho R \Delta x) = -\frac{d(\rho u R)}{dx}\Delta x + dm_j \Delta x$$

$$\frac{\partial(\rho R)}{\partial t} + \frac{\partial(\rho u R)}{\partial x} = dm_j \qquad (A1.1)$$

2. Axial momentum equation:

The control volume is shown in figure A1.2.
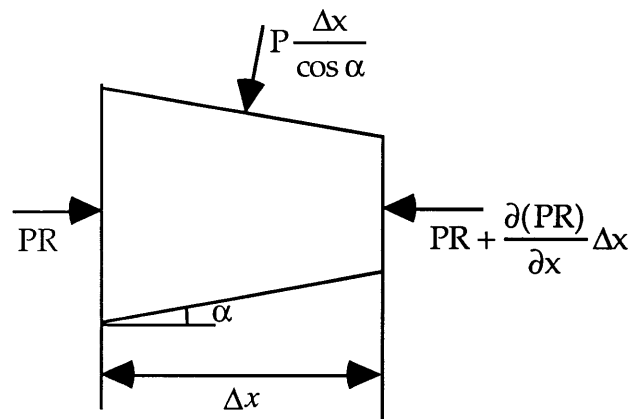
Figure A1.2 Control volume with pressure force on each face

Momentum of fluid enclosed: $\rho R \Delta x \cdot u$

Rate of change of momentum enclosed: $\dfrac{\partial}{\partial t}(\rho u R \Delta x)$

Axial component of pressure force=pressure force@inlet+pressure force@outlet

$$+\text{pressure force@wall}$$

$$=PR\text{-}\left(PR+\frac{\partial(PR)}{\partial x}\Delta x\right)\text{-}P\frac{\Delta x}{\cos\alpha}\cdot\sin\alpha$$

$$=-\frac{\partial(\rho R)}{\partial x}\Delta x+P\frac{\partial R}{\partial x}\Delta x$$

Momentum in: $\rho u R \cdot u + dm_j \Delta x \cdot u$

Momentum out: $[\rho u R + \dfrac{\partial(\rho u R)}{\partial x}\Delta x]\cdot[u+\dfrac{\partial u}{\partial x}\Delta x]\approx \rho u R\cdot u+\dfrac{\partial(\rho u^2 R)}{\partial x}\Delta x$

External force: $F_x \Delta x$

rate of momentum change=momentum in - momentum out + pressure force + external force

Thus

68

$$\frac{\partial(\rho uR)}{\partial t} = -\frac{\partial(\rho u^2R)}{\partial x} + dm_ju - \frac{\partial(\rho R)}{\partial x} + P\frac{\partial R}{\partial x} + F_x$$

i.e.
$$\frac{\partial(\rho uR)}{\partial t} + \frac{\partial(\rho u^2R + PR)}{\partial x} = P\frac{\partial R}{\partial x} + F_x + dm_ju \qquad (A1.2)$$

3. Circumferential momentum equation:

Momentum of fluid enclosed: $\rho R\Delta x \cdot v$

Rate of change: $\dfrac{\partial}{\partial t}(\rho vR\Delta x)$

Momentum in: $\rho uR \cdot v + dm_j\Delta x \cdot v$

Momentum out: $[\rho uR + \dfrac{\partial(\rho uR)}{\partial x}\Delta x] \cdot [v + \dfrac{\partial v}{\partial x}\Delta x] \approx \rho uR \cdot v + \dfrac{\partial(\rho uvR)}{\partial x}\Delta x$

External force: $F_y\Delta x$

Thus similarly, we obtain:

$$\frac{\partial(\rho vR)}{\partial t} + \frac{\partial(\rho uvR)}{\partial x} = F_y + dm_jv \qquad (A1.3)$$

4. Energy equation:

Internal energy of fluid enclosed: $\rho R\Delta x \cdot E$

Rate of change: $\dfrac{\partial}{\partial t}(\rho ER\Delta x)$

Bulk flow energy in: $\rho uR \cdot H + dm_j\Delta x \cdot H$

Bulk flow energy out: $[\rho uR + \dfrac{\partial(\rho uR)}{\partial x}\Delta x] \cdot [H + \dfrac{\partial H}{\partial x}\Delta x] \approx \rho uR \cdot H + \dfrac{\partial(\rho uHR)}{\partial x}\Delta x$

Heat addition: 0 (assume flow is adiabatic)

work exchange: 0

rate of internal energy change=energy in - energe out+heat addition+work

Thus

$$\frac{\partial(\rho ER)}{\partial t} + \frac{\partial(\rho uHR)}{\partial x} = dm_jH \qquad (A1.4)$$

69

Appendix 2
Compressor Geometry

In the following compressor geometry files:

ξ represents the stagger angle in degrees

θ^* represents the camber angle in degrees

σ represents the solidity

$\frac{t}{c}$ represents the thickness to chord ratio

c represents the non-dimensionalized chord length

RHLE represents the non-dimensionalized hub radius at the leading edge

RTLE represents the non-dimensionalized tip radius at the leading edge

RHTE represents the non-dimensionalized hub radius at the trailing edge

RTTE represents the non-dimensionalized tip radius at the trailing edge

A.2.1 EFC 4-stage compressor at 100% corrected speed

Blade Type	ξ	θ^*	σ	$\frac{t}{c}$	c	RHLE	RTLE	RHTE	RTTE
IGV	4.0	4.0	1.649	0.055	0.231	0.798	1.117	0.867	1.117
Rotor 1	48.4	17.1	1.590	0.055	0.223	0.867	1.117	0.922	1.117
Stator 1	19.4	54.2	1.630	0.055	0.168	0.922	1.117	0.951	1.117
Rotor 2	50.8	14.6	1.620	0.055	0.176	0.951	1.117	0.978	1.117
Stator 2	17.9	51.6	1.580	0.055	0.141	0.978	1.117	0.997	1.117
Rotor 3	51.9	17.7	1.550	0.055	0.148	0.997	1.117	1.018	1.117
Stator 3	19.4	53.6	1.550	0.055	0.123	1.018	1.117	1.028	1.117

Blade Type	ξ	θ^*	σ	$\dfrac{t}{c}$	c	RHLE	RTLE	RHTE	RTTE
Rotor 4	55.4	11.4	1.560	0.055	0.143	1.028	1.117	1.032	1.117
Stator 4	28.5	36.9	1.500	0.070	0.107	1.032	1.117	1.035	1.117

Rotational speed (non-dimensionalized)=0.972

A.2.2 EFC 4-stage compressor at 70% corrected speed

Blade Type	ξ	θ^*	σ	$\dfrac{t}{c}$	c	RHLE	RTLE	RHTE	RTTE
IGV	30.0	4.0	1.649	0.055	0.231	0.798	1.117	0.867	1.117
Rotor 1	48.4	17.1	1.590	0.055	0.223	0.867	1.117	0.922	1.117
Stator 1	29.4	54.2	1.630	0.055	0.168	0.922	1.117	0.951	1.117
Rotor 2	50.8	14.6	1.620	0.055	0.176	0.951	1.117	0.978	1.117
Stator 2	17.9	51.6	1.580	0.055	0.141	0.978	1.117	0.997	1.117
Rotor 3	51.9	17.7	1.550	0.055	0.148	0.997	1.117	1.018	1.117
Stator 3	19.4	53.6	1.550	0.055	0.123	1.018	1.117	1.028	1.117
Rotor 4	55.4	11.4	1.560	0.055	0.143	1.028	1.117	1.032	1.117
Stator 4	28.5	36.9	1.500	0.070	0.107	1.032	1.117	1.035	1.117

Rotational speed (non-dimensionalized)=0.68

A.2.3 NASA 3-stage compressor

Blade Type	ξ	θ^*	σ	$\dfrac{t}{c}$	c	RHLE	RTLE	RHTE	RTTE

IGV	15.29	0.0	2.000	0.100	0.299	0.689	1.233	0.689	1.233
Rotor 1	47.48	14.52	1.619	0.049	0.368	0.689	1.233	0.721	1.211
Stator 1	24.70	49.55	1.459	0.064	0.277	0.721	1.211	0.789	1.194
Rotor 2	45.36	16.39	1.468	0.061	0.289	0.789	1.194	0.851	1.179
Stator 2	25.43	51.09	1.417	0.065	0.191	0.851	1.179	0.888	1.173
Rotor 3	41.64	20.10	1.423	0.077	0.222	0.888	1.173	0.919	1.153
Stator 3	25.87	53.68	1.417	0.070	0.164	0.919	1.153	0.943	1.147

Rotational speed (non-dimensionalized)=1.0163
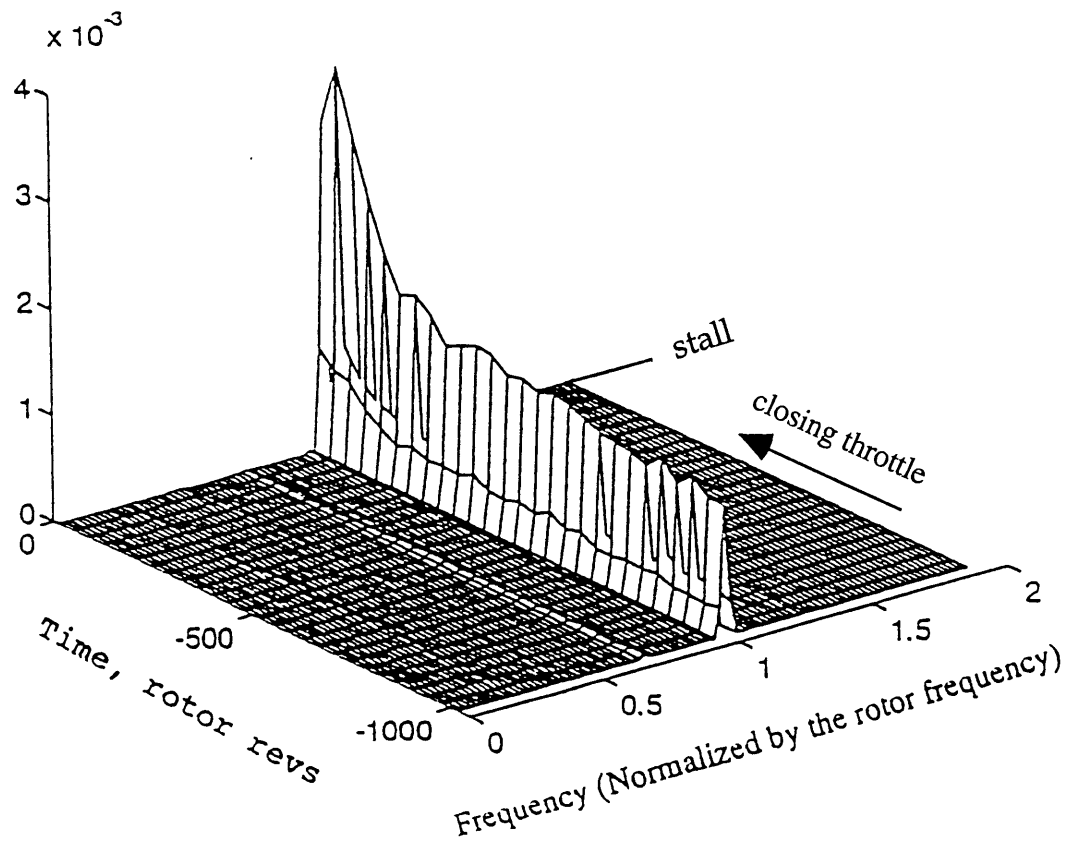
Figure 1.1   Power spectral density plot of experimental data of
4-stage compressor at 100% corrected speed
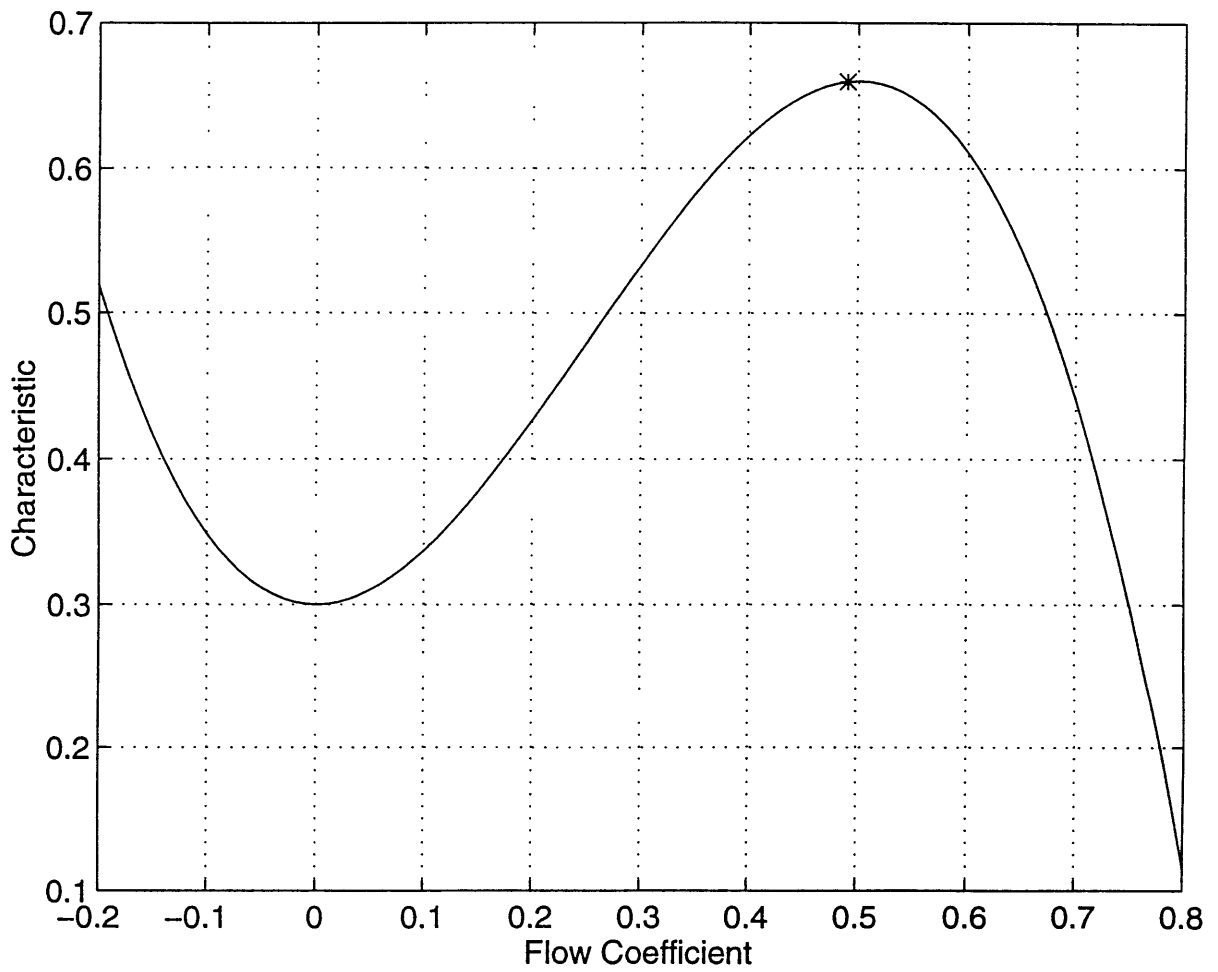
Figure 3.1 The overall compressor characteristic and the

operating point
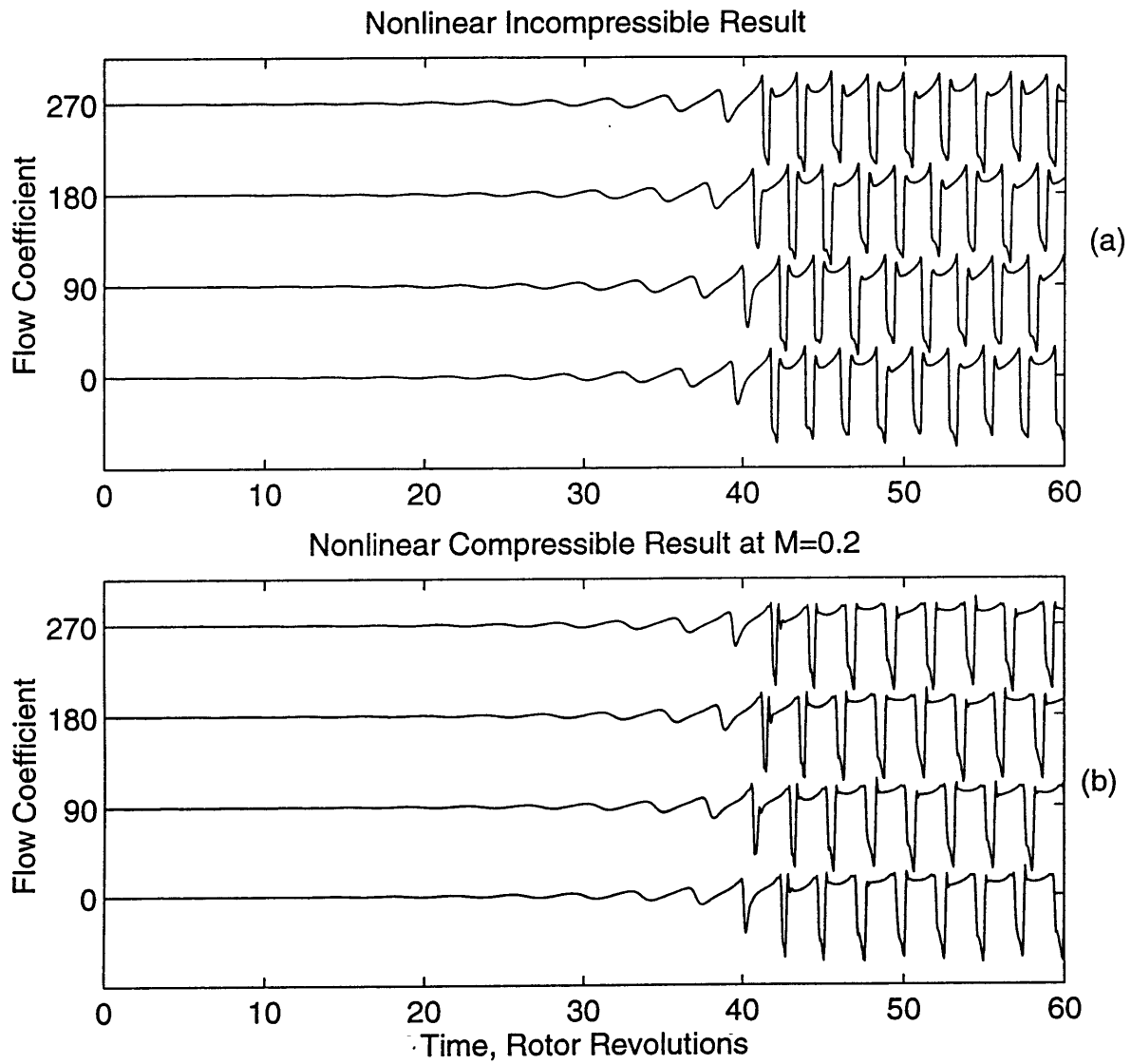
Figure 3.2   Time history of compressor inlet flow coefficient at

four circumferential locations
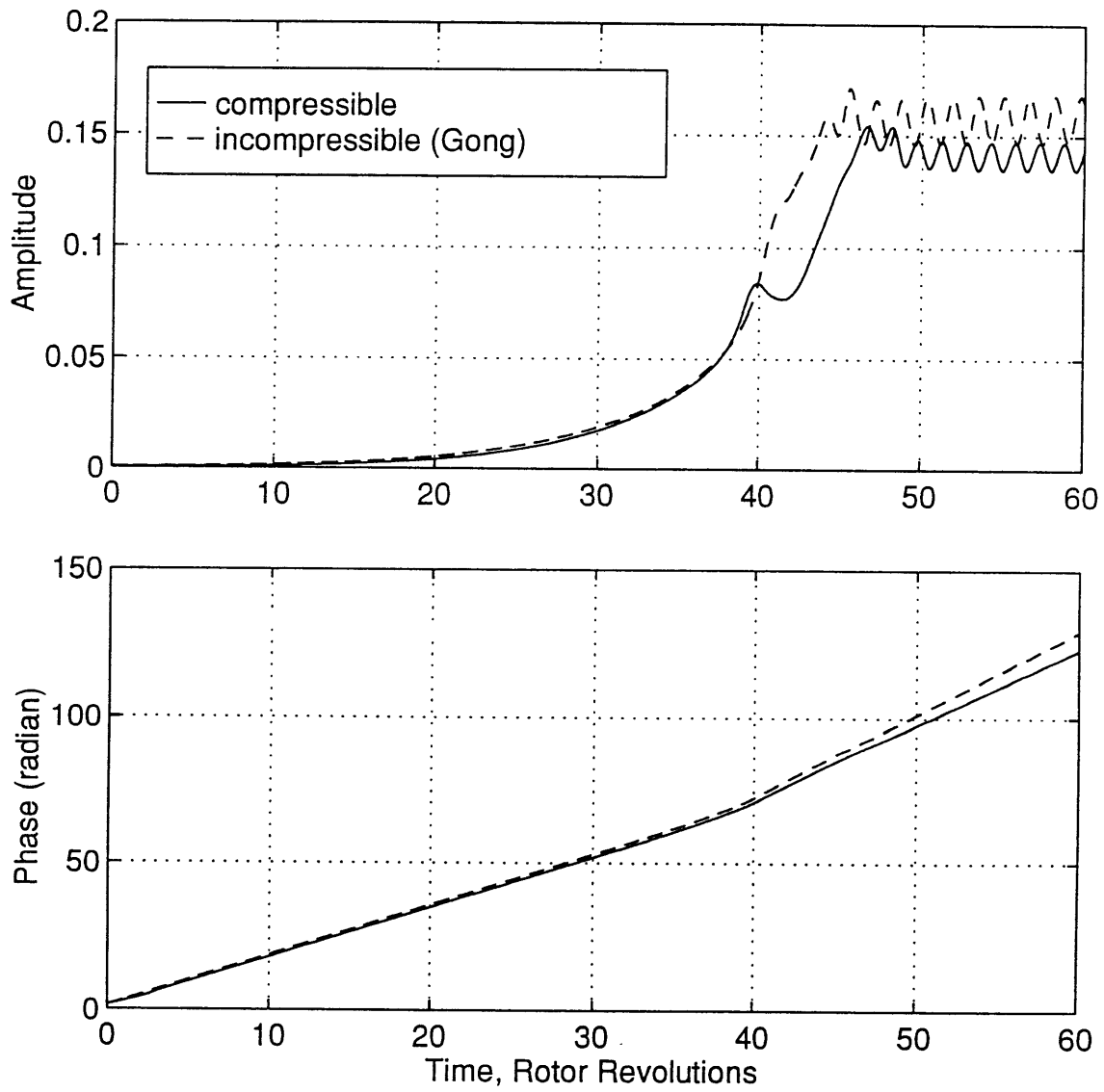
Figure 3.3   Time history of first spatial fourier component of flow

coefficient
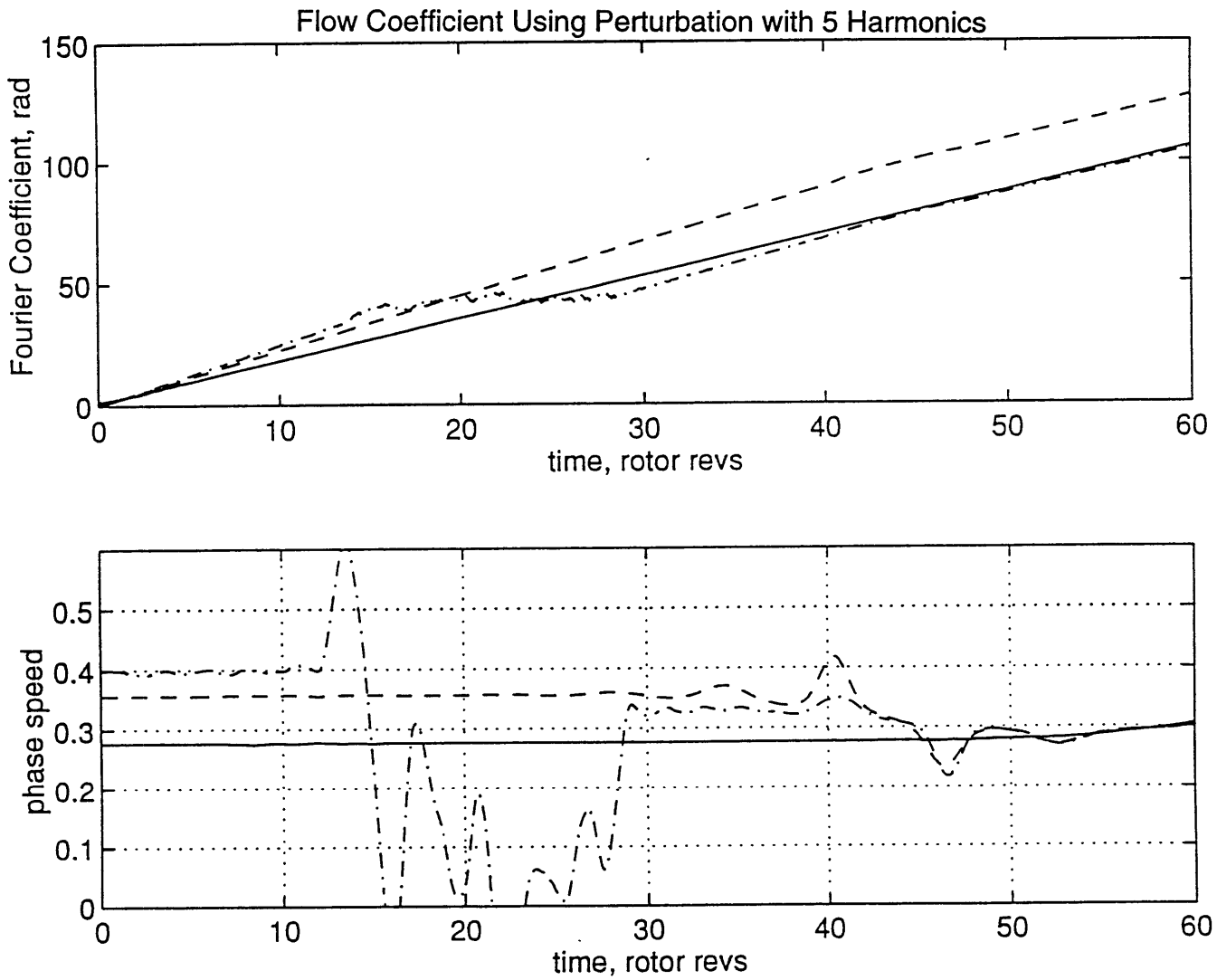
Figure 3.4   Time history of first three harmonics (solid-1st, dashed-2nd, dash-dotted-3rd) of inlet flow coefficient

77
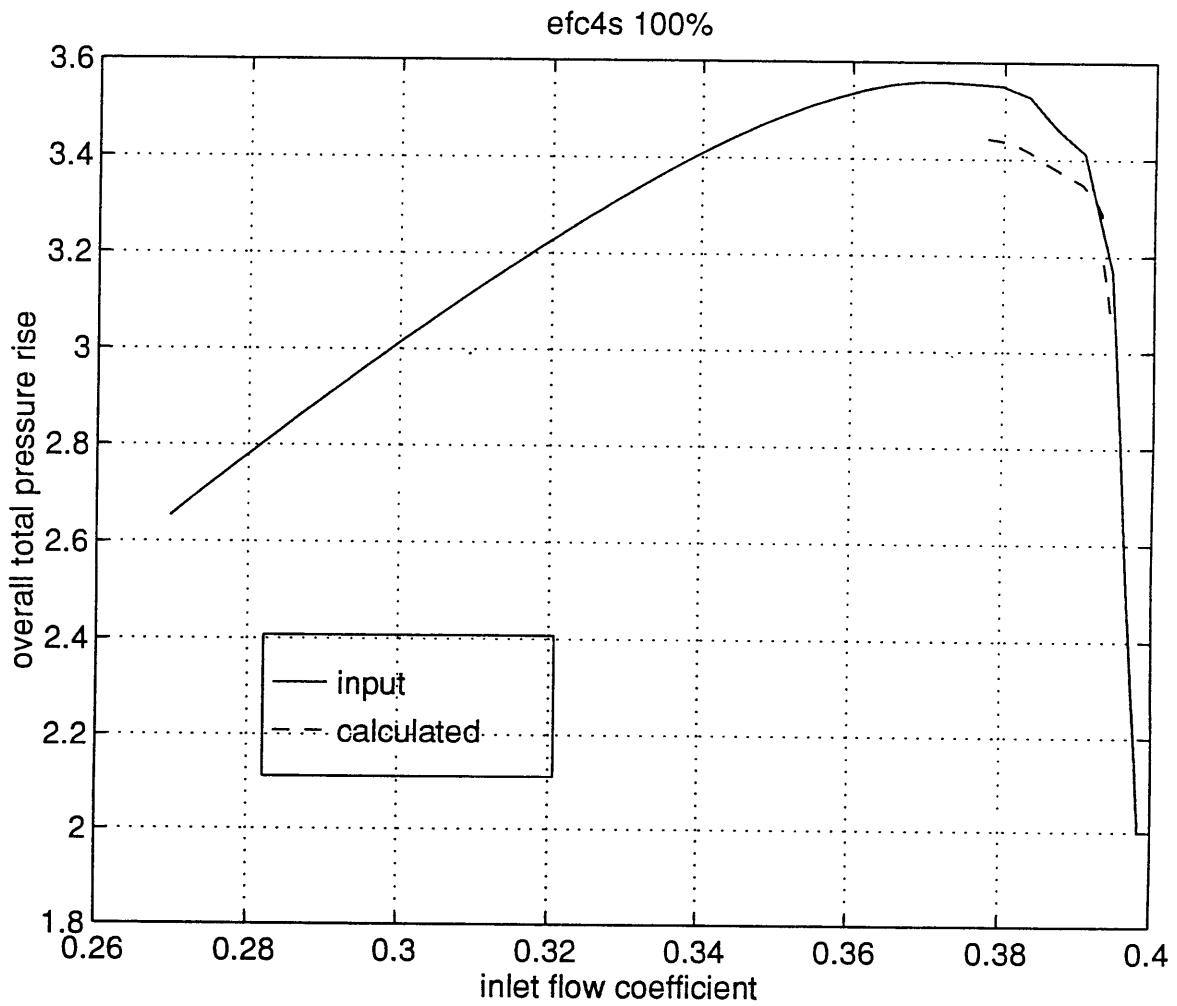
Figure 3.5   Comparison of input and calculated overall compressor

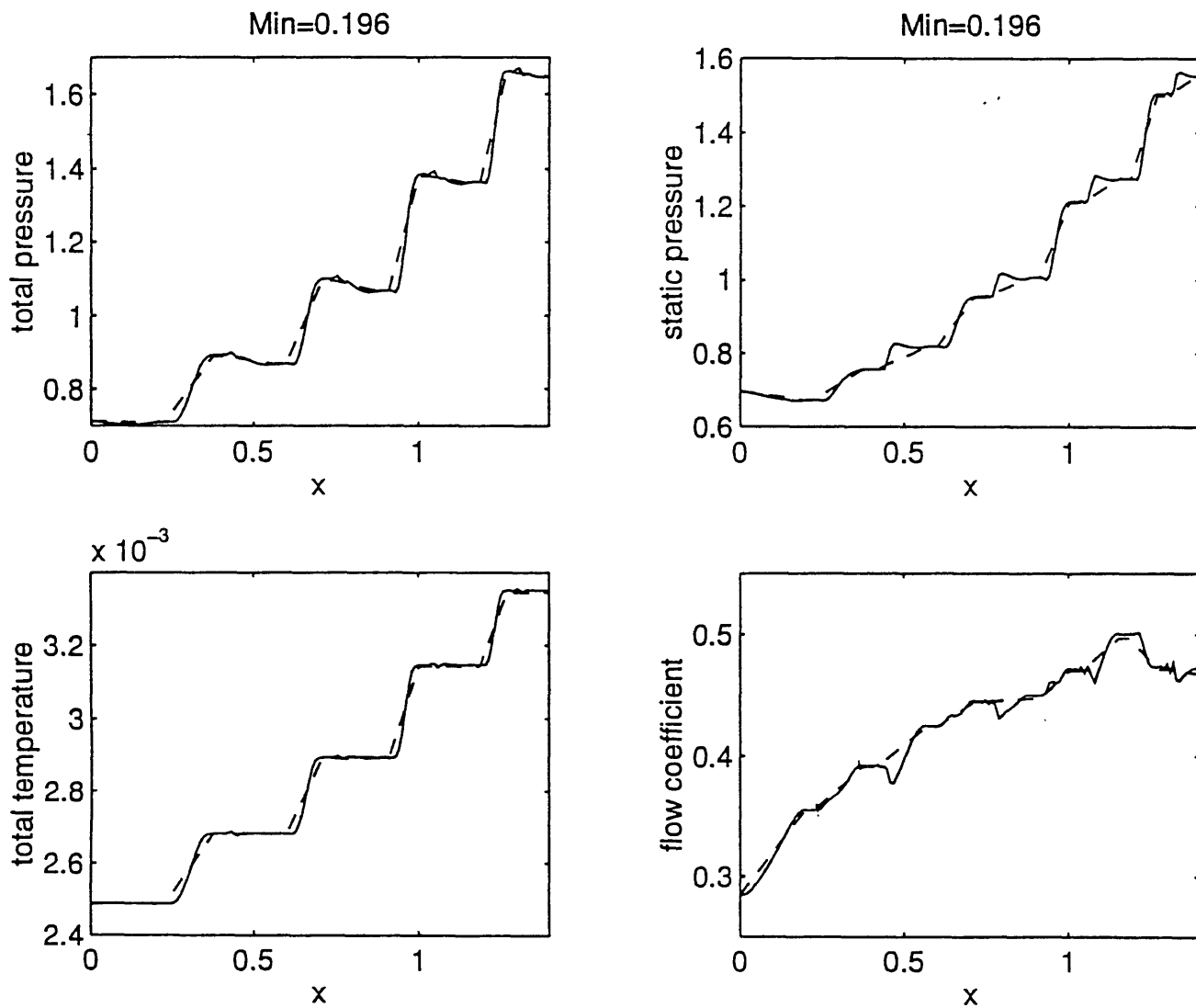characteristic of the 4-stage compressor at 100%

corrected speed
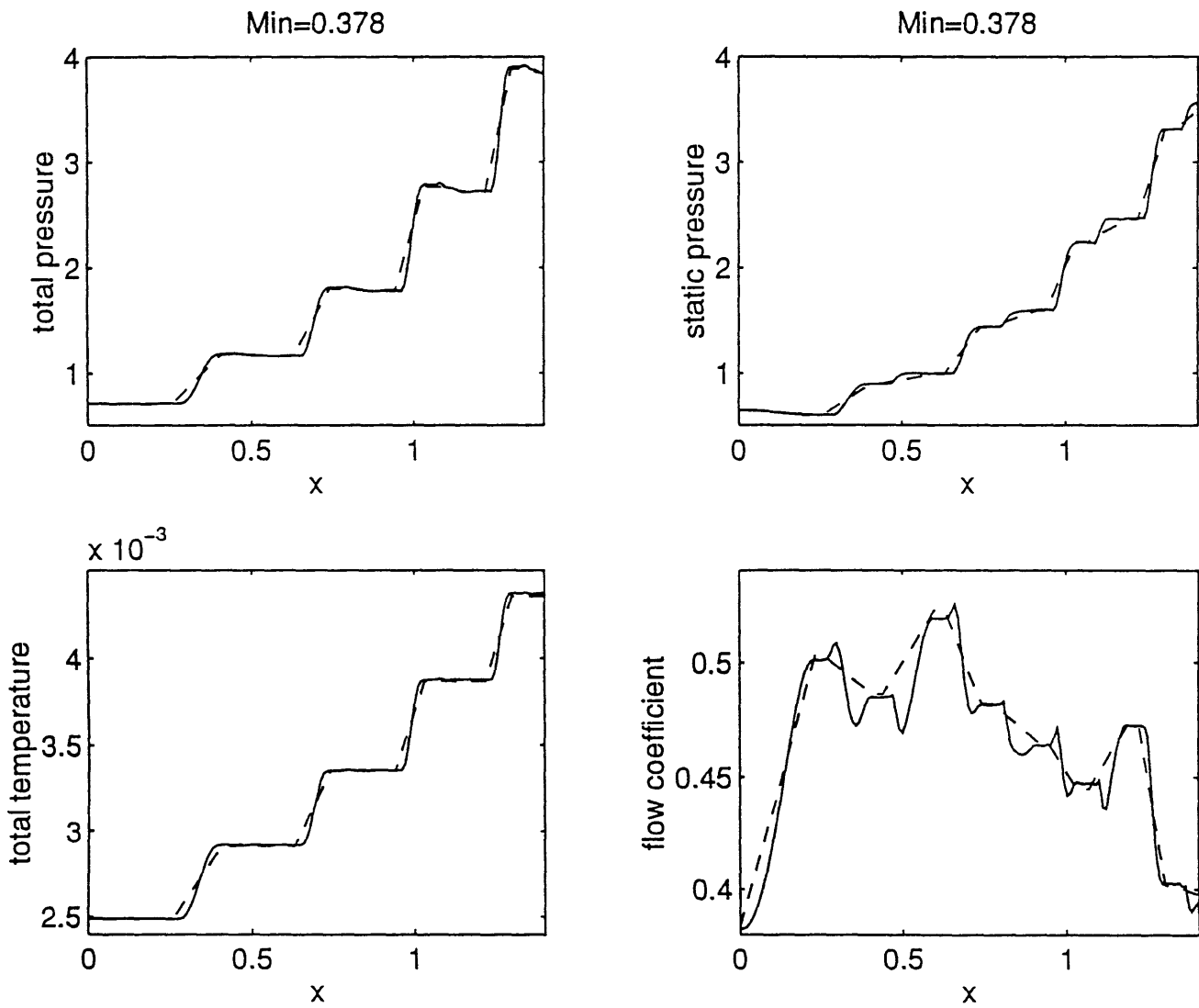
Figure 3.6   Comparison of flow variables calculated from current

model (solid line) and PWmean (dashed line) at an

operating point where the inlet Mach number is 0.378
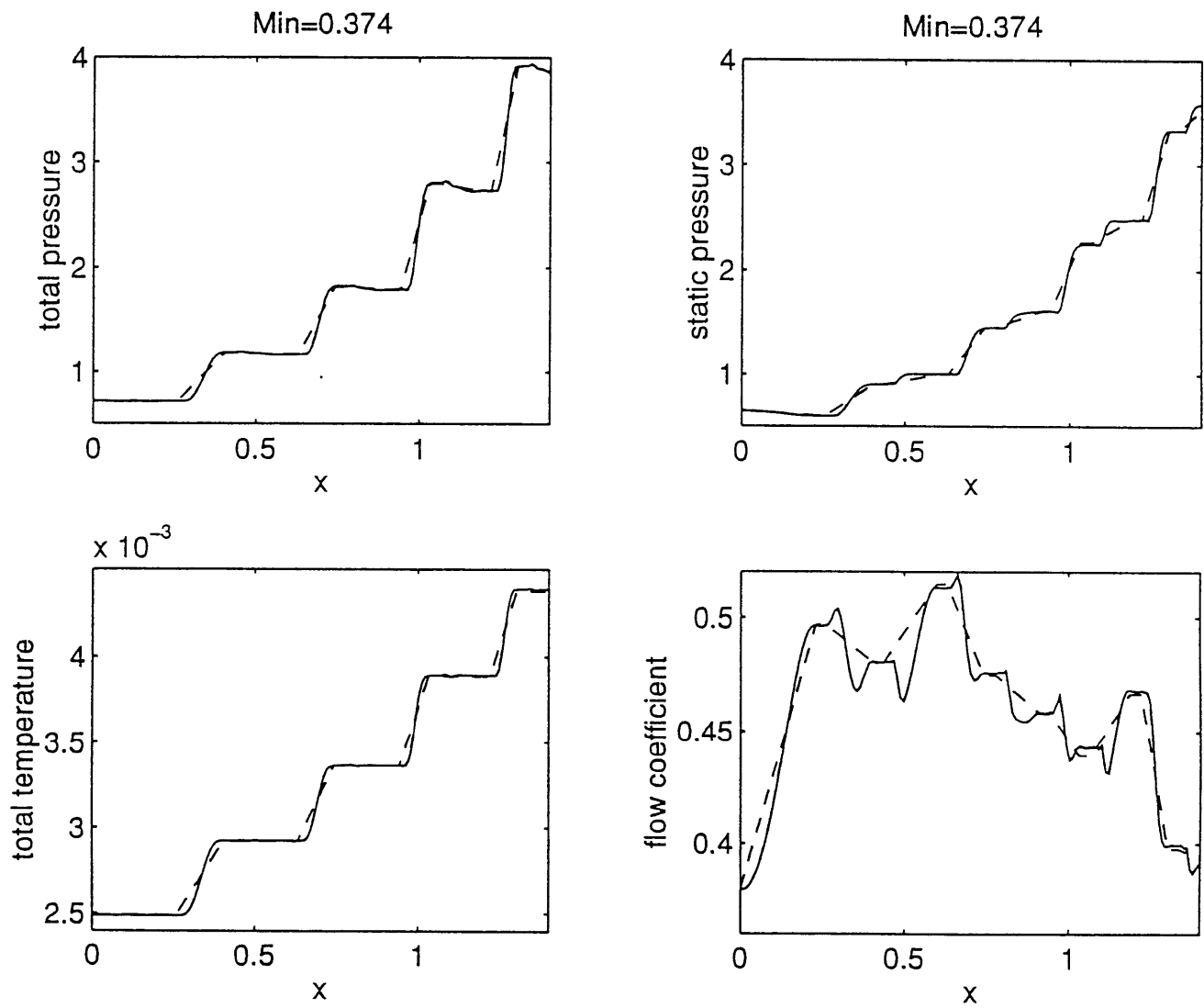
Figure 3.7   Comparison of flow variables calculated from current

model (solid line) and PWmean (dashed line) at an

operating point where the inlet Mach number is 0.374
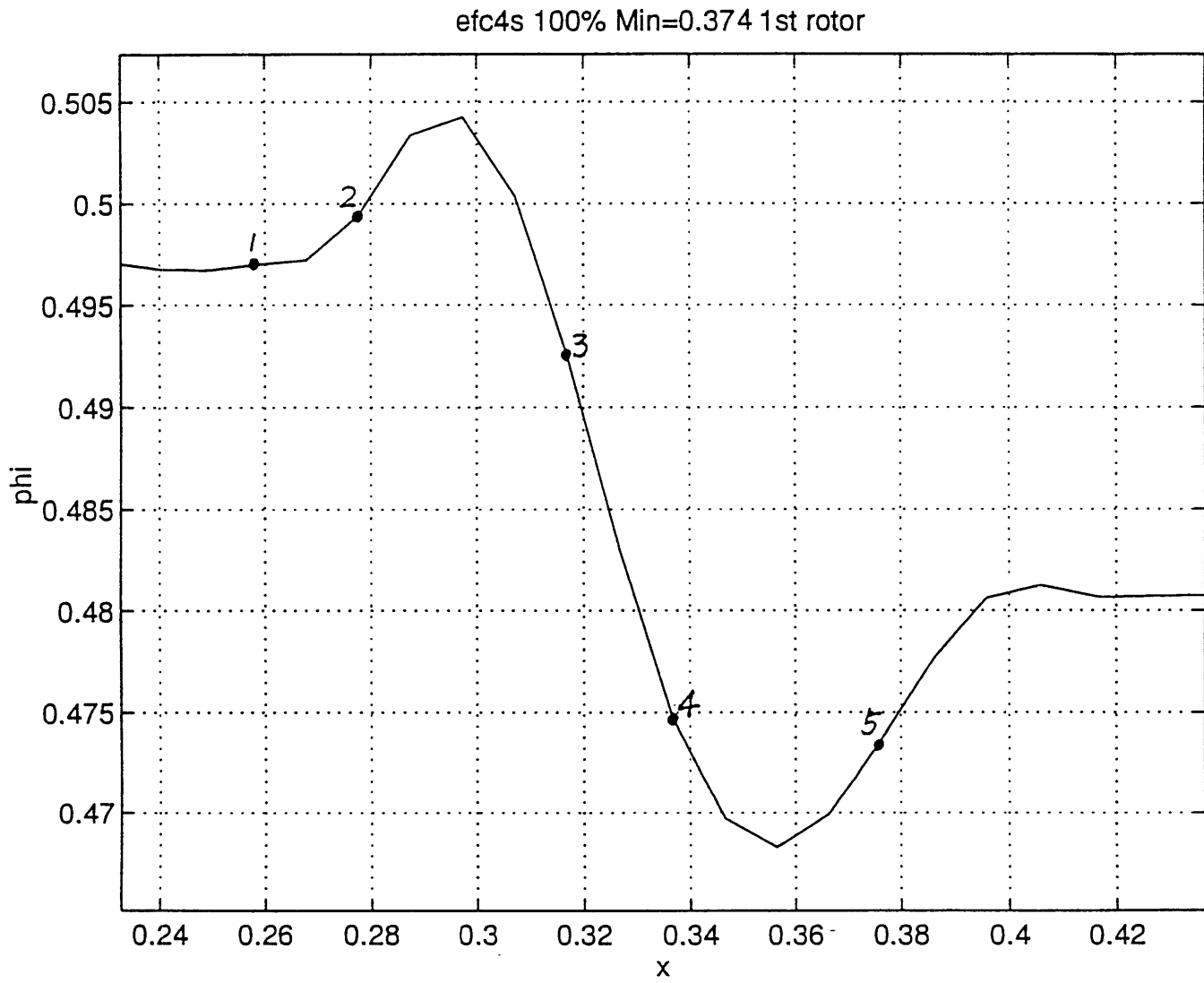
Figure 3.8   Axial distribution of flow coefficient in the first rotor
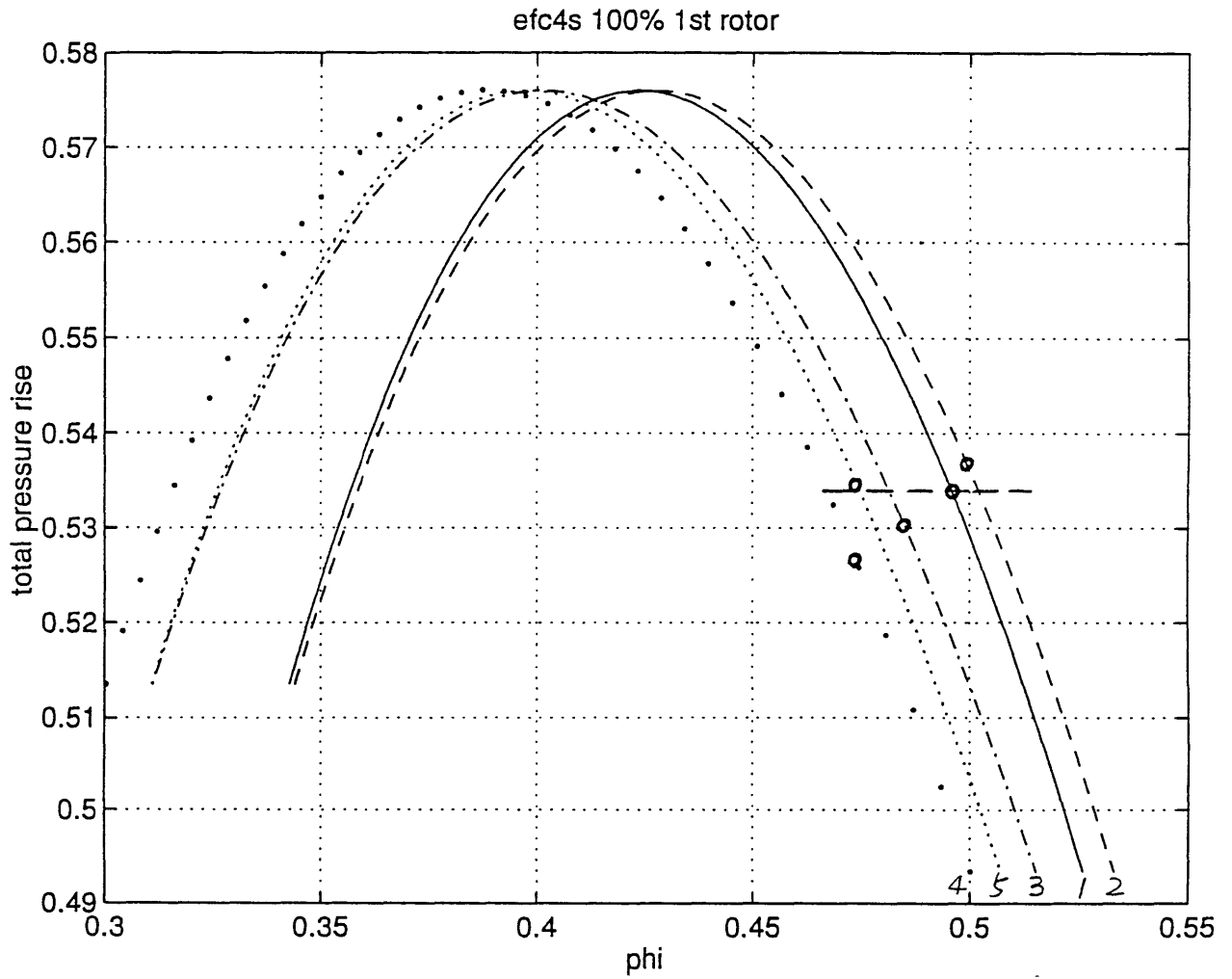
Figure 3.9   Local characteristics of five axial locations
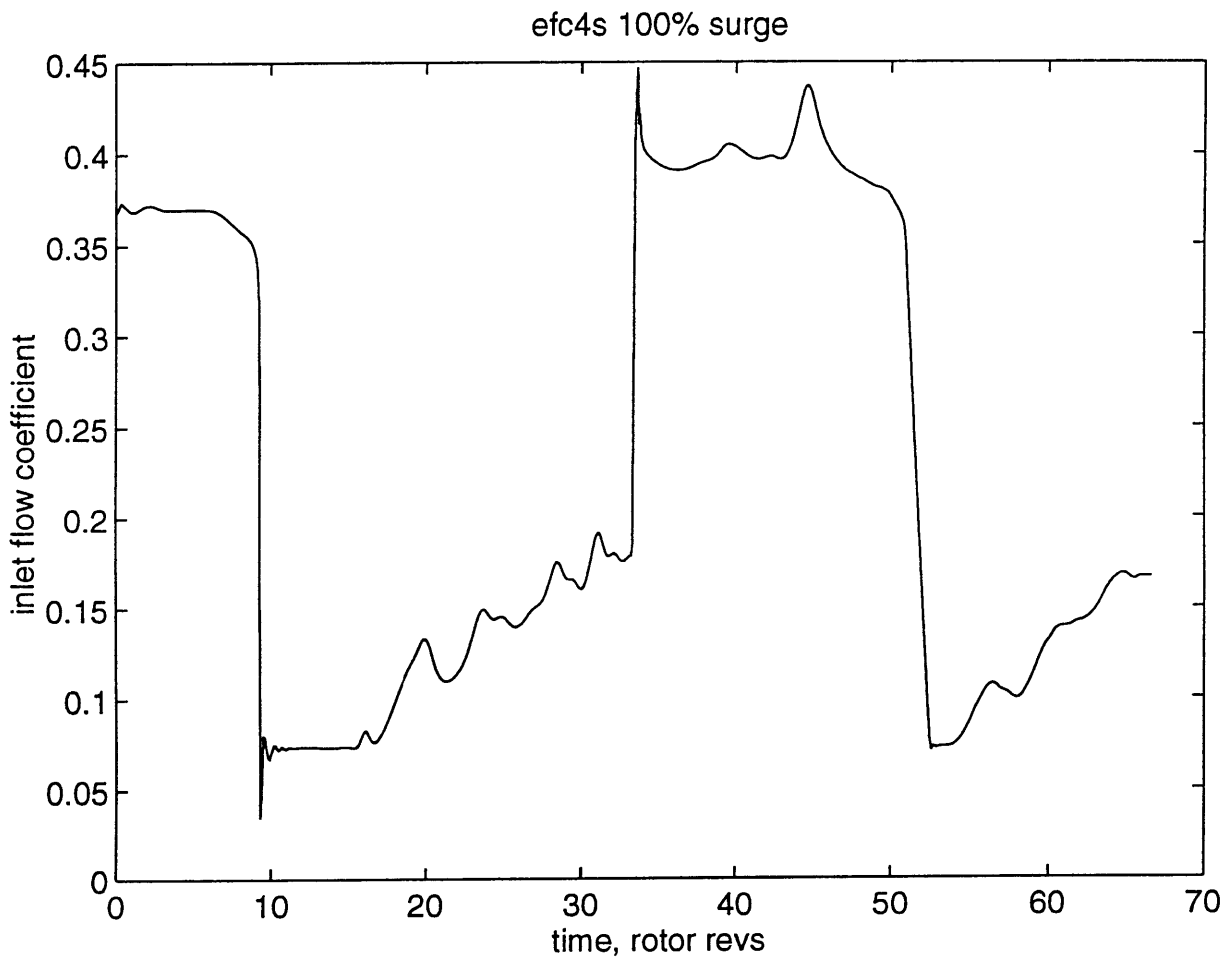
Figure 3.10   Time history of inlet flow coefficient in 4-stage

compressor at 100% corrected speed showing the

surge behavior

Time History of Flow Coefficient at Four Circumferential Positions
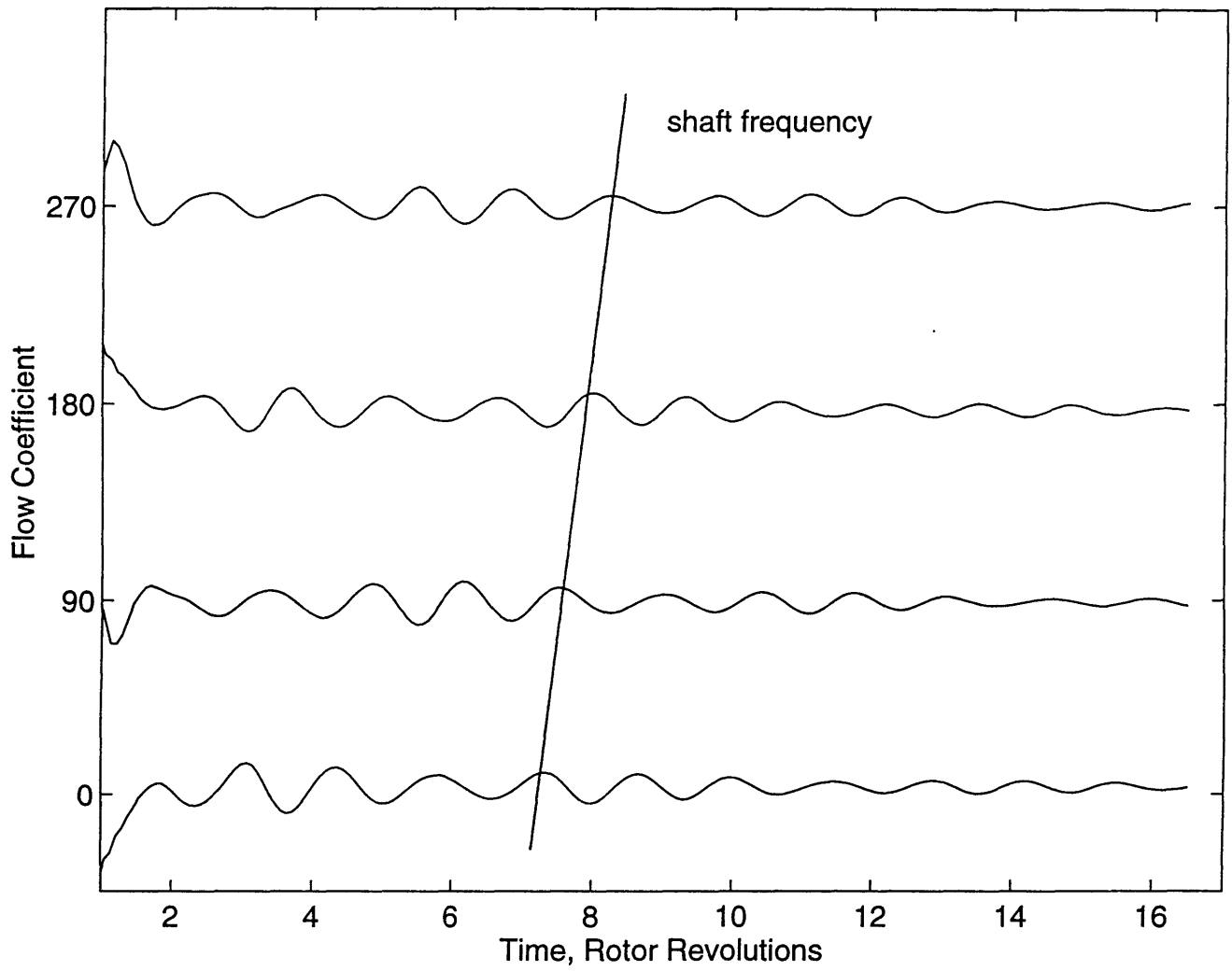
Figure 3.11   Time history of axial velocity at four circumferential

positions in 4-stage compressor at 100% corrected

speed
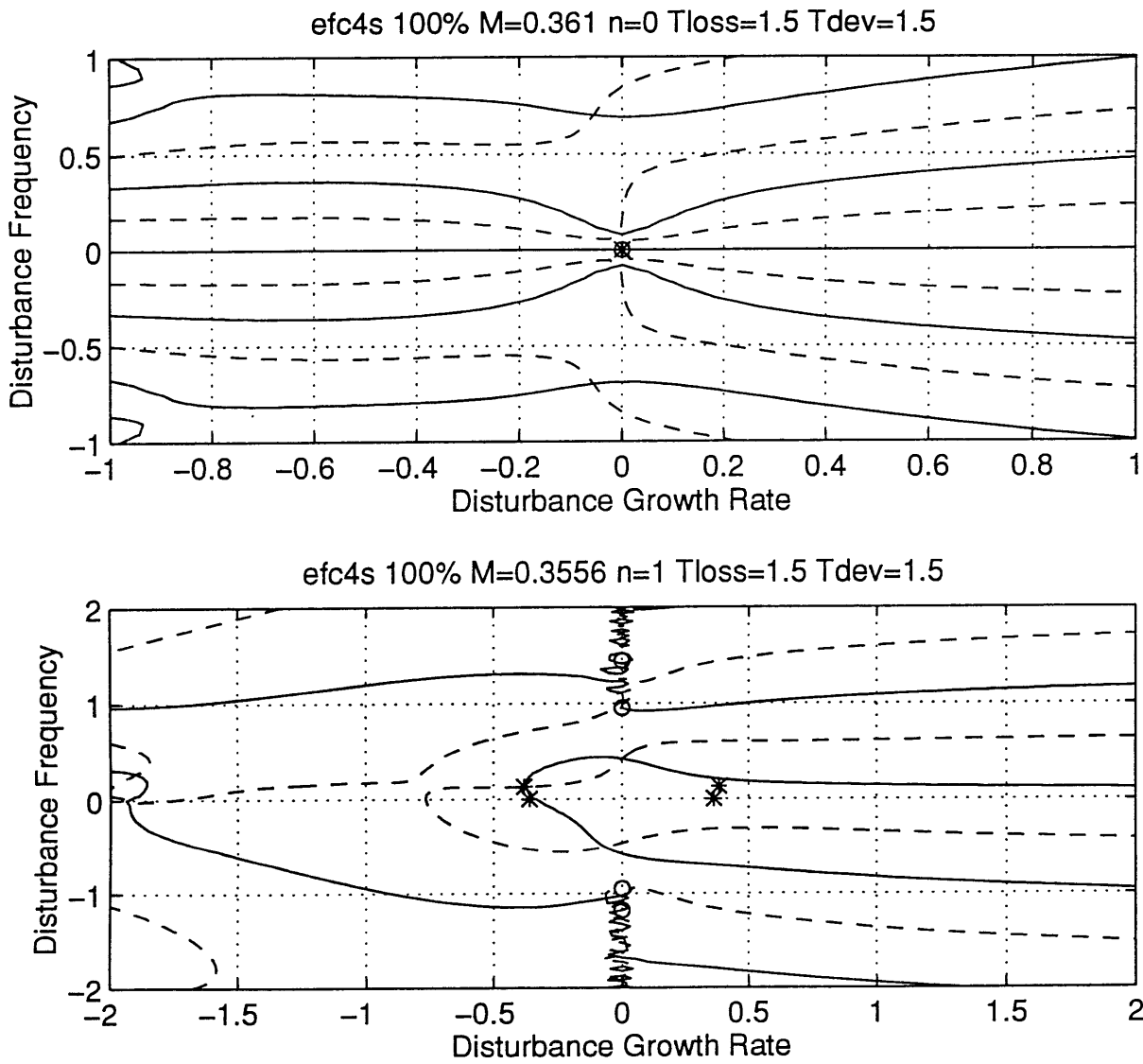
Figure 3.12 Eigenvalues plots for surge type and rotating stall

type of instabilities from linearized analysis

efc4s 100% pert(n=1,a=0.05)
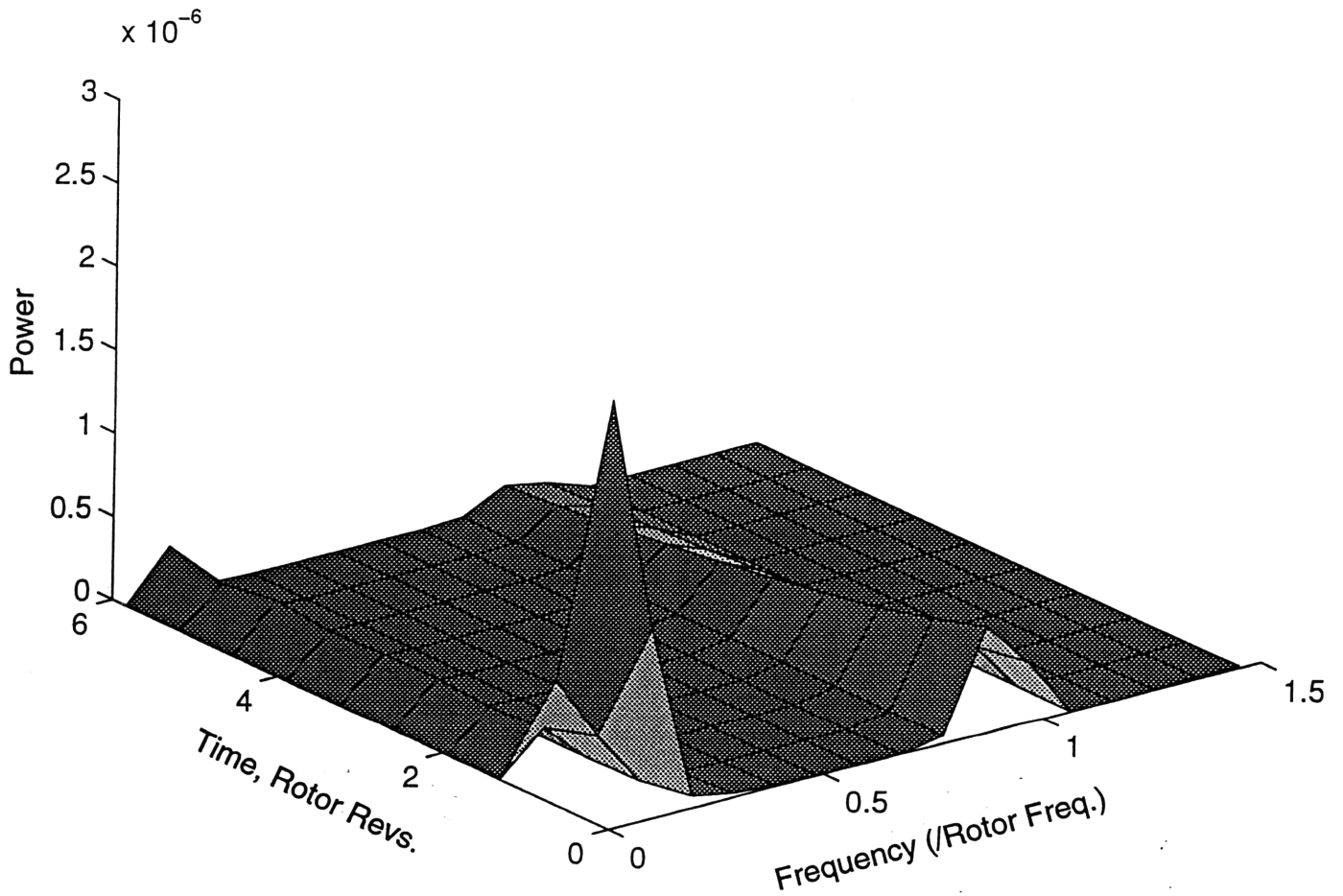
Figure 3.13   Three-dimensional power spectrum density plot

showing time history of the frequency components in
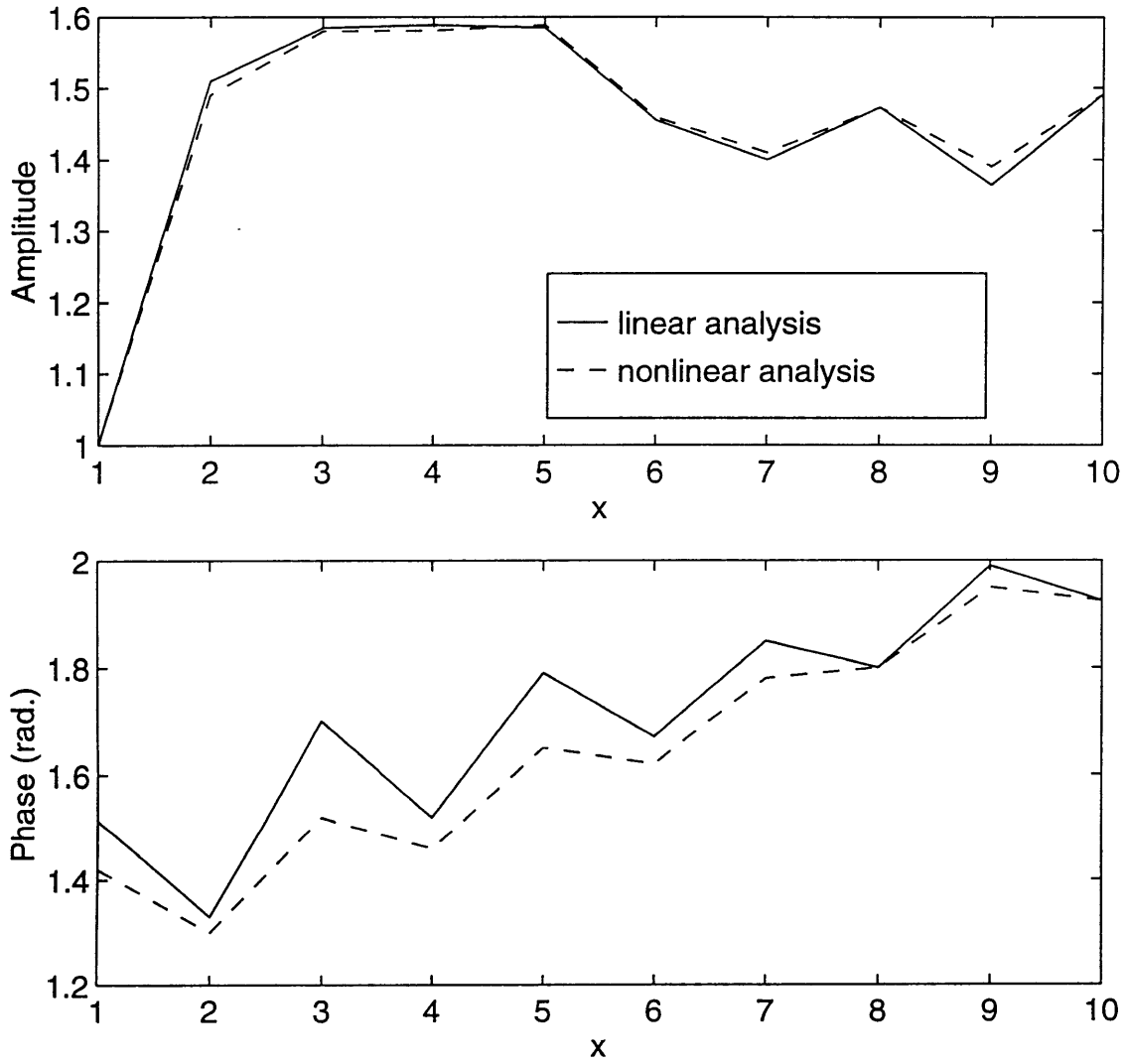
the first spatial harmonics of flow coefficient
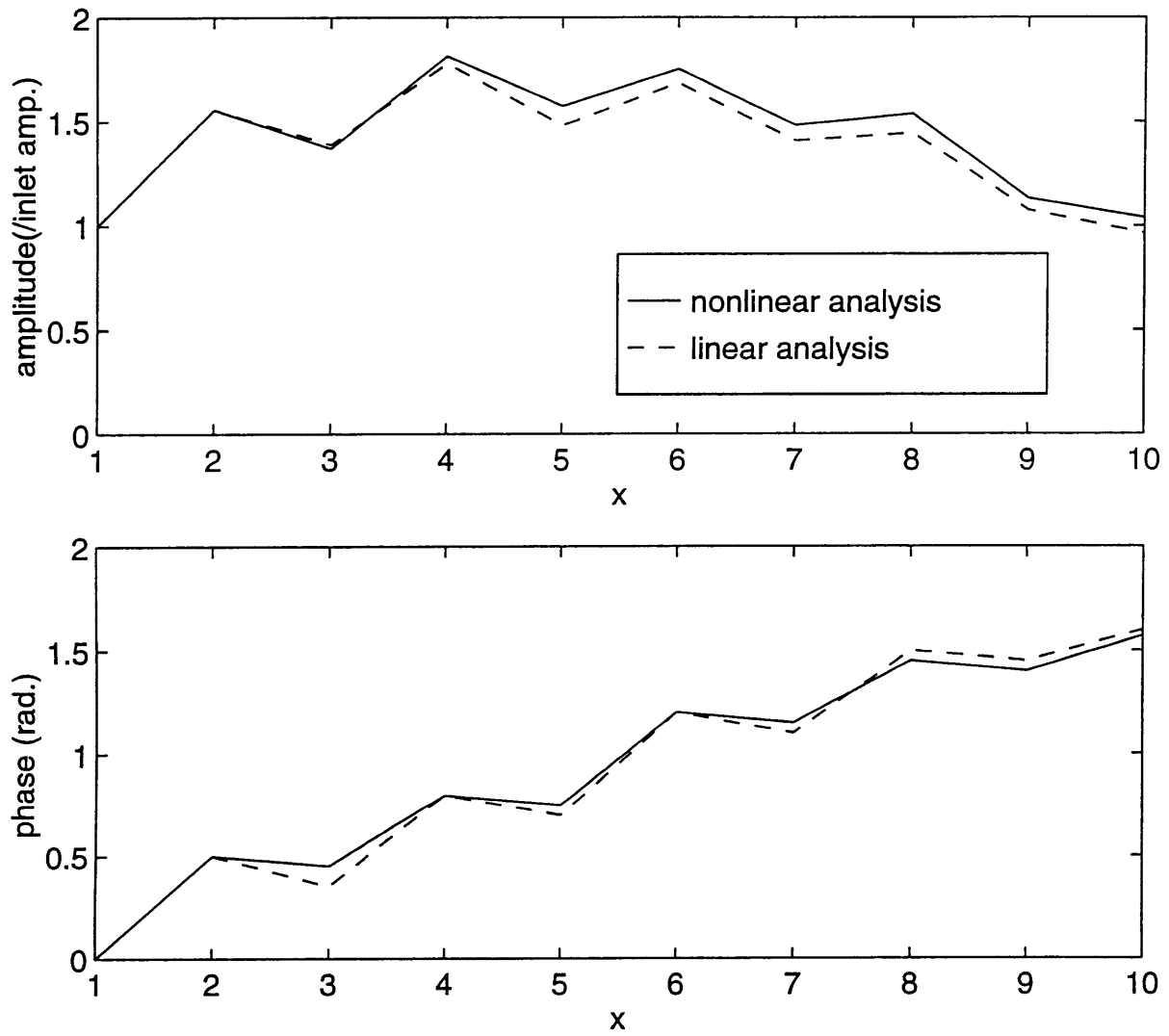
Figure 3.14   Axial structure of flow coefficient perturbation for the

compressible mode; nonlinear and linear analysis
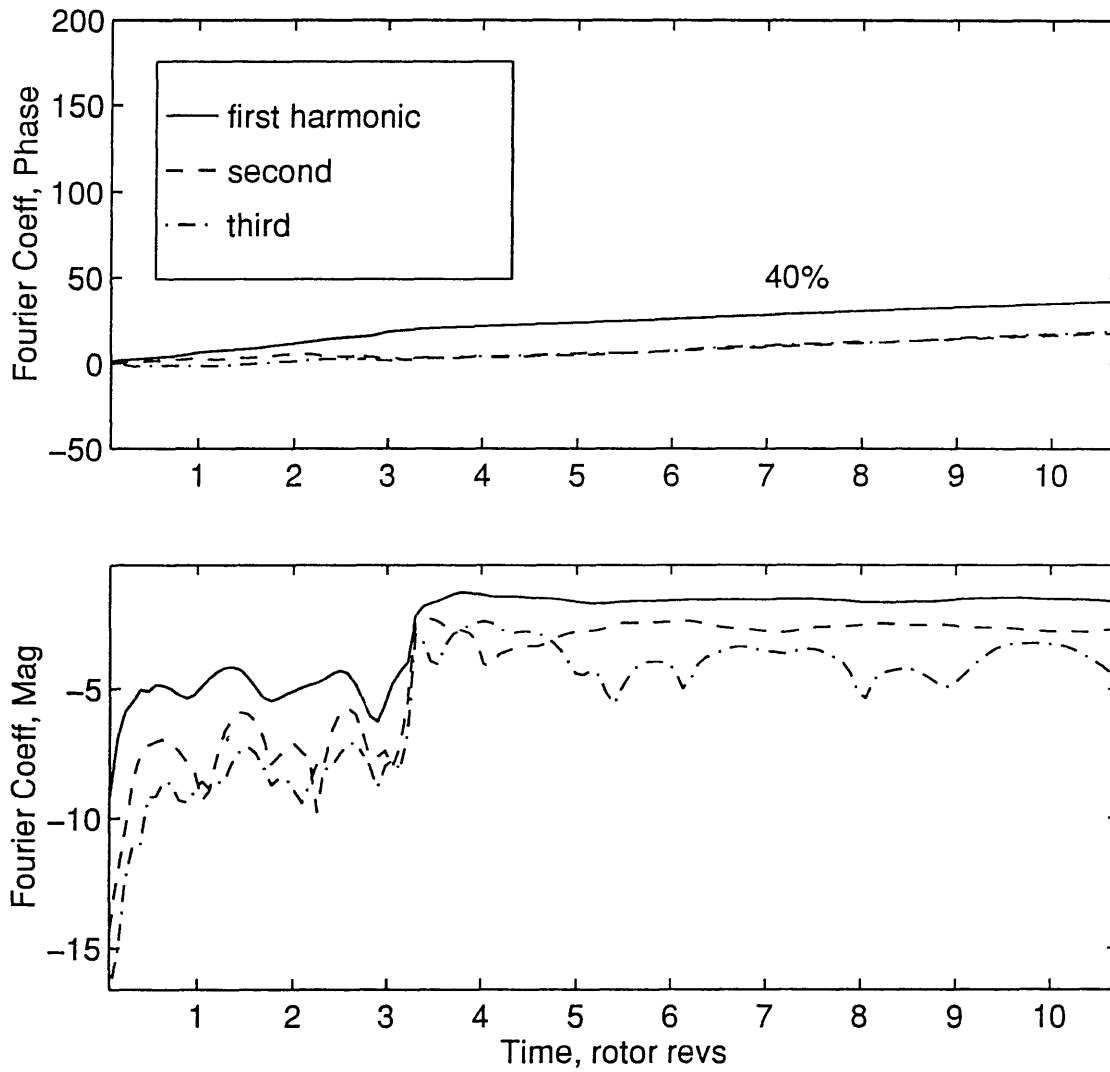
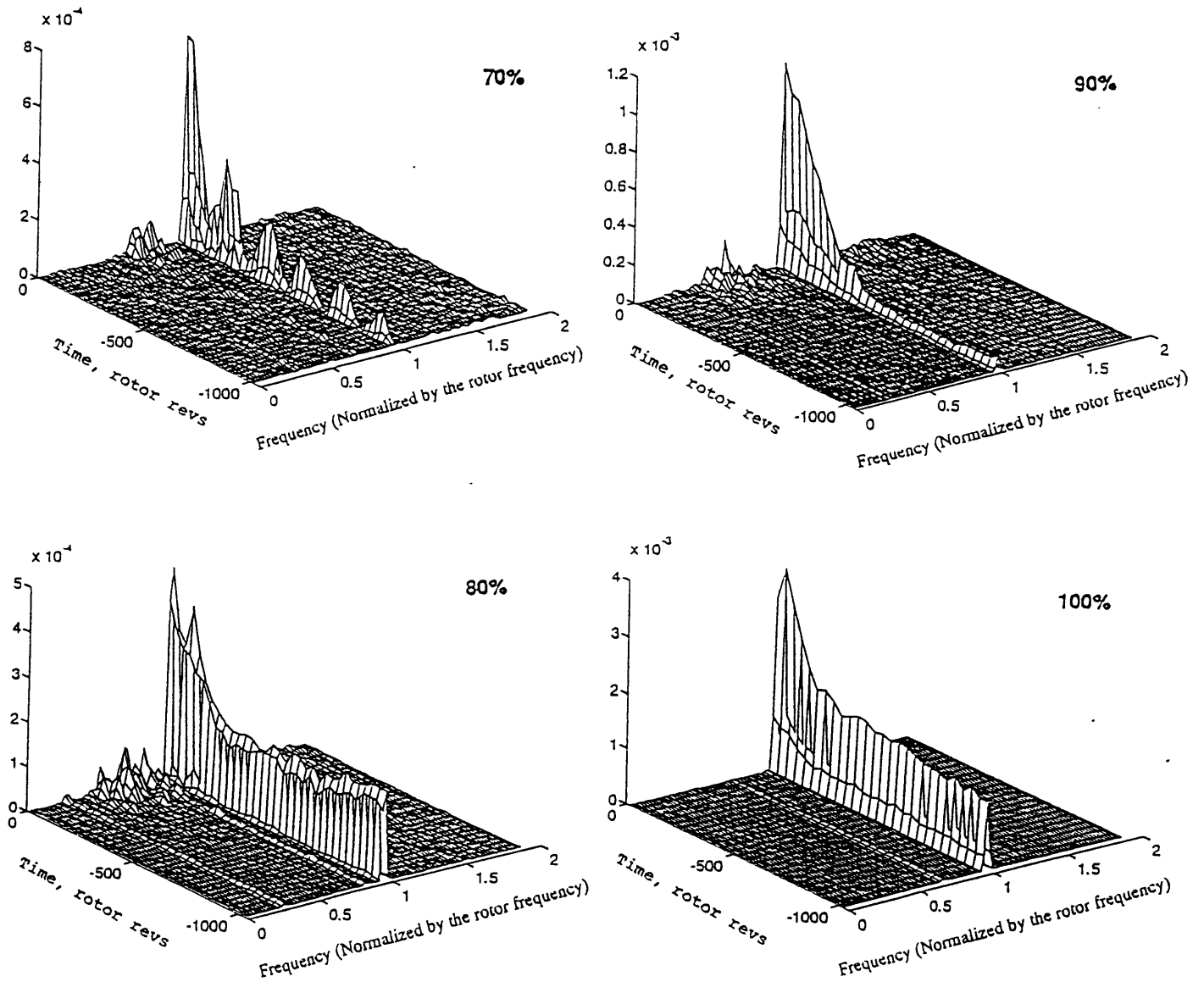Figure 3.15   Time history of the first three spatial harmonics of

flow coefficient with once per revolution forcing
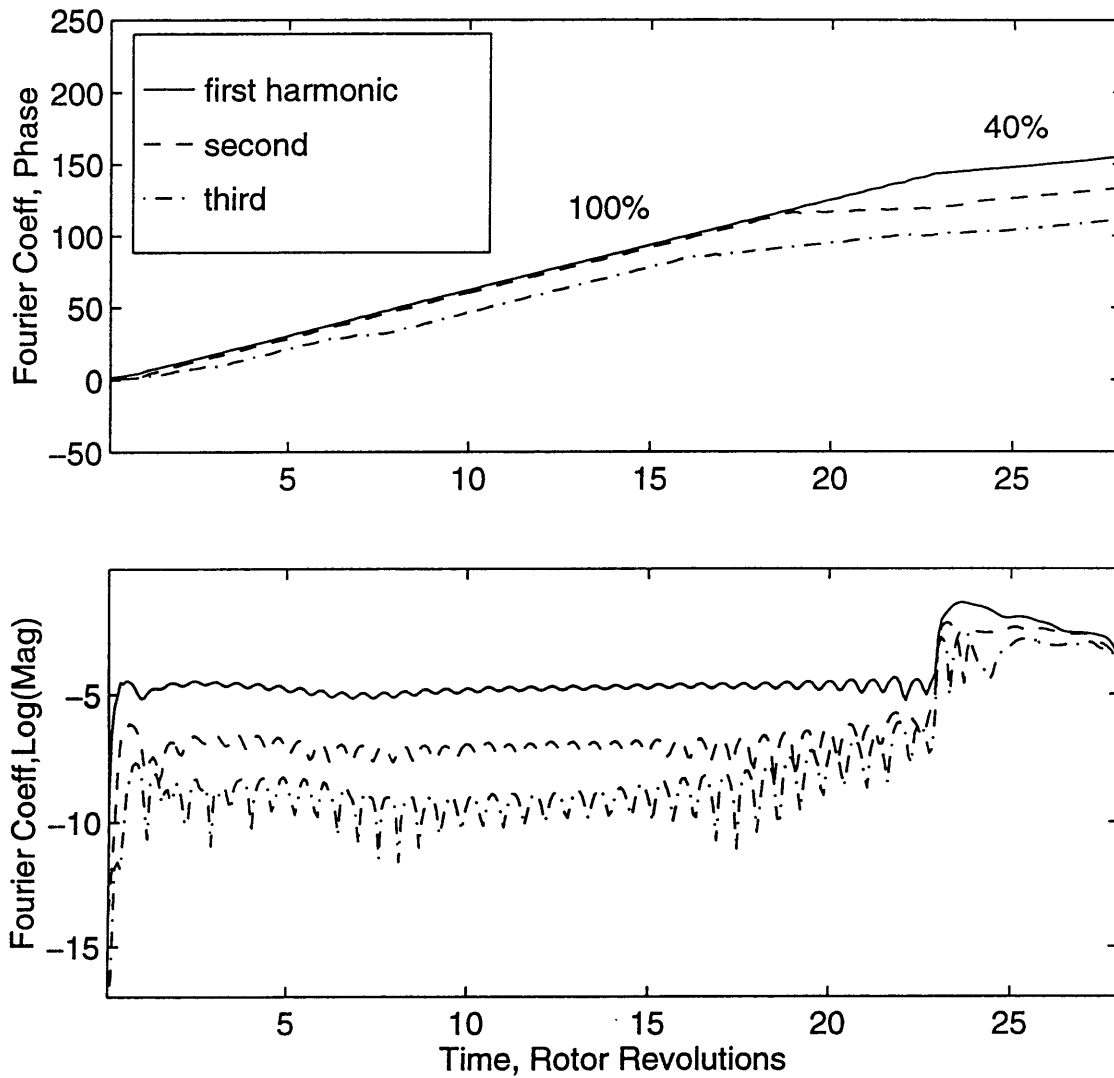
Figure 3.16   Time history of the first three spatial harmonics of flow

coefficient with once per revolution forcing as the

throttle slowly closed from a stable condition

efc4s 100%
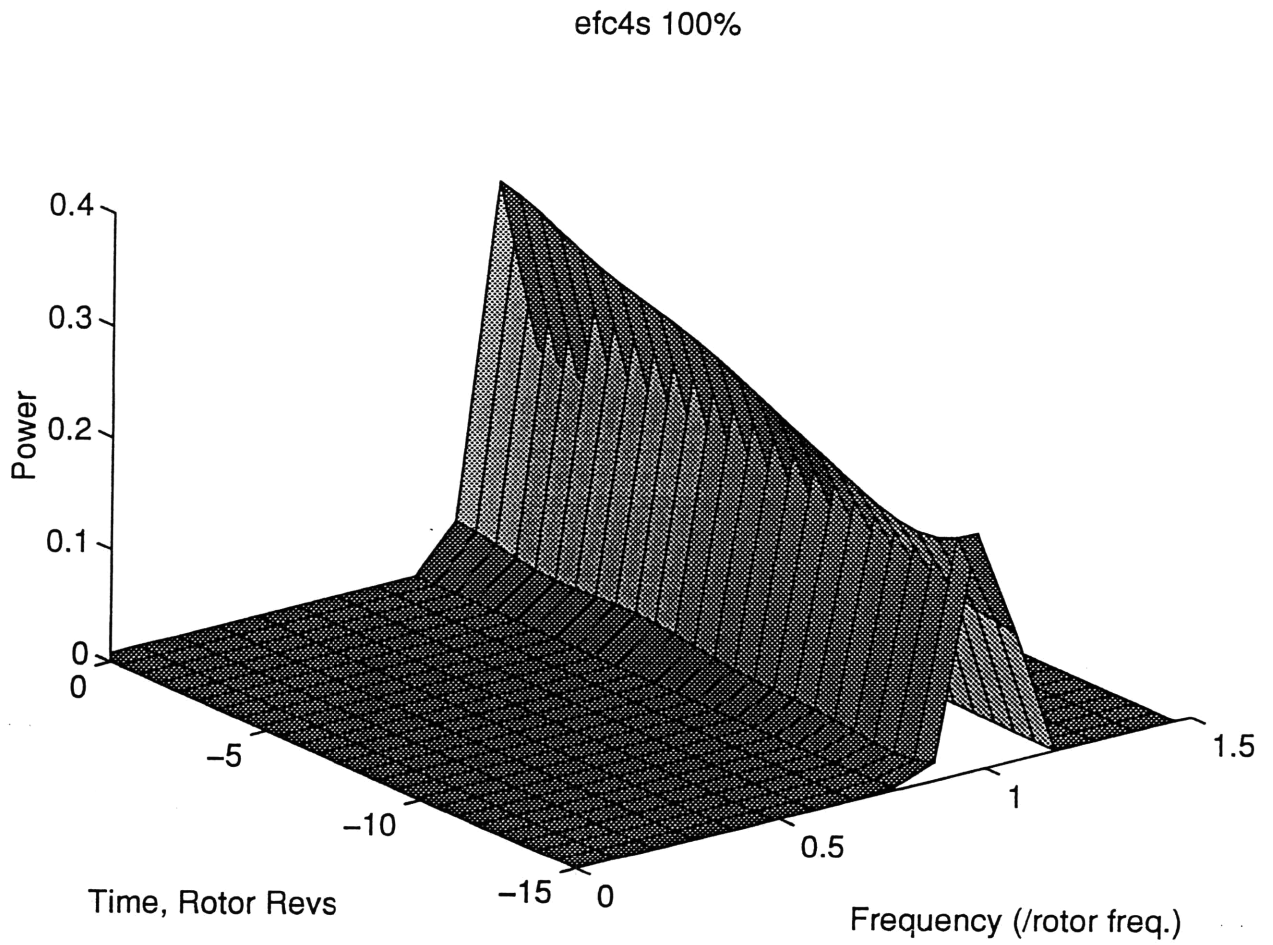
Figure 3.17   Time history of the prestall once per revolution wave

energy in the first harmonic of flow coefficient (from

calculation)
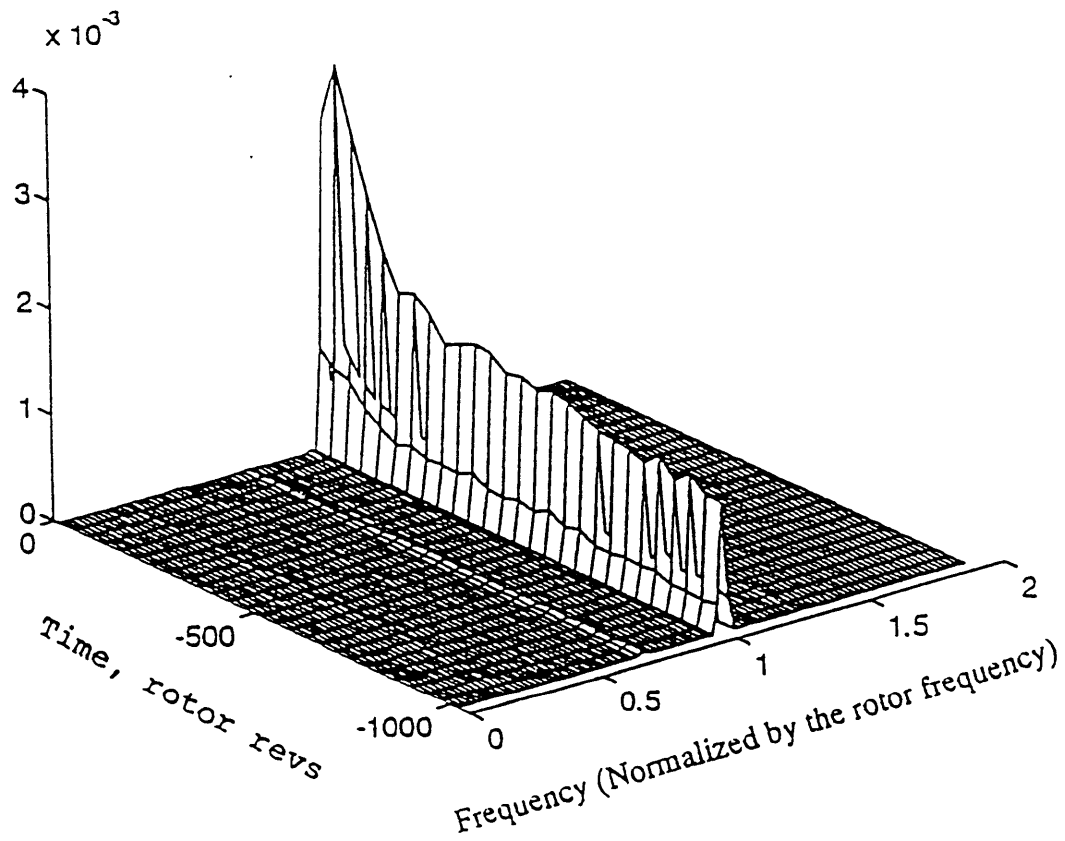
Figure 3.18   Time history of the prestall once per revolution wave

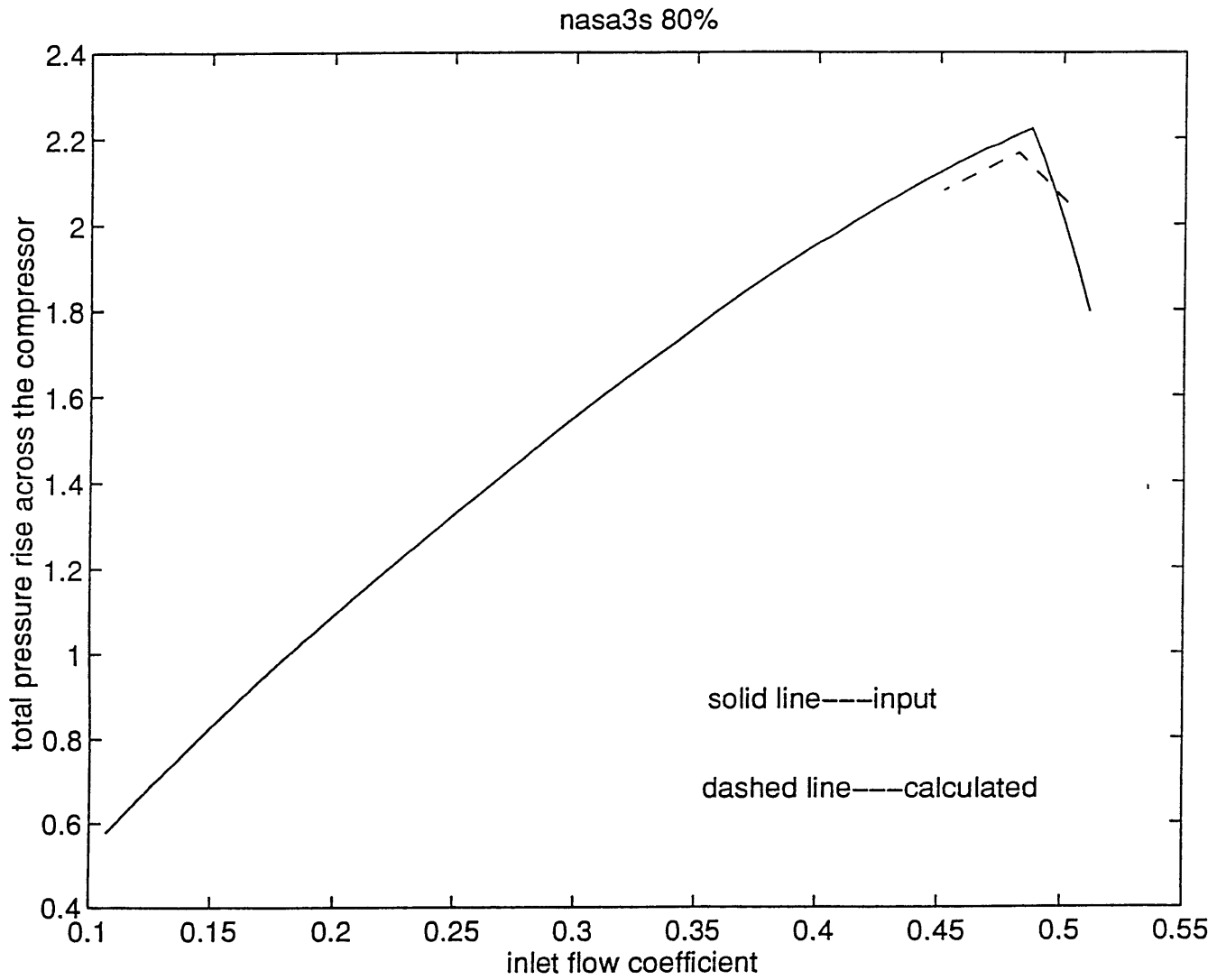energy in the first harmonic of flow coefficient (from

data)
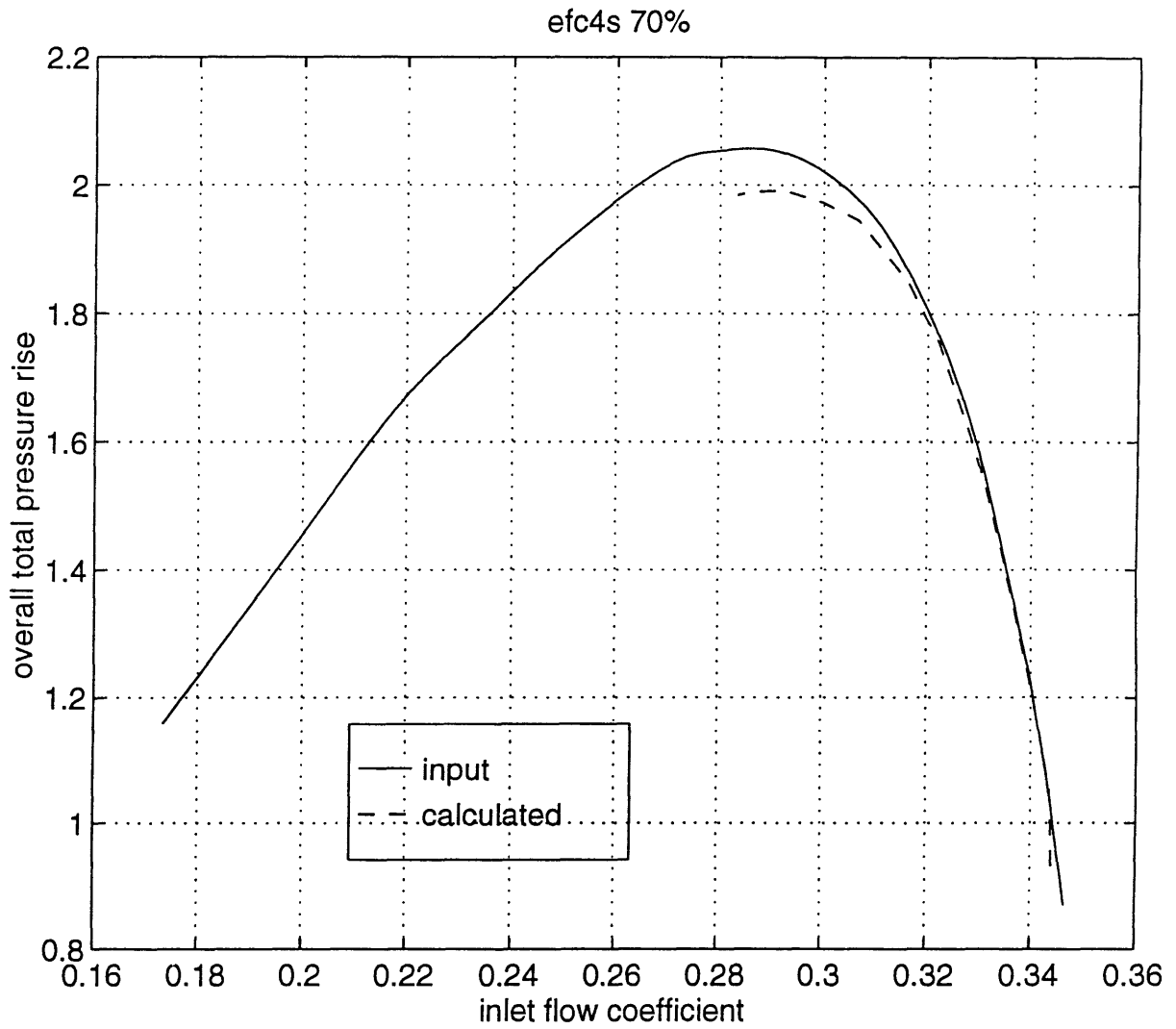
Figure 3.19   Comparison of input and calculated overall compressor

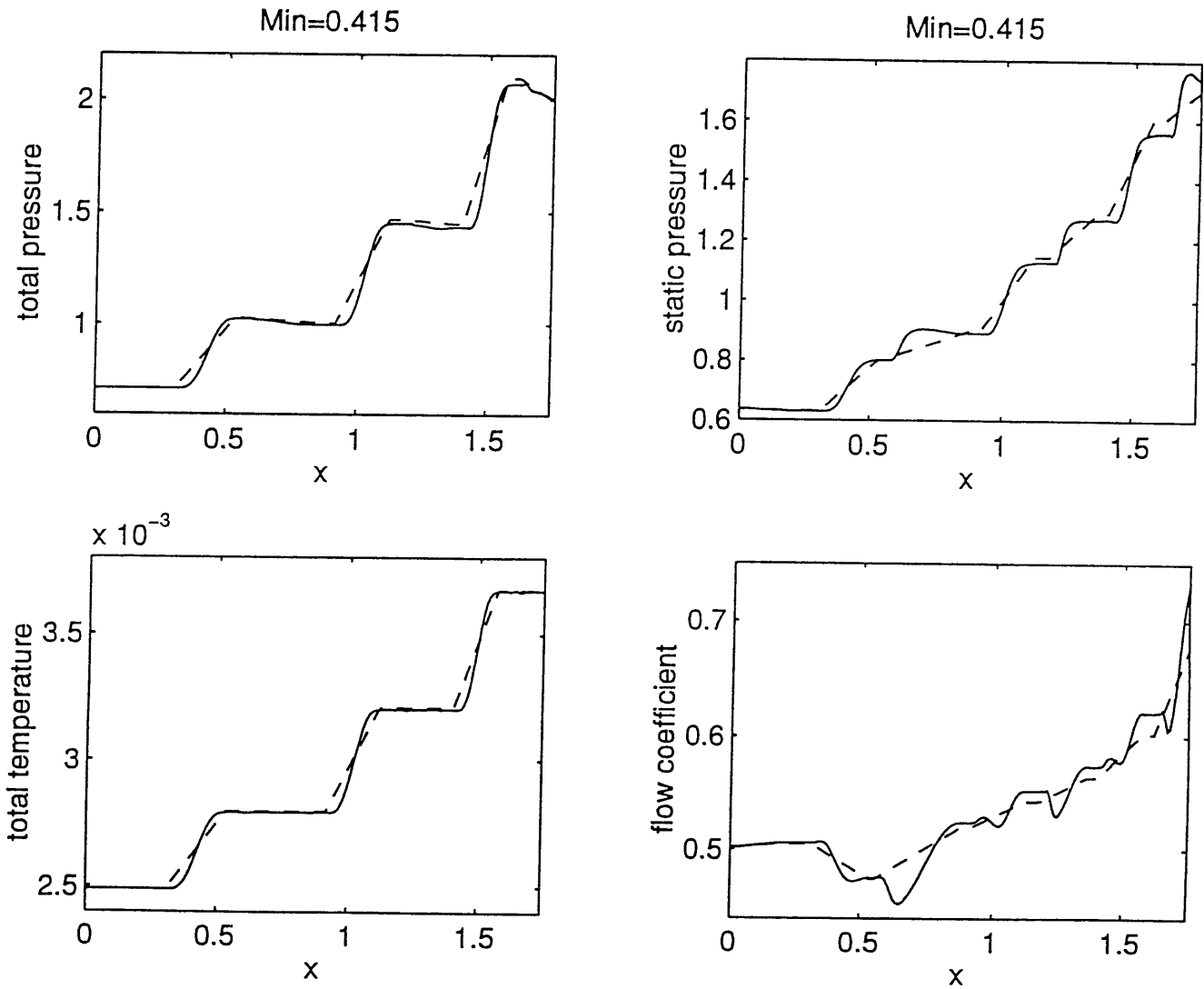characteristics of 4-stage compressor at 70% corrected

speed

Figure 3.20   Comparison of flow variables calculated from current

model (solid line) and PWmean (dashed line) at an

operating point where the inlet Mach number is 0.196

93
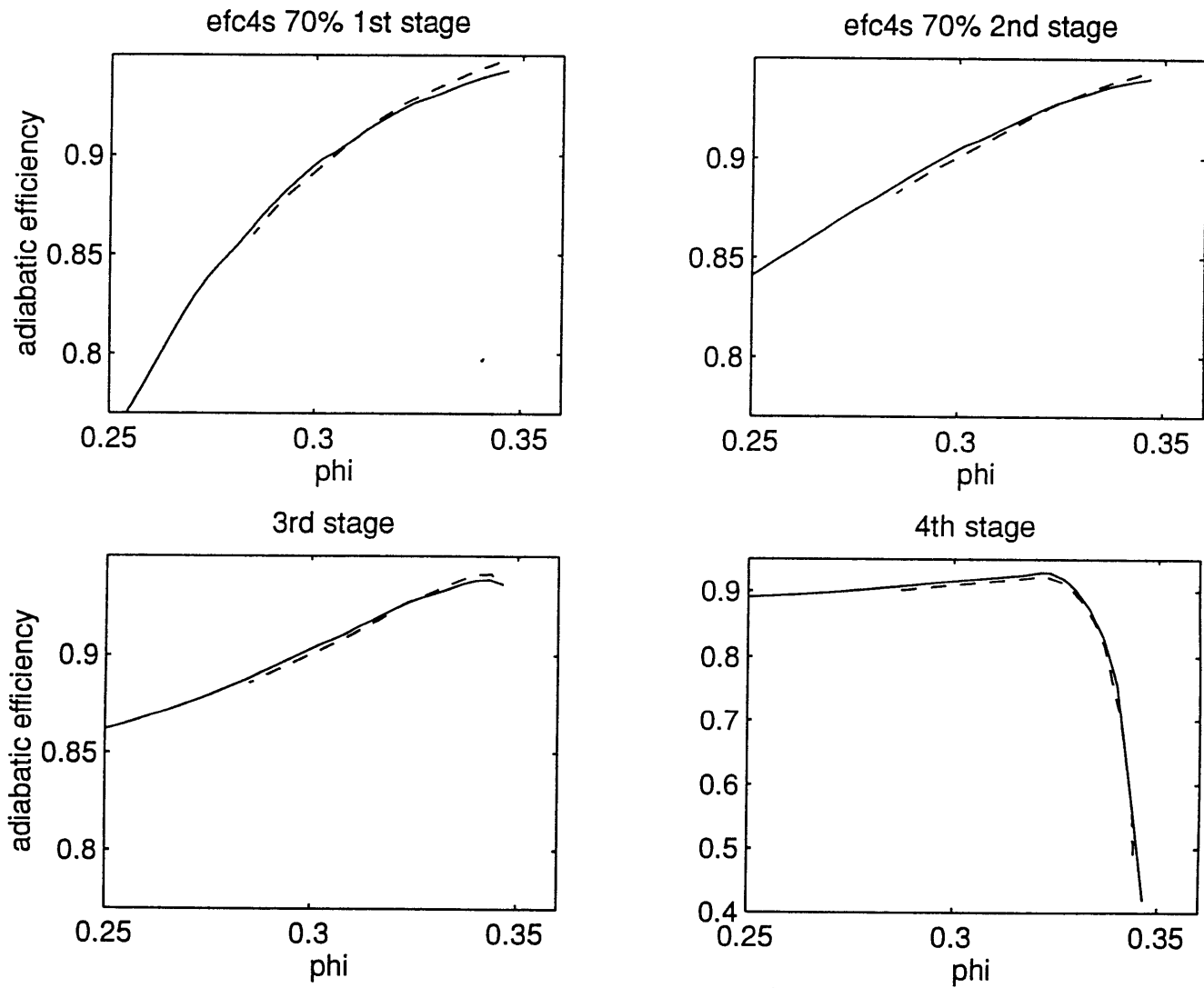
Figure 3.21   Comparison of efficiencies of each stage calculated
from the current model and PWmean for 4-stage
compressor at 70% corrected speed

time history of flow coefficient at four circumferential positions
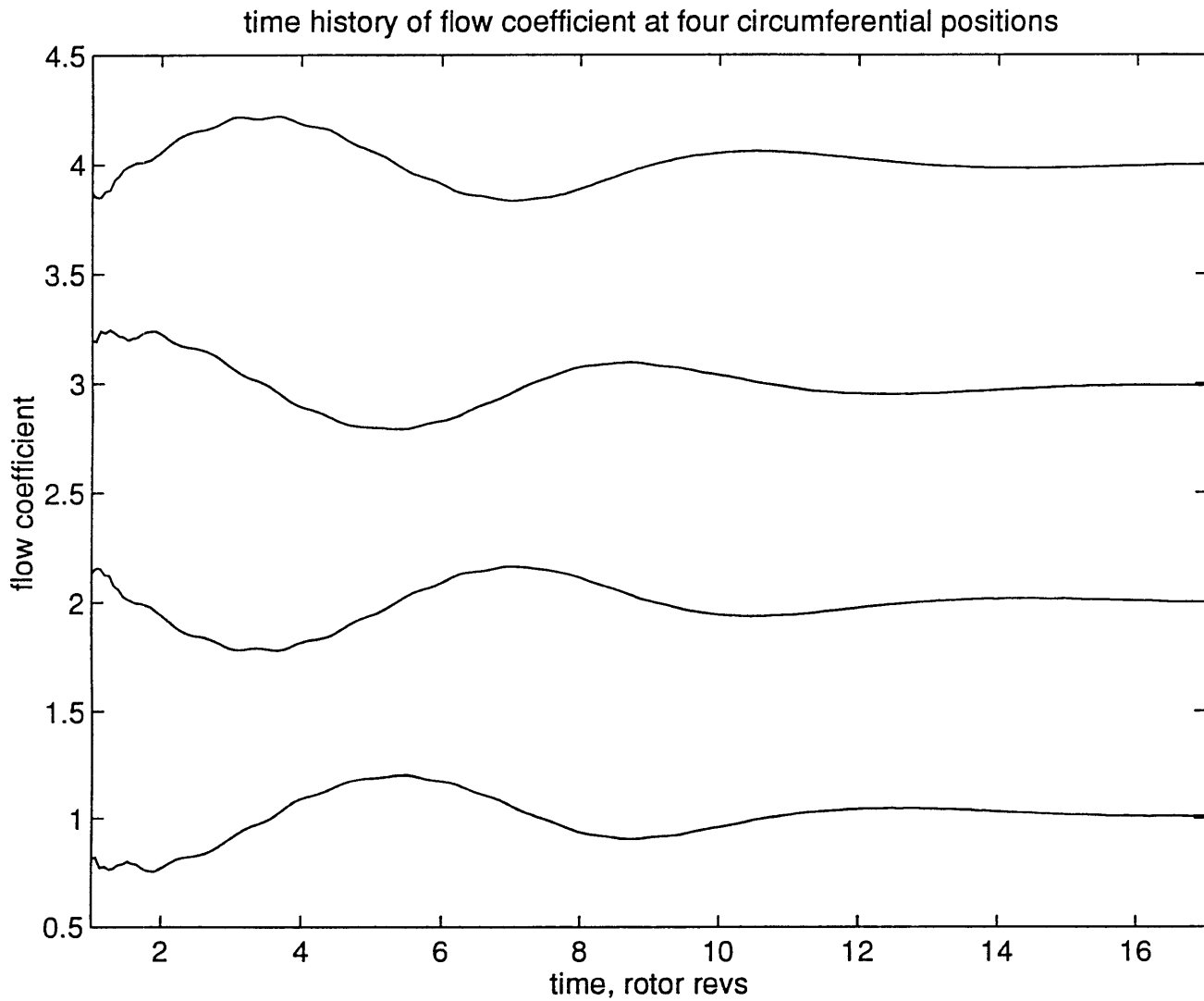
Figure3.22   Time history of inlet flow coefficient in 4-stage

compressor at 70% corrected speed

efc4s 70% M=0.1883 n=0 Tloss=1.5 Tdev=1.5

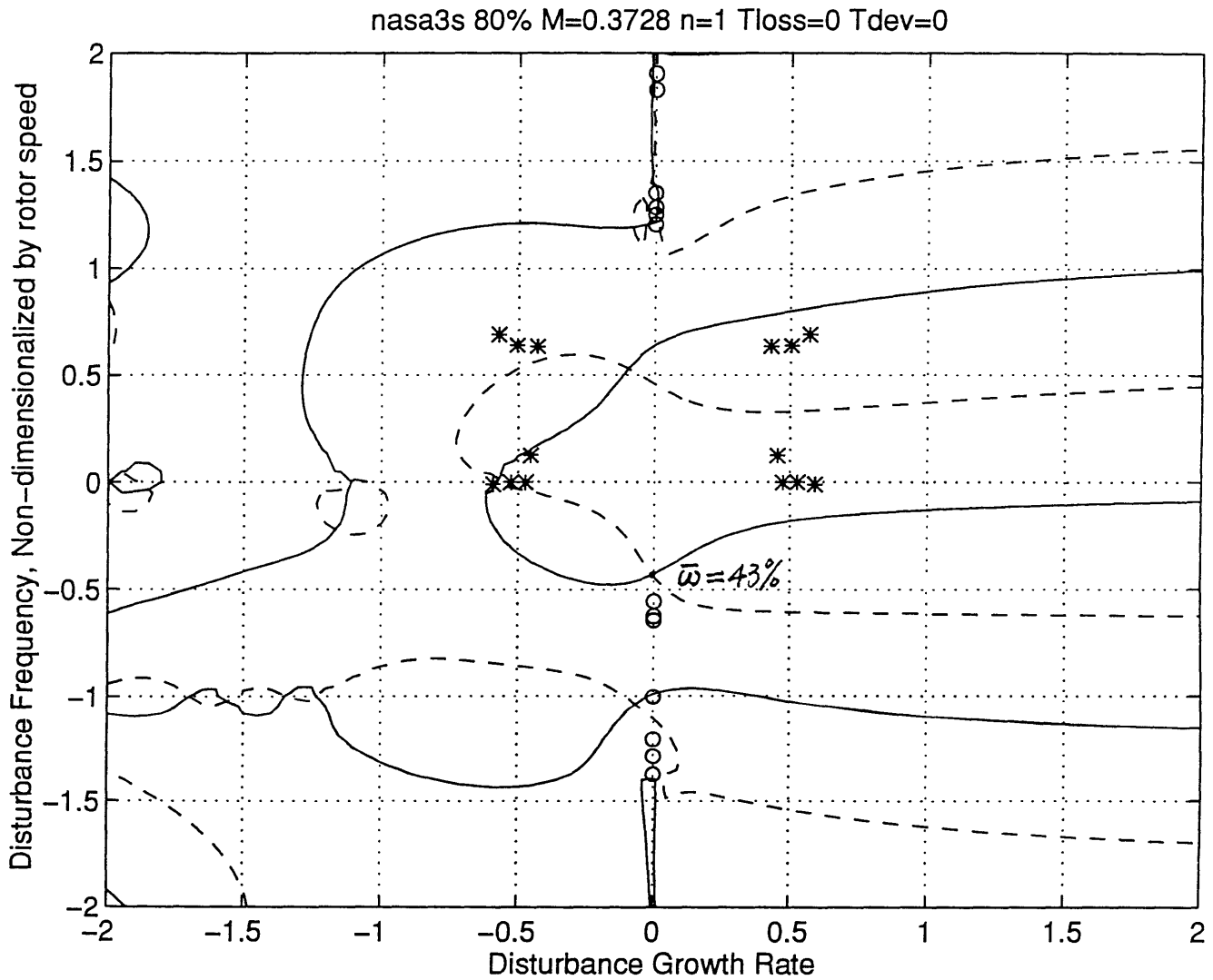efc4s 70% M=0.1862 n=1 Tloss=1.5 Tdev=1.5
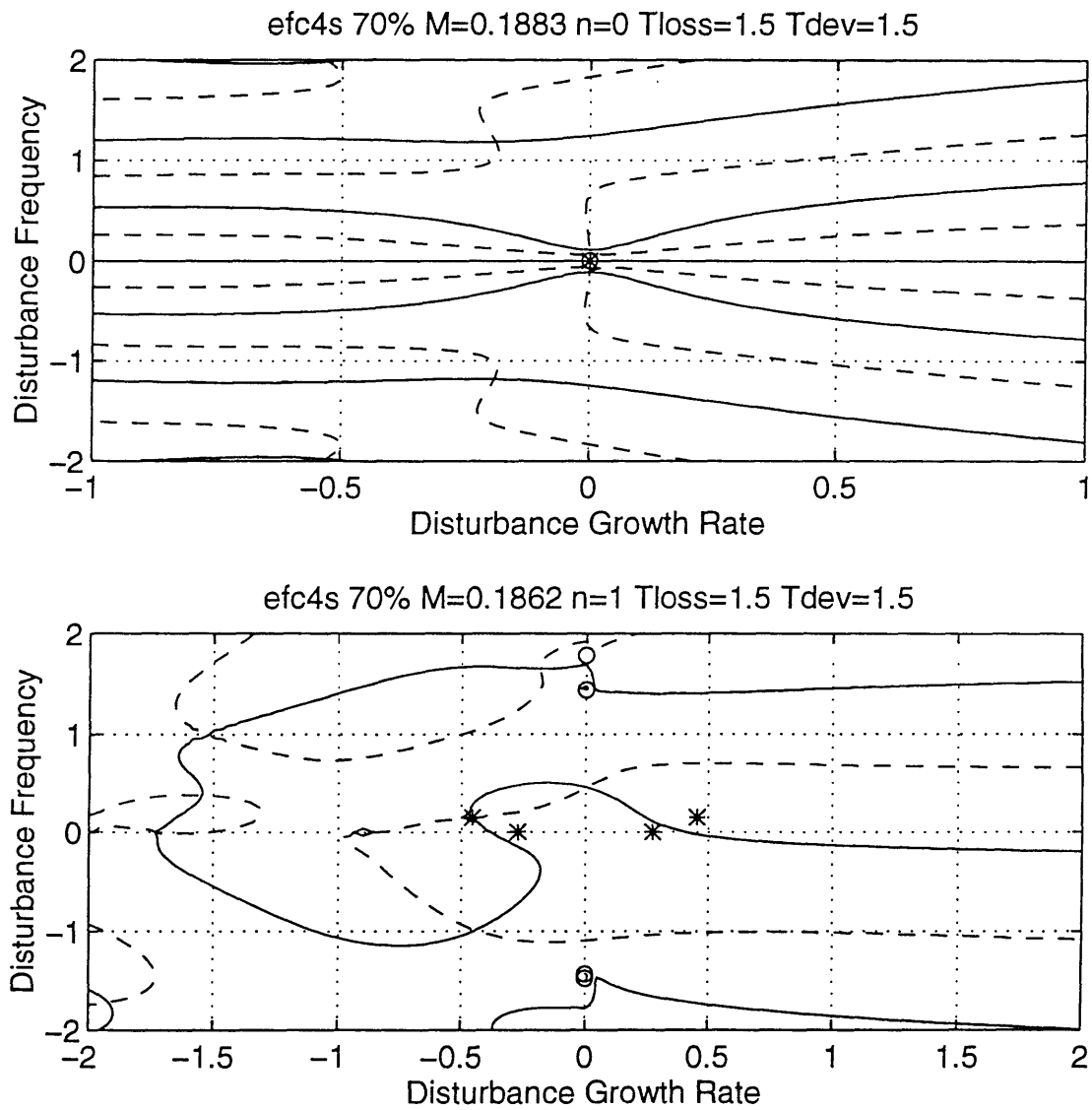
Figure 3.23   Eigenvalues plots for surge type and rotating stall

type of instabilities from linearized analysis for 4-
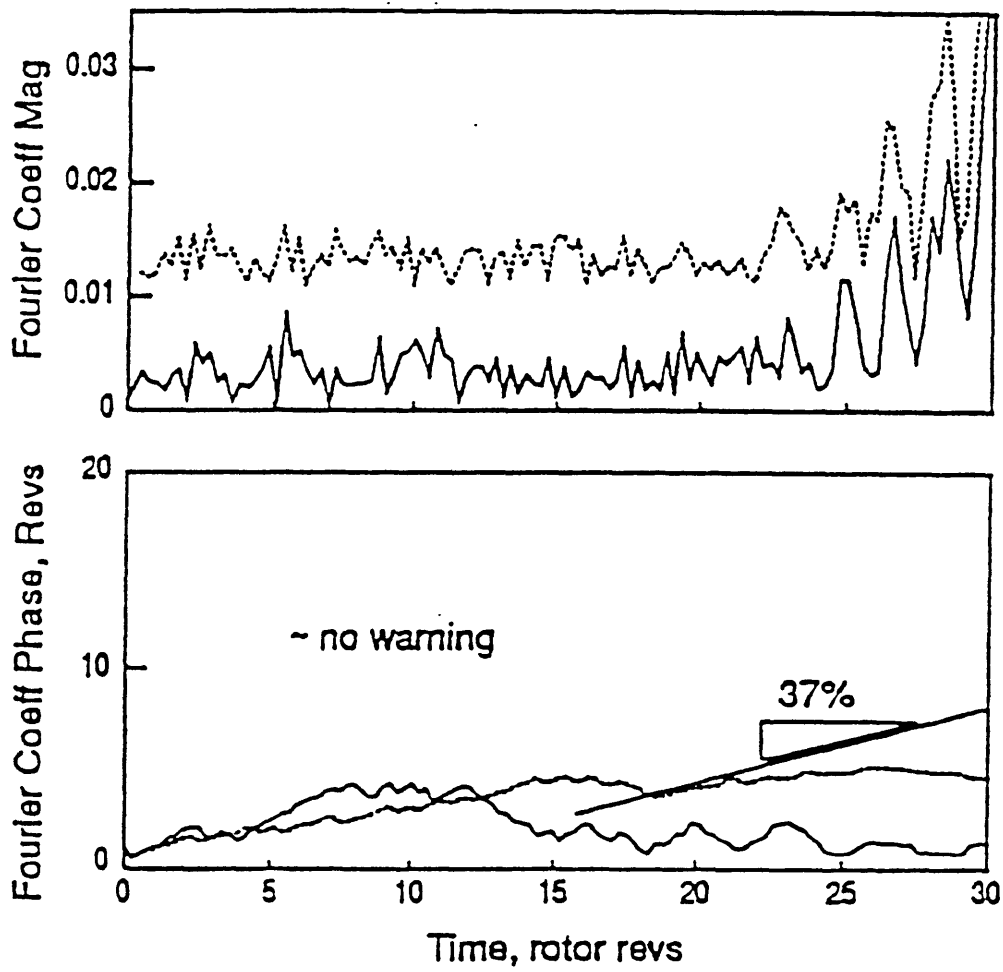
stage compressor at 70% corrected speed

Figure 3.24   Axial structure of flow coefficient perturbation for the
incompressible mode; nonlinear and linear analysis

Figure 3.25 Three-dimensional power spectrum plots of the first

harmonic of flow coefficient of 4-stage compressor at 70%,

80%, 90%, 100% corrected speeds (reduced from data)
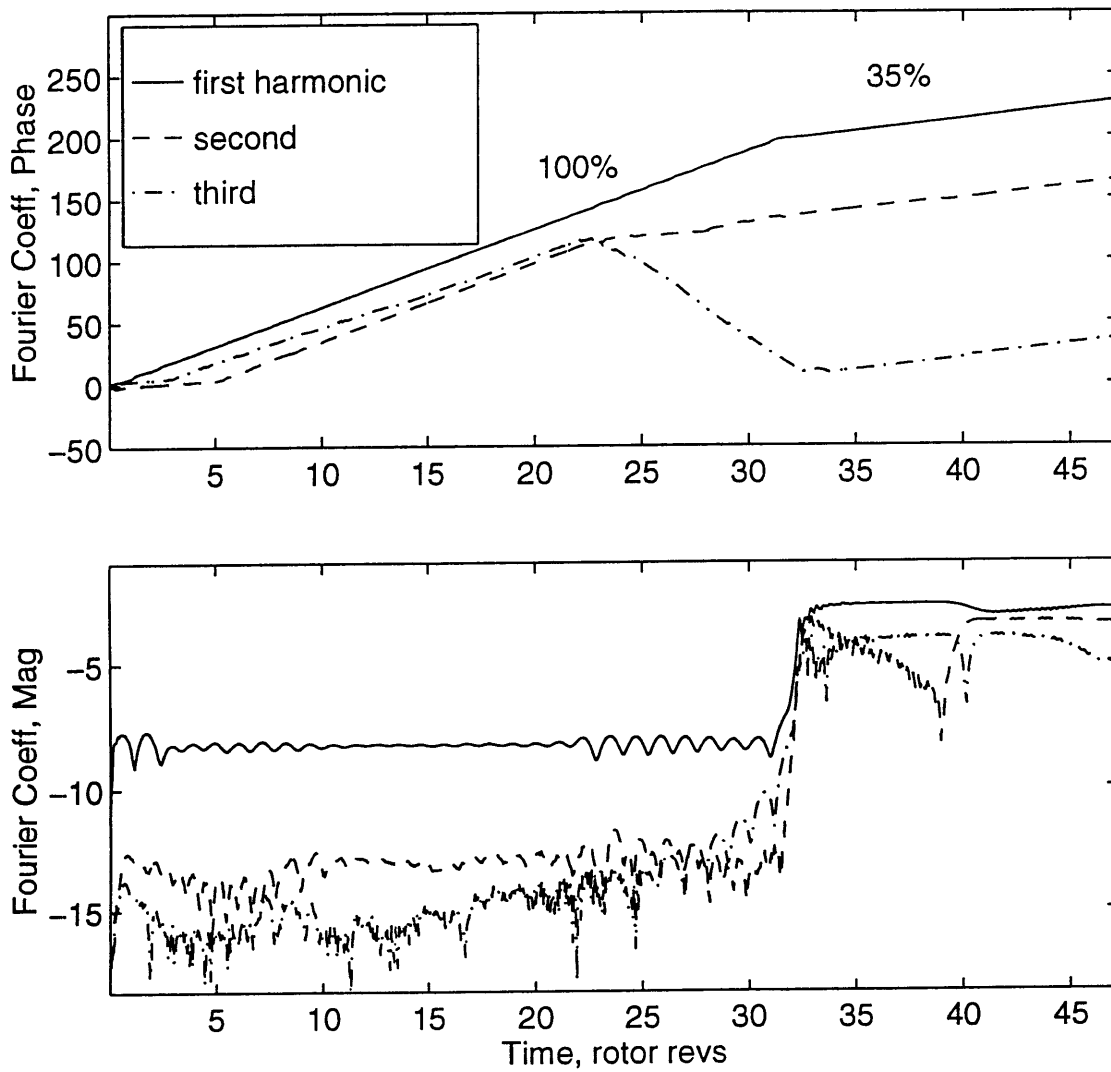
Figure 3.26   Time history of the first three harmonics of flow

coefficient with once per revolution forcing for 4-

stage compressor at 70% corrected speed

efc4s 70%

$\times 10^{-4}$

Power

2.5
2
1.5
1
0.5
0

25
20
15
10
5
0   0

0.5
1
1.5

Time, Rotor Revs

Frequency (/rotor freq.)
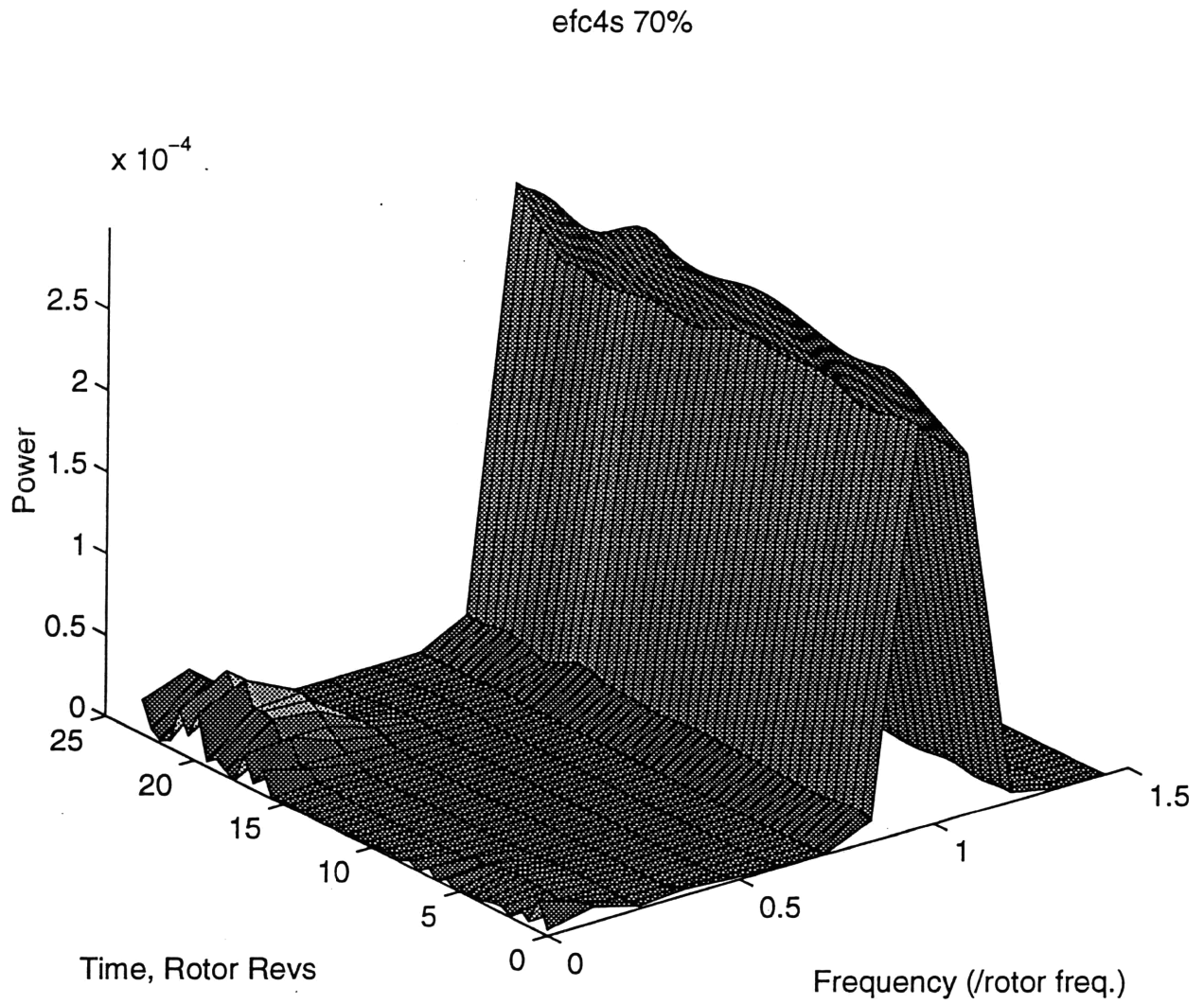
Figure 3.27   Time history of the frequency components in the first

harmonic of flow coefficient for 4-stage compressor at

70% corrected speed

nasa3s 80%

Figure 3.28   Comparison of input and calculated overall

compressor characteristics of NASA 3-stage

compressor at 80% corrected speed

Figure 3.29   Comparison of flow variables calculated from current

model (solid line) and PWmean (dashed line) at an

operating point where the inlet Mach number is 0.415
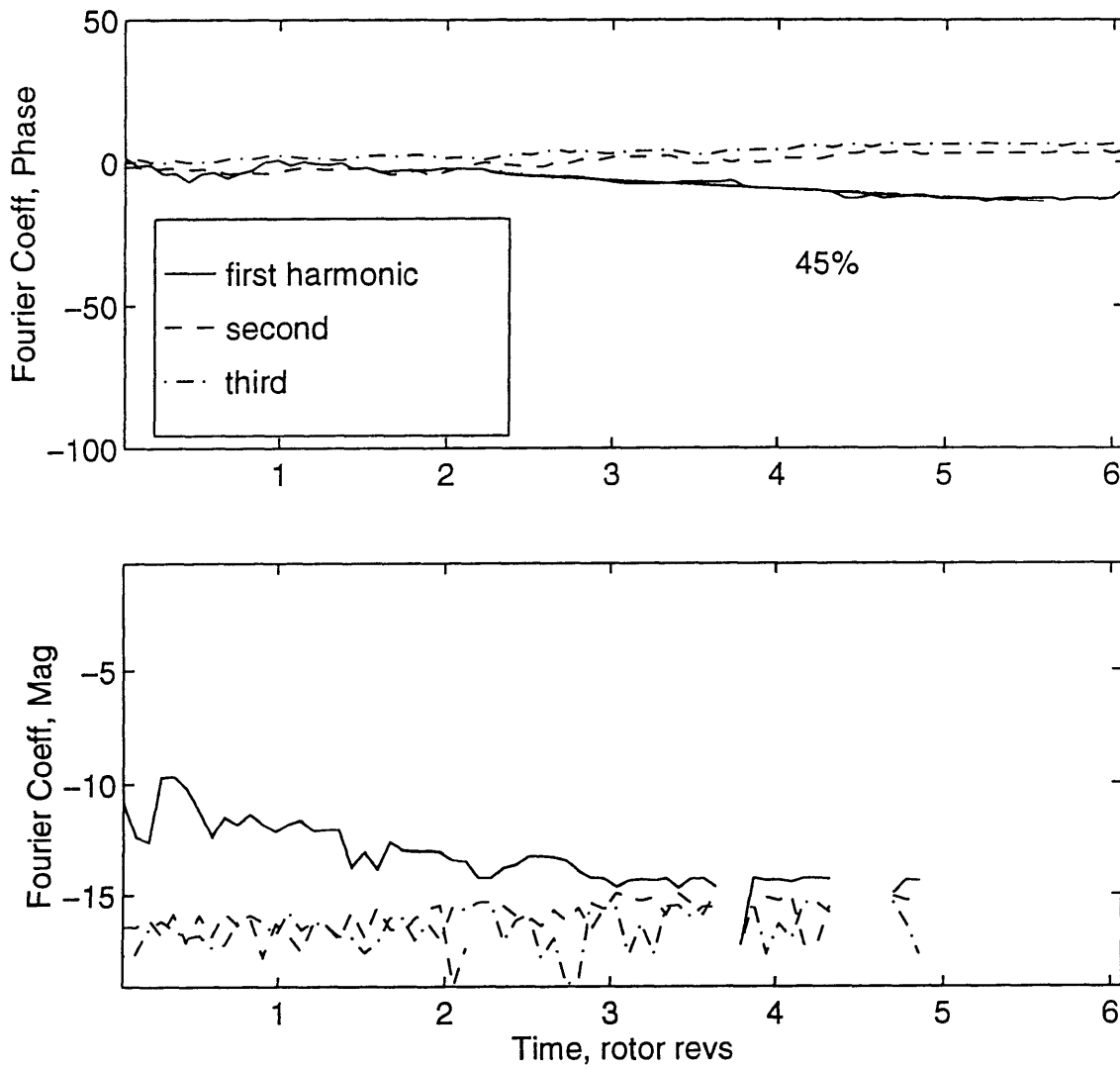
Figure 3.30 Time history of inlet flow coefficient in NASA 3-stage

compressor at 80% corrected speed

Figure 3.31   Eigenvalues plots for rotating stall type of instabilities

from linearized analysis for NASA 3-stage compressor

at 80% corrected speed

Figure 3.32 First (solid line) and second (dotted line) spatial fourier

coefficients, phase and magnitude immediately prior to stall

inception for 4-stage compressor at 100% corrected speed (data)

EFC4s 100% n=0
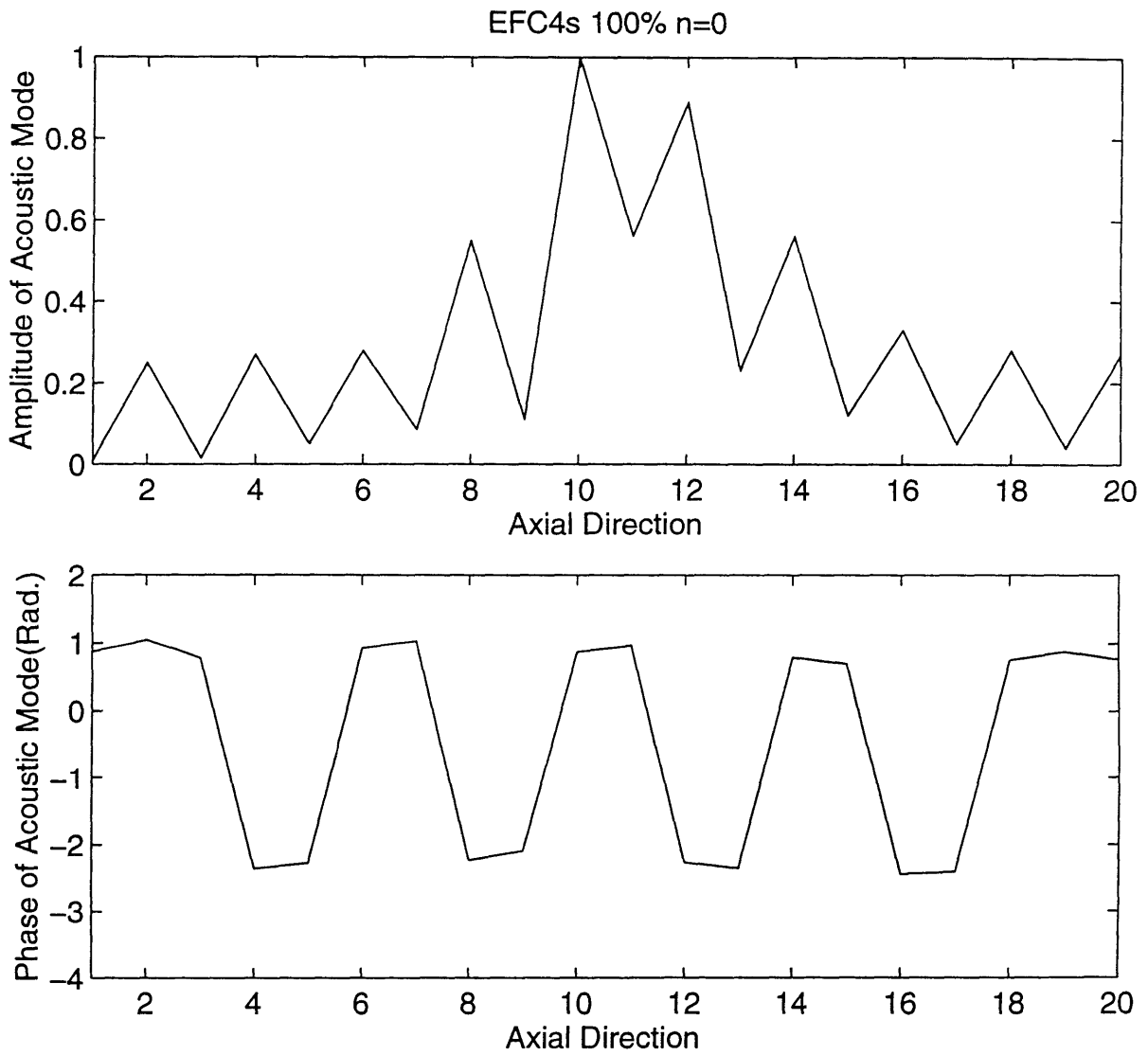
Figure 3.33   Axial distribution of the amplitudes and phases of the

acoustic mode in zeroth harmonic
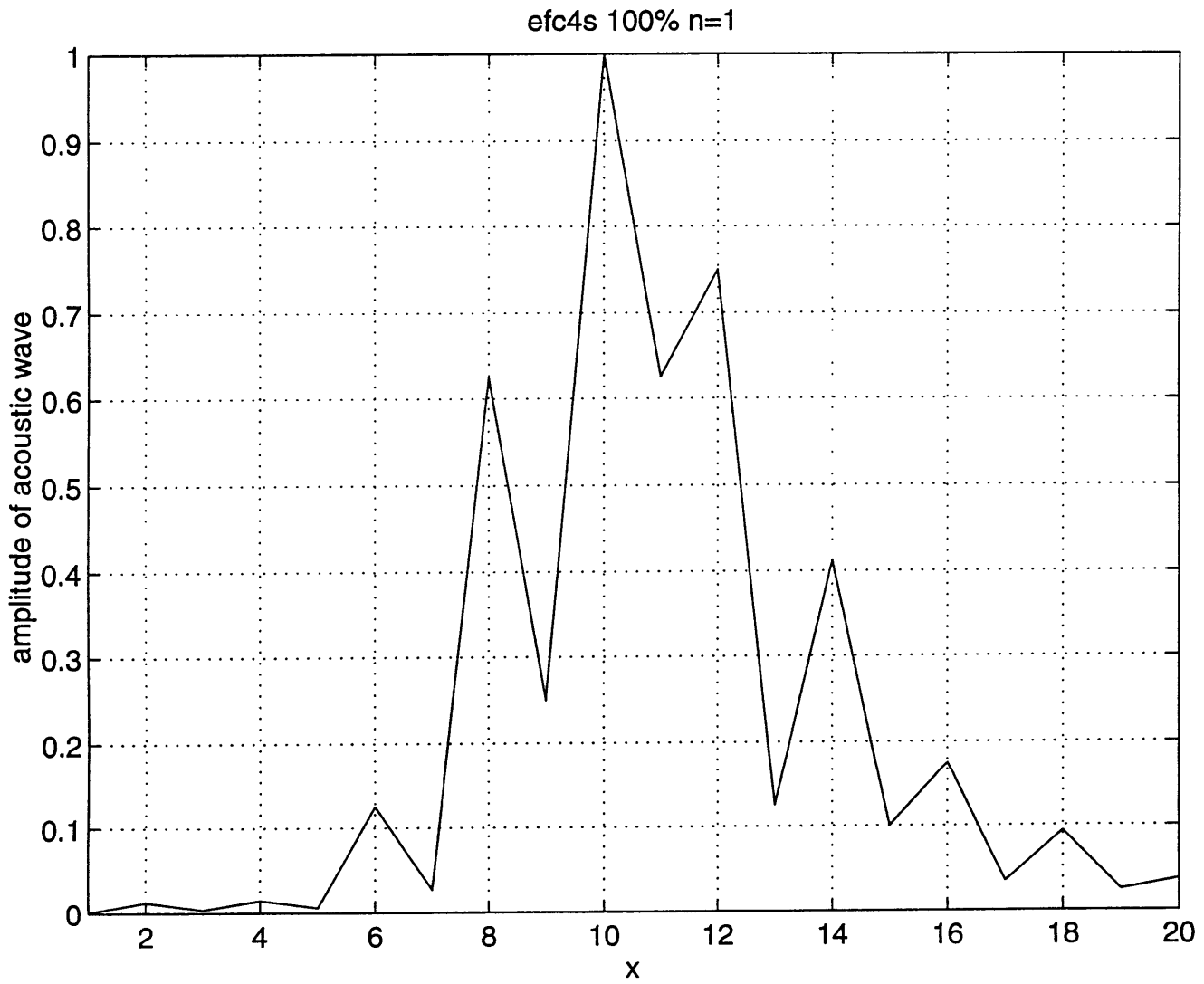
Figure 3.34   Axial distribution of the amplitudes of acoustic mode

in the first harmonic
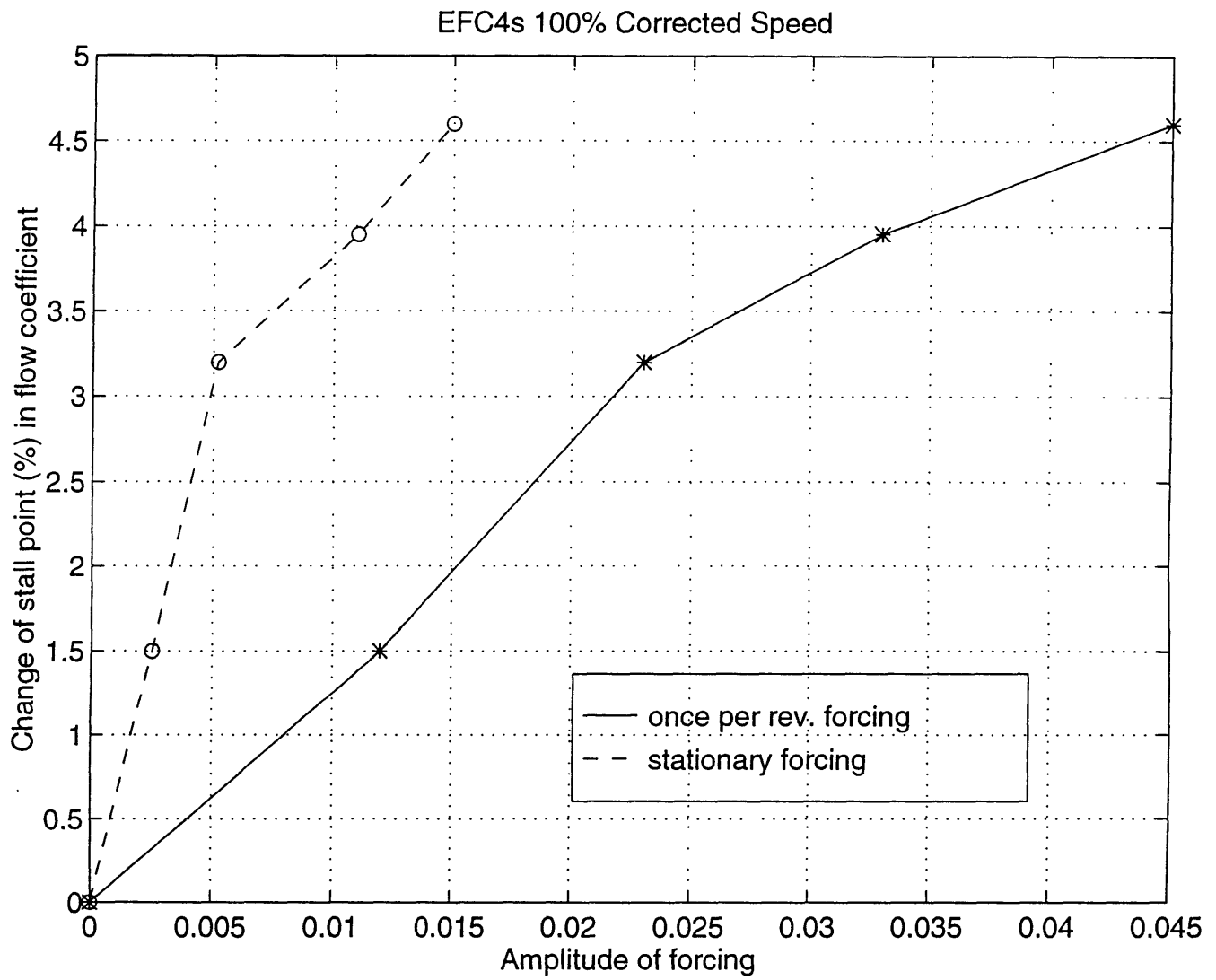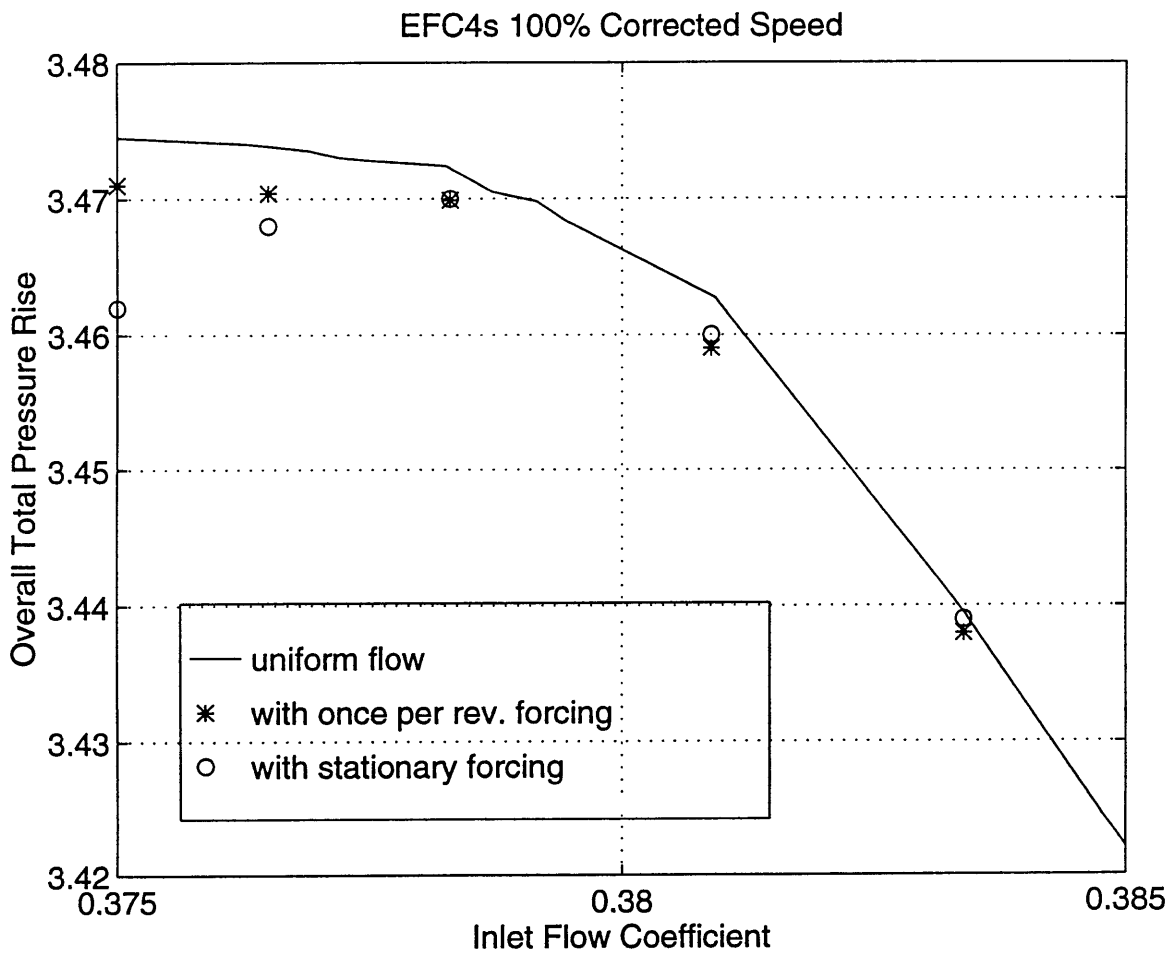
Figure 4.1   Forcing effect on change of stall inception point
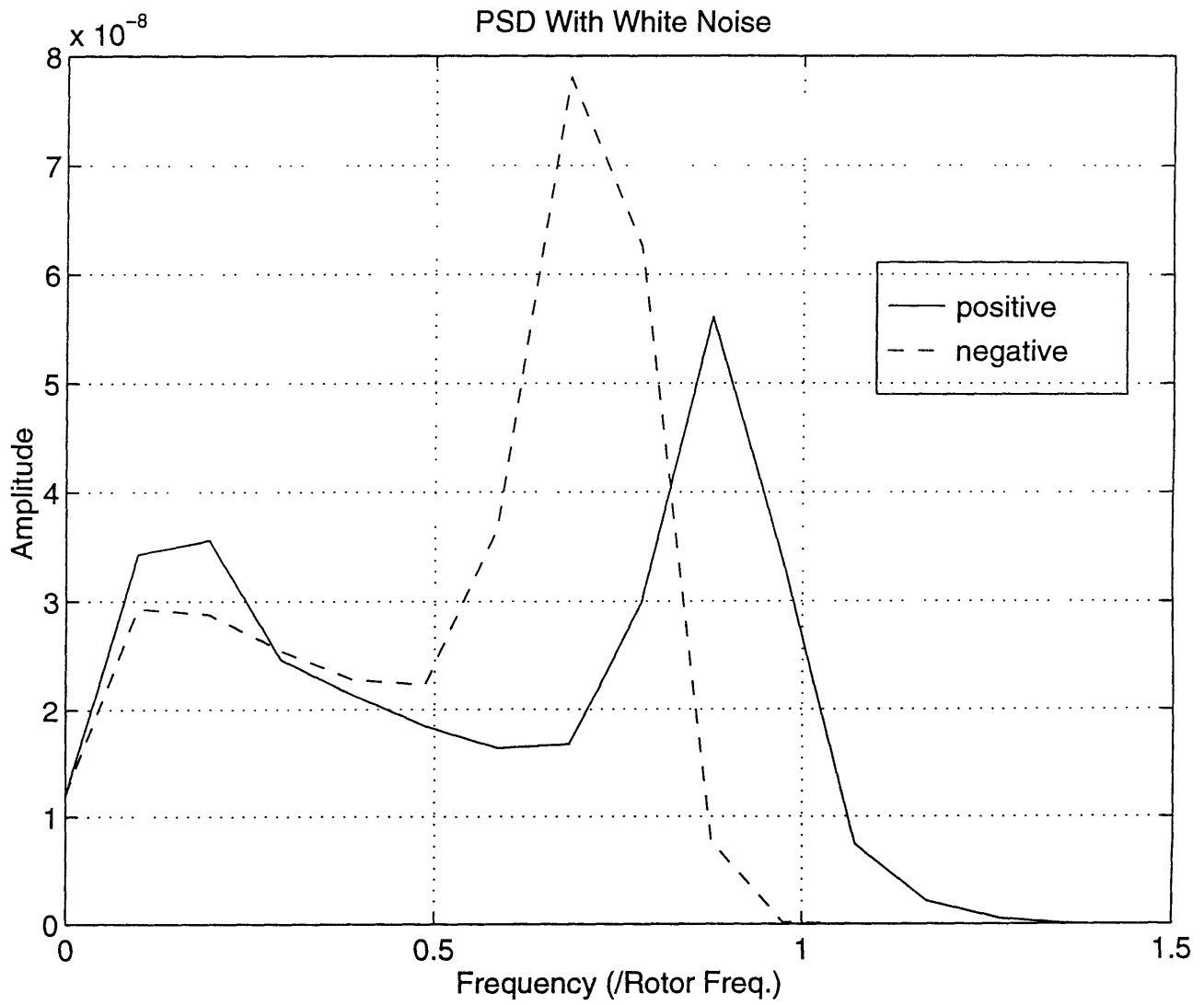
Figure 4.2   Steady-state characteristics

Figure 4.3   PSD of time history of the inlet flow coefficient with
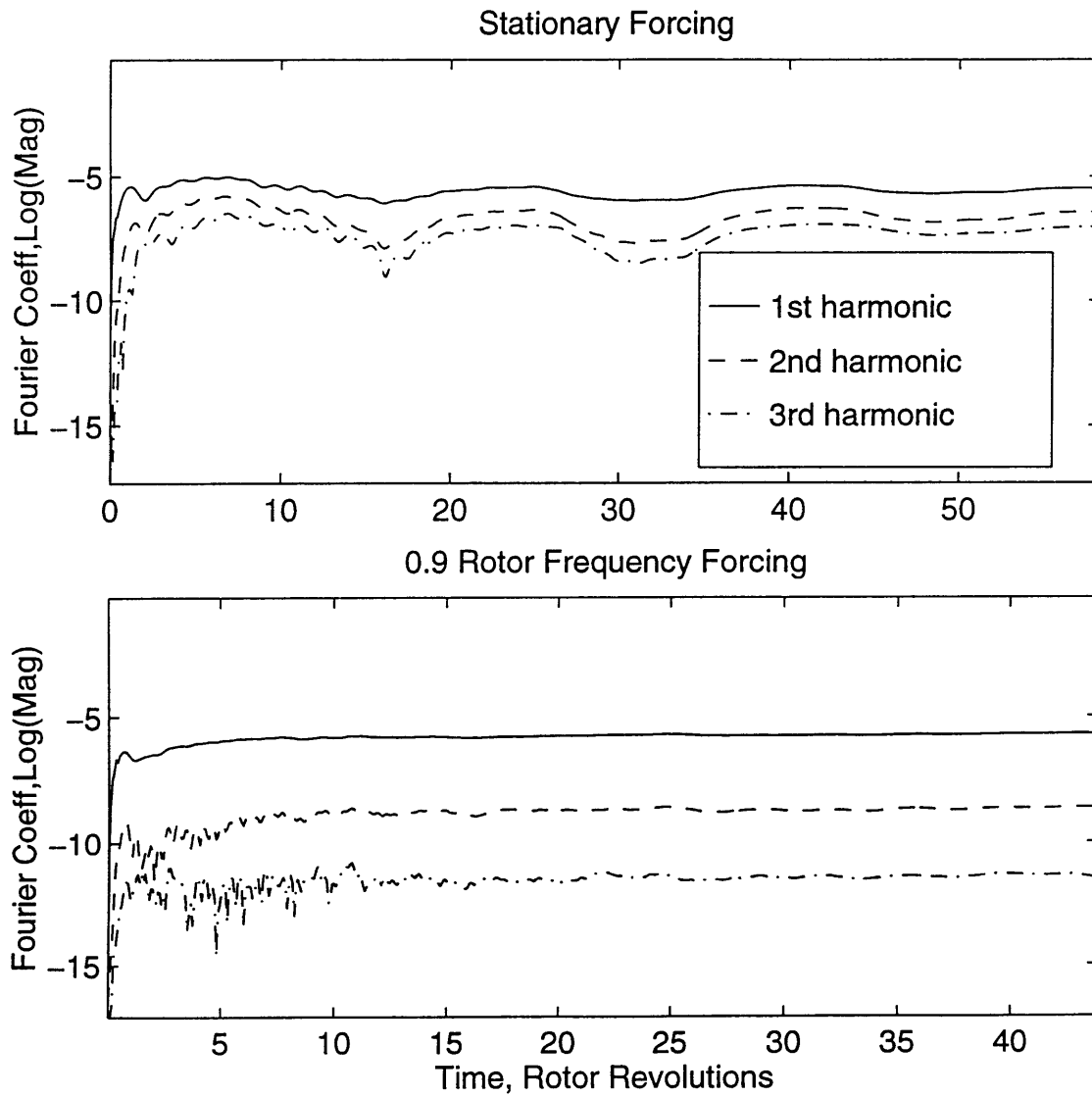white noise as forcing

Figure 4.4   Time history of the first three harmonics of inlet flow
coefficient with stationary forcing and 0.9 rotor
frequency forcing

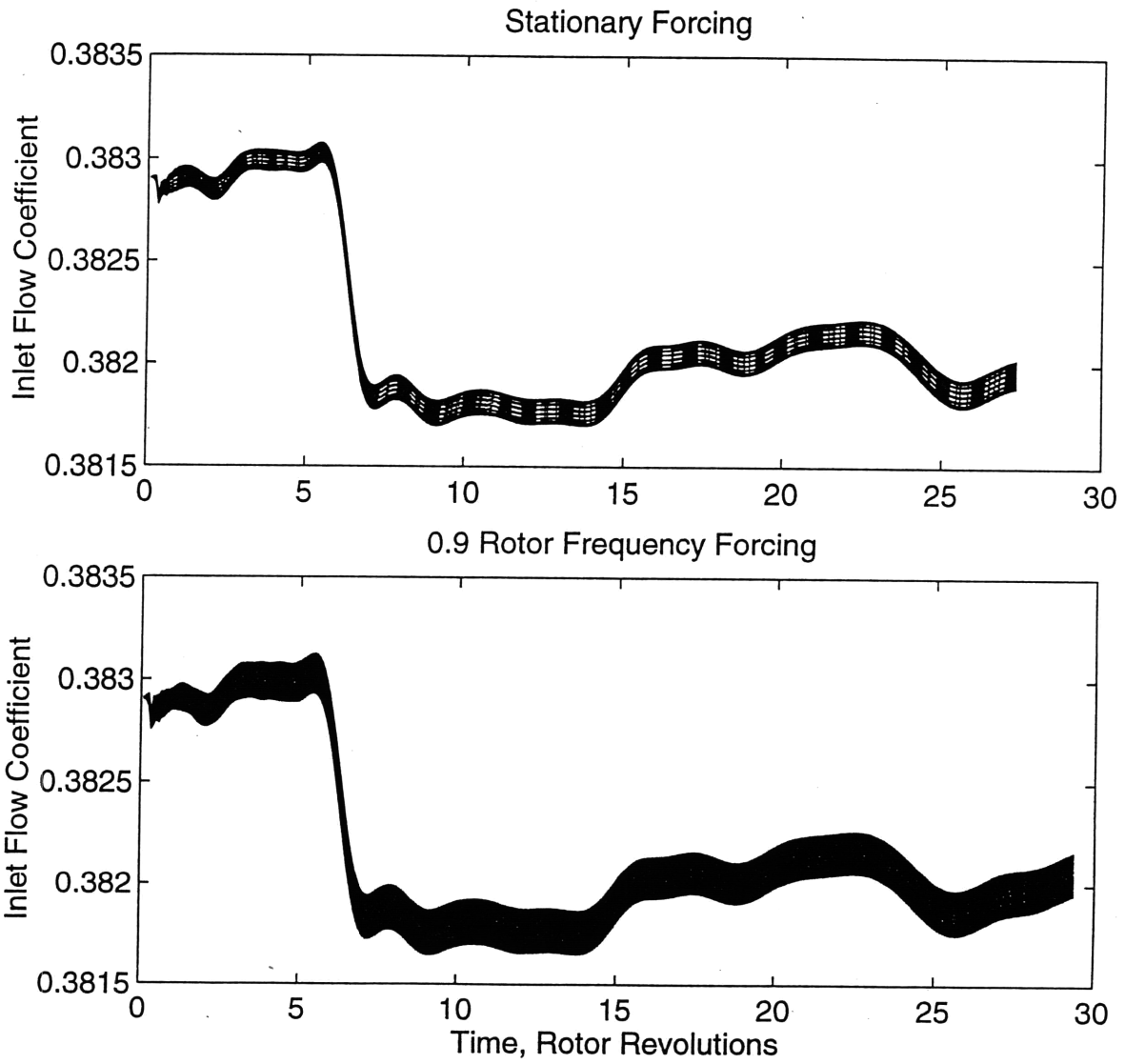Figure 4.5   Time history of inlet flow coefficient around the
              whole annulus with stationary forcing and 0.9 rotor
              frequency forcing

4206-1